Chem Soc Rev

Recent advances in energy transfer in bulk and nanoscale luminescent materials: From spectroscopy to applications

Journal:	*Chemical Society Reviews*
Manuscript ID	CS-SYN-01-2015-000067.R3
Article Type:	Review Article
Date Submitted by the Author:	28-Aug-2015
Complete List of Authors:	Liu, Xiaofeng; Zhejiang University, School of Materials Science and Engineering Qiu, Jianrong; Zhejiang University, School of Materials Science and Engineering

Recent advances in energy transfer in bulk and nanoscale luminescent materials: From spectroscopy to applications

Received 00th January 50xx,
Accepted 00th January 20xx

DOI: 10.1039/x0xx00000x

www.rsc.org/

Xiaofeng Liu[a*] and Jianrong Qiu[a,b*]

Transfer of energy occurs endlessly in our universe by means of radiation. Compared to energy transfer (ET) in free space, in solid state materials the transfer of energy occurs in a rather confined manner, which is usually mediated by real or virtue particles, including not only photons, but also electrons, phonons, and excitons. In the present review, we discuss the recent advance on optical ET by resonance mediated with photons in solid materials as well as their nanoscale counterparts, with focus on the photoluminescence behavior pertaining to ET between optically active centers, such as rare earth (RE) ions. This review begins with a brief discussion on the classification of optical ET together with an overview of the theoretical formulations and experimental method for the examination of ET. We will then present a comprehensive discussion on the ET in practical systems in which normal photoluminescence, upconversion and quantum cutting are resulted from ET involving metal ions, QDs, organic species, 2D materials and plasmonic nanostructures. Diverse ET systems are therefore simply categorized into cases of ion–ion interaction and non–ion interactions. Special attention has been paid to the progress in the manipulation of spatially confined ET in nanostructured systems including core–shell structures, as well as the ET in multiple exciton generation found in QDs and organic molecules, which behavior quite similarly to resonance ET between metal ion centers. Afterwards, we will discuss the broad spectrum of applications of ET in the aforementioned systems, including solid state lighting, solar energy utilization, bio–imaging and diagnosis, and sensing. In the closing part, along with a short summary, we discuss further research focus regarding the remained problems and possible future directions of optical ET in solids.

1. Introduction

The delivery of energy is ubiquitous in our universe and it occurs across vast length scales, from atomic to interstellar distances. By means of radiation, solar energy is endlessly delivered and deposited onto the earth. A large part of the solar radiation is captured by various plants, where the energy of the visible photons absorbed by antenna complexes in plant leaves is delivered to reaction centers which then perform the photosynthesis.1,2,3 These radiative and non-radiative energy transfer (ET) both can be regarded as optical process as they have to be mediated by photons.

Inside the solid state materials, spatial redistribution of energy occurs spontaneously to remove energy gradient after sudden injection of energy by a thermal or optical excitation. Meanwhile, in a microscopic scale ET occurs across a considerable distances that can far exceed atomic size range, while the pathways accessible to such ET process becomes rather limited in solids compared to ET in free space. Generally, ET in an optical fashion occurs in insulators or semiconductors with bandgap in the optical frequency. After excitation by, e.g., photons, spatial redistribution of energy inside these solids can be often mediated by the photon-generated excitons, which act as the energy carrier and migrate to a distant site before recombination. This is a very common case of energy migration in bulk solid and conjugate polymers.

On the other hand, optical ET also takes place by resonance between pair of separated donor and acceptor incorporated inside solids as well as their nanoscale counterpart. The donor or acceptor can be any optical active species, including metal ions, quantum dots (QDs), molecules, and organic complex and quasiparticle like exciton. Regardless of the radiative or non-radiative mechanism, this process can be simply described in analogue to a chemical reaction by $D^* + A \leftrightarrow D + A^*$, where the asterisk indicates the ion or molecule at the excited state (**Fig.** 1). Energy resonance between the donor-acceptor (D-A) pair is required by this reaction. This ET mechanism by resonance has played a dominating role in the generation of upconversion (UC) and quantum cutting (QC) (also referred as downconversion, DC) in most rare-earth (RE) doped systems, as well as multiple exciton generation in QDs and organic molecules. Despite that diverse systems can participate in ET, in the context of ET they share important characteristics. It is the purpose of the present review to make clear the similarities as well as differences of ET in different systems, and discuss together their related applications.

[a] School of Materials Science and Engineering, Zhejiang University, Hangzhou 310027, P. R. China. E-mail: xfliu@zju.edu.cn.
[b] College of Materials Science and Engineering, South China University of Technology, Guangzhou, 510640, P. R. China. E-mail: qjr@zju.edu.cn.

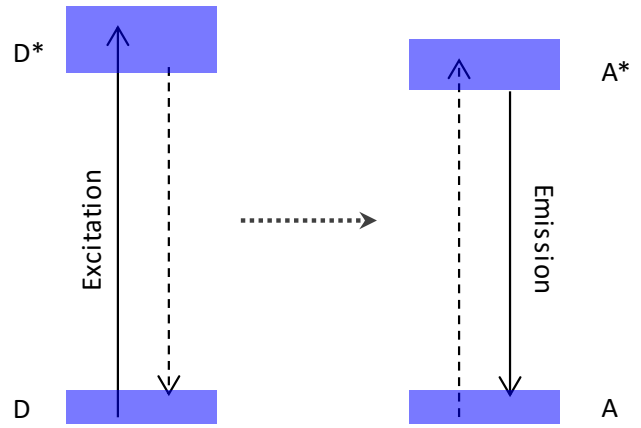

Fig. 1 Schematic representation of ET from a donor (D) to an acceptor (A) center. D* and A* stand for the donor and acceptor at their excited states, respectively. Usually, the energy levels of D, D*, A and A* are located within the bandgap of the host material for RE or TM doped materials.

In spite of the rapid advances in the past over 60 years, resonant ET is among the one of the most active area of the interdisciplinary research bridging physics, chemistry and biological sciences. These investigations have led to the discovery of more efficient phosphors, laser materials, optical bio–probes, and etc.4-11 We will review optical ET in solid state materials here, with special emphasis paid on the recent advances in nanoscale systems. It is certainly not possible to cover all the related issues of ET spanning from biology to material sciences. ET related with solar light capture in plants and other biological system will not be covered as it is sufficiently described in many reviews.9,10,11 In addition, it is not the intention of this review to give an in–depth discussion about ET between organic molecules or bio–organic substances and exciton mediated ET that occurs mostly in semiconductors as well as conjugate polymers.12,13,14,15,16

The organization of the present review is as follows. In the following section we will discuss different types of ET and give a brief description of the theoretical formulations and the experimental methods. We will then review typical ET systems involving ions doped in bulk and nanomaterials, and non–ion systems, such as QDs, molecules and two-dimensional (2D) materials. In these systems, ET, as demonstrated by different optical spectroscopy, can be used to modulate the emission spectra and to generate UC and DC emission in diverse materials. Application of optical in diverse areas from photonics, energy to medicine will be discussed in the followed section. Finally, we will summarize the current research process and discuss possible future directions for ET in solid state materials.

2. Classification, theory and experimental method

Optical ET has been divided into different types which occur in a pair/group of D-A under different conditions. As introduced below, ET may occur by resonance, semi–resonance, or double resonance depending on characteristics bearing by the D-A pair. Brief description regarding the theoretical background and experimental method for examining ET are also provided below.

2.1 Types of optical ET

2.1.1 Resonant ET

The most widely examined types of ET are based on resonance. However, resonance does not mean that the donor has the exact same energy levels as that of the acceptor, in which forward and backward ET would have the same chance.17 To enable directional ET from D to A, the donor prefers acceptors bearing slightly lower energy levels meanwhile with sufficient energy overlap. Backward ET (from A to D) also occurs at the same time by theory, while under this condition it is not energetically favoured. Therefore, this directional ET process degrades the excitation energy due to the small energy difference between donor and acceptor. The "missing" energy is usually dissipated as heat. In solid state materials, donor or acceptor includes different main group and transition metal (TM) ions, metalate anions, and the host lattice itself. They have different characteristics and emission can be of both ordinary and anti–Stocks type, which will be discussed in detail in section 3.

2.1.2 Non–Resonant ET

On the other hand, ET, in the absence of strict resonance condition, still occurs in many systems and it has been understood from both the experimental and the theoretical level.18 The first type of non–resonant ET can be regarded as a semi–resonance type, where the small energy mismatch between the donor and the acceptor is bridged with several phonons.19 In the second case, ET takes place completely without resonance among three centers, in which one of the centers has a high excited state at energy 2E and the other two centers have energy levels at E, as can be expressed by D* + A + A $\leftrightarrow$ D + A*+ A*.18,20 The occurrence of this three–center process requires close proximity of the centers, and it has been usually referred as double–resonance ET. If the center with energy level at 2E servers as the donor, the process is known as cooperative downconversion (DC), which is a typical mechanism for QC; and the reverse process is known as cooperative UC. Since cooperative process requires the close proximity of the two centers of identical energy, a high concentration of dopant is usually necessary in order to maximize the rate of ET by high order interactions.

2.2 Theoretical formulations of ET

2.2.1 Förster–Dexter theory

Modern theoretical foundation of resonant ET that has been widely accepted and introduced in literatures was laid by Fröster in the 1940s using semi–quantum treatment for dipole–dipole (d-d) interaction, and later in the 1950s it was extended by Dexter to include the contribution of multipole interactions as well as exchange effect based on quantum mechanical method.21,22 This is why resonant ET has always been referred as Föster–Dexter ET. In spite of enormous

development in both experimental observations and theoretical advances in the past 60+ years, this old theory remains valid and useful. It is now extensively applied in systems from the initial solutions containing dissolved fluorescent molecules to solid materials activated with metal ions and biological systems, in which certain conditions are not considered in the early development.12

In the weak coupling limit when direct electronic coupling between donor and acceptor is absent (see Fig. S1 in electronic supplementary information), the ET rate can be derived using Fermi's golden rule based on time–dependant perturbation theory.23,24 When the donor and acceptor are approximated as point dipole the well–known R^{-6} scaling can be found:22

$$k_{dd}(R) = \frac{3c^4\hbar^4\sigma_A}{4\pi n^4 \tau_D R^6}\int \frac{f_D(E)f_A(E)}{E^4}dE \quad (1)$$

where R is the D–A seperation, n is the refractive index of the host, τ_D is the radiative lifetime of the donor in the absence of the acceptor, σ_A is the absorption cross section of A, and $f_D(E)$, $f_A(E)$ are the normalized emission spectra of the donor and the absorption spectrum of the acceptor. From the equation above it is clear that ET rate is proportional to R^{-6} and the magnitude of spectral overlap (integral in eq. 1), which affords the resonance condition. By introducing the critical distance R_0 (or sometimes referred as Förster distance), eq. 1 can be simplified as:

$$k_{dd}(R) = \frac{1}{\tau_D}\left(\frac{R_0}{R}\right)^6 \quad (2)$$

where the critical distance R_0 can be expressed by:

$$R_0 = \frac{3c^4\hbar^4\sigma_A}{4\pi n^4}\int \frac{f_D(E)f_A(E)}{E^4}dE \quad (3)$$

From the equations above the physical meaning of R_0 is evident: for donor and acceptor separated by R_0 the ET rate equals the decay rate ($1/\tau_D$) of the donor.

With the decrease in D–A separation high order interactions will become operative.22 In the case of dipole–qudrapole (d–q) and qudrapole–qudrapole (q–q) interactions, the ET rates scale with R^{-8}, and R^{-10}, respectively, suggesting that these high order interactions operate in a much shorter distance. When considering different types of interactions, we have the following general form for ET rate:25,26

$$k_{DA}(R) = \frac{\alpha_{dd}}{R^6} + \frac{\alpha_{dq}}{R^8} + \frac{\alpha_{qq}}{R^{10}} + \cdots = \sum_{i=6,8,10}\frac{\alpha_i}{R^i} \quad (4)$$

As the low order interactions dominate the ET process in most cases, the magnitude of α_i should have the following sequence: $\alpha_{dd} > \alpha_{dq} > \alpha_{qq}$. In many early examples of molecular systems only d–d interaction is considered, which however already gives good agreement with the experimental results. 12 Nevertheless, multipole interactions should be taken into account when d–d interaction is not allowed, for instance, some f–f transitions of RE ions. Based on eq. 4, it is possible to figure out the dominating ET mechanism by the examination the dependence of radiative lifetime with the D–A separation R.

In case that donor and acceptor stay very close such that their electron wavefunction overlap (see Fig. S1), exchange interaction between them will dominate the ET process. According to quantum mechanics the ET rate can be described as:22,27

$$P_{ex}(R) = (2\pi/\hbar)K^2\exp(-2R/L)\int f_D(E)f_A(E)dE \quad (5)$$

where K is a constant related with the overlap of the wave function, L is the effective Bohr radius of the system. Here the ET rate varied as exp(–2R/L) with R, which is used to describe the radial distribution of the wave functions.

2.2.2 Phonon–assisted ET

The discussion above concerns different types of ET which all rely on the resonance condition between donor and acceptor, as reflected by the spectral overlap integral given in eq. 1. The spectral overlap also includes the contribution of line broadening of different origins, such as thermal effect. Without strict resonance, this near–resonance ET occurs with the help of lattice phonons; the rate therefore rise with the increase of temperature due to increased phonon population. The dependence of ET rate on temperature can be described by the following equation:19

$$k_{ET} \propto (k_B\mathrm{T}/\hbar\bar{\omega})^N \quad (6)$$

Here, $\hbar\bar{\omega}$ is the average energy of lattice phonons, and N is the number of phonons involved in the ET. For an energy mismatch of ΔE between donor and acceptor, the ET rate is described by the following expression:

$$k_{ph}(\Delta E) = k_0\exp(-\alpha\Delta E) \quad (7)$$

where, $\Delta E = N\cdot\hbar\bar{\omega}$, α is given by $(1/\hbar\bar{\omega})|\ln\epsilon|$ (ϵ is a constast), and k_0 is the zero–phonon ET rate. This is the well–known energy–gap law that governs radiative and non–radiative phonon–assisted processes in solid state materials.

2.2.3 Cooperative process

Beside the two center ET common for optical materials, the ET with the simultaneous participation of three centers have been known as a second-order process, in which the excitation ET between one donor and a pair of identical acceptors, or the reverse. Cooperative ET can lead to both DC and QC emission in several RE heavily doped materials.28,29,30 The cooperation process has been connected with high order interaction, such as d–q, q–q and exchange interactions. Theoretical description of this process has begun since the 1950s using quantum mechanical method.31,32,32 In the recent developments by modern quantum electrodynamics (QED), the matrix element in this three center ET can be described explicitly by the summarization of cooperative and accretive matrix element:

$$M_{fi} = M_{fi}^{ac1} + M_{fi}^{ac1} + M_{fi}^{co1} \quad (8)$$

where the superscript ac and co represent the accretive and cooperative process. The detailed mathematical expressions have been given by Andrew et al. in ref. 20.

2.2.4 Beyond the point dipole approximation

When the donor and acceptor cannot be approximate using point dipoles, for instance, 2D materials, the R^{-6} dependence of ET rate is no longer valid. Nevertheless, it is not difficult to derive the mathematical expressions of ET involving 2D materials. To put it simply, the dependence of ET rate (k_{ET}) on the D-A separation will have the following generalized relation:33

$$k_{ET} \propto R^{-n} \quad (9)$$

where n=6 for 0D (zero dimensional) D-A pairs, and n=4, and 2 for 0D–2D and 2D–2D pairs, respectively (see **Fig.** 2). However, in the bulk limit a R^{-3} dependence is found for the ET rate between 0D and surface of bulk donor (acceptor), as shown in **Fig.** 2c. Practically, small deviation from the relations expressed by eq. 9 is always observed in different experiments, which stimulated the development of more precise theories.34 In the case of ET in 0D–1D or 1D–2D donor–acceptor pairs, a simple rate–distance relation is not found as the ET rate depends on not only the distance but also the orientation of the 1D donor (acceptor) with respect to the 0D or 2D acceptor (donor). Mathematical treatment of ET in these cases becomes rather complicated but still can be based on the Förster(–Dexter) theory.

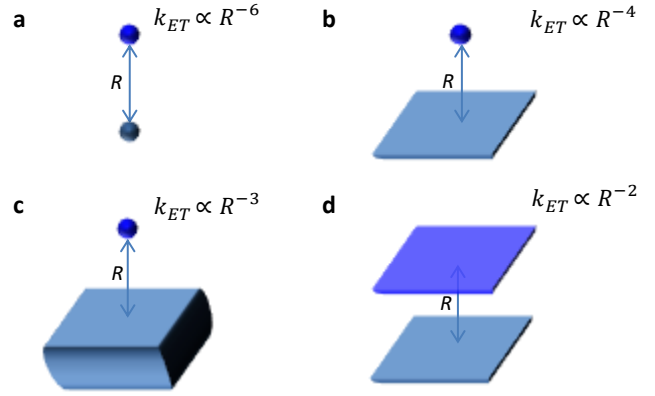

Fig. 2 ET in D–A pairs of different geometry. (a) 0D–0D, (b) 0D–2D, (c) 0D–3D (bulk surface) and (d) 2D–2D. The ET rate scales with the inverse of the n–th power of D–A distance with n=6, 4, 3 and 2 for cases shown in (a–d).

The point dipole approximation also fails when treating ET involving large molecules, such as conjugated polymer and bio-substances.12 For instance, in pairs of D–A each consisting of multiple chromophores that are intimately coupled forming excitonic state in a collective manner, changes to the original Förster formation and generalized Förster resonance ET (FRET) theory have to be used for a precise interpretation of the ET efficiency in this systems.35 The generalized FRET theory is also successful in the description of ET involving inorganic nanomaterials such as semiconductor nanorods and also conjugates polymers and biological structures without well-defined shape.35,36,37 The FRET theory however only valid in the weak electronic coupling limit, that is, the separation between donor and acceptor are large enough to prevent delocalization of excitons. At higher coupling strength, Fermi's gold rule which describe ET based on perturbation is no longer valid, and a more complex picture appears. In the intermediate and strongly coupling region, the separations are comparable to the size of the molecule itself, and the molecular excitons are delocalized among the sites, forming coherent superpositions. This type of ET exists in light photosynthetic systems and it is believed to occur in the wavelike process through quantum coherence.3 Detailed theoretical interpretations of this process and the examples can be found in several recent publications and reviews.12,38,39,40,41

2.2.5 Unified theory on radiative and non-radiative ET

The Förster–Dexter theory presented above describes radiationless ET and therefore it is applicable only under near field condition (small D–A separation) which does not involve the emission of real photons. Unifying far-field radiative ET and the near-field ET has been continuously pursued by theorists by using both classical electrodynamic theory and quantum chemical methods. For the photosynthetic process in bacteria, for instance, modern electrodynamic modelling has enabled the capturing of both coherent and incoherent terms of excitonic ET and energy flux within the structures covering both near field and far field region.42,43 On the other hand, helped by the development in QED, resonant ET theory has been reframed such that short range and long range interaction (by e.g., radiation) are unified in a single mechanism. The formulation of ET using QED was pioneered by Avery et al in 1960s, 44,45 and later developed by Andrew et al.46,47 The detailed mathematical derivation has been provided in many literatures. To put it simply here, the rate of ET is divided into three terms as:48

$$\omega = \omega_F + \omega_I + \omega_{rad} \quad (10)$$

The first term can be considered as the normal Förster term, in which ET rate has a R^{-6} dependence and it operates only in near field (R<<λ). The second term is proportional to R^{-4}, which refers to a correction when the condition R<<λ is no longer obeyed. The third term has a R^{-2} dependence which becomes dominate for R>>λ, and it is in fact the rate of the acceptor captures a photon emitted from the donor (**Fig.** 3). The last radiative term certainly requires the participation of real photons, while photons are virtual in the first term for near field interactions. With the increase of D–A separation, the real character of photon involved in the ET increase, and eventually the radiative ET dominates. In this case, radiationless ET and radiative ET by reabsorption are unified in the same theory that works for all distances.47,49 This is why QED is regarded as a unified theory valid in both near field and far field ET.

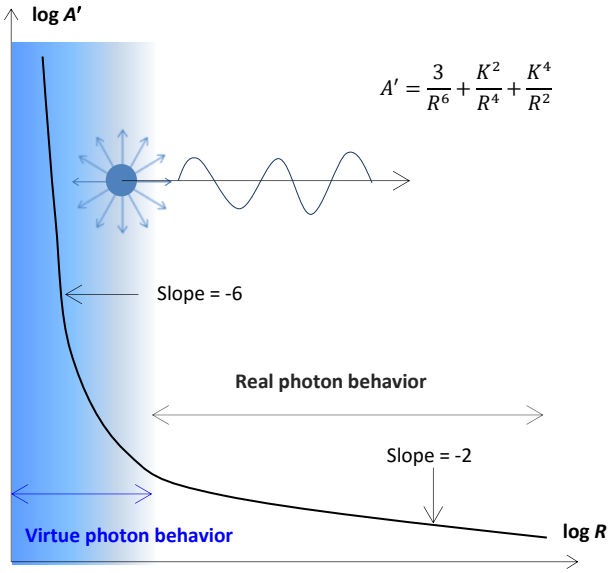

Fig. 3 Log–log plot of ET rate as a function of D-A distance (R). This relation is described by rotationally averaged function *A'*; where *K* is the wavenumber of the ET. Virtue photon behavior here is associated with the short–range non–radiative ET; while the real photon behavior is connected with the long–range radiative ET (photon re–absorption). Reprinted with permission from Ref. 49, copyright 2013, American Chemical Society.

2.3 Experimental methods

2.3.1 Steady state excitation and emission spectra

Steady state emission/excitation can provide a direct evidence of ET in most of the systems. Due to resonance, the excitation at the absorption band of donor normally leads to the emission of both donor and acceptor, as schematically represented in **Fig.** S2. It is important to note that in this region the acceptor does not absorb light. In other words, the excitation spectra for the emission of acceptor and donor must be the same, or at least strongly overlapped. This spectral character is an important fingerprint for ET in different types of D–A systems, including resonant ET, phonon assisted ET and cooperative process. Furthermore, from the change in the integrated emission intensity of the donor in the presence and absence of A, it is possible to determine qualitatively the efficiency of ET.

As ET is strongly sensitive to D-A separation, the steady state spectra evolves steadily with the changing of donor or acceptor concentration. This change would normally result in the notable increase/decrease in the acceptor/donor emission intensity, which can be observed in different D–A codoped systems, especially for RE activated materials.50 High doping concentration of A is however detrimental due to concentration quenching arise from increased cross–relaxation (CR) and energy migration probabilities.

ET is also affected by temperature as phonons are always involved because exact match in energy between donor and acceptor is rare in practical systems. The temperature sensitivity of ET enables remote optical thermal sensing using luminescent materials, as discussed in section 4.4.1 The phonon–assisted ET process can be accessed by the strong temperature dependence of ET. As phonon emission strongly depends on temperature, the phonon–assisted ET rate increases with the rise in temperature. This process is therefore ruled by the energy gap law as given by eqs. 6, and 7. Without the participation of phonons, low temperature freezes the ET process regardless of the types of optical centers.

2.3.2 Decay kinetics and transient state spectra

In comparison to steady state spectra, time resolved spectroscopy provides a powerful tool for the examination of ET and allows for a better understanding of the excited state dynamics. With the technological advance of ultrafast photo–detectors and lasers, the precise determination of the decay kinetics in time scale down to picoseconds becomes rather simple in recent years.51 Note has to be made here that the following discussion cannot be applied to ET by reabsorption (radiative process), in which the excited state lifetime of the donor is not affected by the presence of acceptor. In the case of resonant ET, the ET rate and efficiency can be directly calculated from the decay curves. The decay rate from a donor center contains the contribution of both intrinsic decay rate and ET rate to acceptors.

$$k_{DA} = k_D + k_{ET} \quad (11)$$

The intrinsic decay rate of the donor contains the contribution of radiative and non–radiative decay, i.e., $k_D = k_r + k_{nr}$ The efficiency of ET is defined as the fraction of photons being transferred to the acceptors by:

$$\eta_{ET} = k_{ET}/(k_D + k_{ET}) \quad (12)$$

Recalling eq. 2, the ET efficiency can be reformulated by using the D–A separation (R):

$$\eta_{ET} = R_0^6/(R_0^6 + R^6) \quad (13)$$

In the above equation, it has to be noted that the point dipole approximation is used and nonradiative rate is assumed to be zero ($k_D = 1/\tau_D$). According to this relation, half of the absorbed photons is transferred to the acceptor at D–A separation of $R=R_0$, and the ET efficiency reaches 0.985 for $R=0.5R_0$, indicative of the near field nature of ET.

Experimentally, from the decay curves the fluorescence lifetime can be directly measured, which can be used for the calculation of the ET rate and efficiency (Fig. S2 in ESI). Typically, the ET efficiency is determined using the fluorescence decay curves of the donor in the absence (I_D) and presence (I_{DA}) of acceptor by 51:

$$\eta_{ET} = 1 - \frac{\int_0^\infty I_{DA}(t)dt}{\int_0^\infty I_D(t)dt} \quad (14)$$

In this equation the integrals are proportional to the steady state intensity of the donor in the presence (I_{DA}) and absence (I_D) of acceptor. In the case of single exponential decay, eq. 14 can be rewritten by using the lifetime values derived from the decay curves:

$$\eta_{ET} = 1 - \frac{\tau_{DA}}{\tau_D} \quad (15)$$

Here τ_{DA} is the fluorescence lifetime of the donor in the presence of acceptor, respectively. However, ideal exponential decay is rarely found in practical systems, such as molecules and RE–doped materials. In terms of multi–exponential decay the lifetimes used in eq. 15 τ_{DA} and τ_D should be replaced by the sum of decay times ($\sum \alpha_i \tau_i$) which are derived by fitting the decay curves using multi–exponential functions.

$$\mathrm{I(t)} = \sum_i \alpha_i \exp\left(-\frac{t}{\tau_i}\right) \quad (16)$$

Practically, all the decay curves can be fitted using the multi–exponential functional irrespective of the different decay mechanisms. Although these expressions have been widely used for the examination of ET in different systems, it is important to note here that we have to assume that the donor and acceptor have constant distances when using the above equations. For the random distribution of donor and acceptors as commonly found in solid materials, like phosphors, precise description of the ET rate can be made by more complicated expressions.52,53,54

2.3.3 Ultrafast spectroscopy

In the recent decades, the development of ultrafast laser systems, e.g., Ti–sapphire femtosecond laser, has led to the rapid advance in the use of these lasers for the studying of the ultrafast process down to femtosecond time scale. These methods thus allows for the capturing of snapshot of short–lived intermediate state in, e.g., chemical reactions and ET. There are several different types of ultrafast spectroscopy, and the technical details have been described in many text books and reviews.51,55 For optical process, transient absorption based on the pump–probe technique has been extensively used to track the evolution of transient state following short pulse laser excitation. These techniques are especially useful in revealing the mechanisms of carrier multiplication (CM) in semiconductor QDs as well as singlet fission (SF) in organic molecules.56,57 In transient absorption measurement, a short pump pulse excites the sample, and then the absorption change is probed by another sequence of short pulses. From the absorption change the formation of bi–excitons in QDs and organic molecules can be examined. This technique is proven to be particularly useful for revealing the exciton dynamics in semiconductors.

2D electronic spectroscopy is another powerful ultrafast technique for the studying of the ET and its microscopic mechanisms.58,59,60 Here, 2D does not means spatial two–dimensionality. In the 2D spectra, the emission is plotted as a function of absorption, and electronic coupling or ET between chromophores with different frequencies would lead to the appearances of cross–peaks in the spectra. Technically, 2D spectrum is based on a four–wave mixing set–up with phase–matched box geometry. This technique allows for the mapping of the energy landscape of intermediate state during an ET process occurring in organic or bio–organic molecules. By tracing the evolution of intermediate state, it is possible to locate the direction of energy flow and the time scale of ET. This technique is especially useful for the examination of photonic process in bio–systems. For instance, strong–coupled wave–like ET through coherence is clarified in photosynthetic systems by 2D spectra.60 More examples employing 2D spectra for studying ET in molecular aggregates are described in refs. 58,59 and 60.

3. ET in practical systems

In this section, we will discuss in detail the ET in different ion pairs and materials as well as the resultant normal down-shifted emission, UC and DC (or QC). Similarities as well as differences are discussed and highlighted for ET in different systems. These topics included in this section can be roughly divided into two categories: ET between metal ion centers (mostly RE ions), and ET involving non–ion centers, such as molecules, QDs and plasmonic nanostructures. Special focus has been placed on the recent advances in management of ET in nanoscale materials, such as nanoparticles and 2D materials.

3.1 Host-ion and ion-ion ET

3.1.1 Typical host sensitized emission

Photoluminescence (PL) from a number of phosphors relies on the sensitization by the host lattice, which efficiently captures the excitation photons. In host sensitized luminescence, UV excitation of the host first produces excitons, which prefer to pass the excitation energy to the activators ions rather than emitting by recombination.61, 62 Usually, the excitons induced by excitation migrates across certain distance before eventually being captured by emission centers, like RE ions. Host sensitization can occur under sufficient high energy excitation that induces band gap transition of the host for all phosphors. In practical phosphors, host sensitization enables more efficient excitation in the near ultraviolet (UV) region where strong emission lines of dilute mercury gas and Xeon gas are located. Typical hosts are built up of metalate anions of TM ions, such as VO_4^{3-}, MoO_4^{2-}, WO_6^{6-}, which strongly absorbs UC radiation of Hg and Xe gas.62 For instance, in the well–known red phosphor YVO_4:Eu^{3+},63,64 excitation in the UV region from 300 nm to 400 nm is highly efficient for the generation of red emission by the transition of $^5D_0 \rightarrow {}^7F_2$(see **Fig.** S3).62,65,66 On the other hand, optical centers with 6s2 electronic configuration such as Bi^{3+}, Pb^{2+}, and 5s2, Sn^{2+}, and Ce^{3+}, are naturally host–sensitized and are often used in scintillator materials due to their short fluorescence lifetime (<50 ns). 56 Because of the high lying energy levels, the emission from these ions is usually generated by direction excitation of the host and the emission is therefore mediated by excitons. In Table S1, we list the typical host sensitized phosphors developed in the past half–century.62

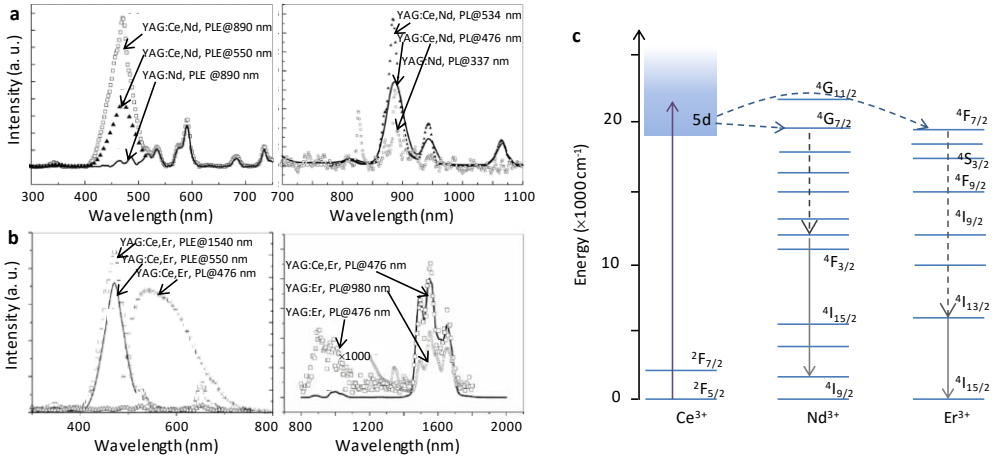

Fig. 4 Sensitized NIR emission in YAG:Ce^{3+}, RE^{3+} (RE=Nd, Er). (a) Excitation spectra (left) for the visible (550 nm from Ce^{3+}) and NIR (890 nm from Nd^{3+}) emission of YAG:Ce^{3+},Nd^{3+}, and YAG:Nd, and emission spectra (right) of YAG:Ce^{3+},Nd^{3+}, and YAG:Nd^{3+} recorded at different excitation wavelengths. (b) Excitation spectra (left) for the visible (550 nm from Ce^{3+}) and NIR (1550 nm from Er^{3+}) emission of YAG:Ce^{3+},Er^{3+}, and emission spectra (right) of YAG:Ce^{3+},Er^{3+}, and YAG:Er recorded at different excitation wavelengths. The overlap in the excitation spectra confirms the ET from Ce^{3+} to Er^{3+} and Nd^{3+}. Reprinted with permission from Refs. 79 and 82, copyright 2007, 2008, American Institute of Physics. (c) Energy level diagrams for the illustration of ET from Ce^{3+} to RE^{3+} (RE = Nd, Er). In these ion pairs, the emission of RE from their 4f levels is sensitized by Ce^{3+}, which has a broad and strong absorption by f–d transition in near UV region depending on the nephelauxetic effect of the host. Excitation of the Ce^{3+} leads to the visible and NIR emissions of Nd^{3+} and Er^{3+}.

3.1.2 Ion-ion ET

Typical ET in most luminescent materials occurs between a pair of D–A without the participation of the host, which acts only as the platform for ET. To be an efficient sensitizer, it should have strong and broad absorption/emission that covers the thin absorption lines of the donor ion. To this end, RE ions with allowed d–f transitions, such as Ce^{3+} and Eu^{2+}, have been frequently employed as sensitizers for other RE ions with thin f–f transition lines as well as TM ions, such as Mn^{2+} (see Table S2 for examples). 62,67,68,69,70 On the other hand, Yb^{3+} often behaviours as an efficient donor center to sensitise near infrared (NIR) emission because its f–f transition by $^2F_{7/2} \rightarrow {}^2F_{5/2}$ has relatively large absorption cross section near 980 nm.71,72,73 (see Table S2 for more examples). Similarly, due to the rich f–f transitions there are also several other efficient RE–RE ion pairs as long as suitable energy levels are present. Especially, in the IR region the resonance condition required by ET is help with the increased peak broadening due to thermal effect.74,75,76,77

Besides being an efficient sensitizer for visible emission in phosphors, recently Ce^{3+} has been employed as an efficient broadband sensitizer also for ions emitting in the NIR region, which are of particular interest for applications as photonic materials.78,79,80,81 For instance, in the host of $Y_3Al_5O_{12}$ (YAG), where the strong nephelauxetic effect shift the d–f transition to blue region, the NIR emission of Nd^{3+}, and Er^{3+} can be produced by pumping Ce^{3+} using blue light (**Fig.** 4).79,82 In this case, Ce^{3+} excited to 5d levels transfer energy to Nd^{3+}, Er^{3+}, promoting them to high lying levels of $^4G_{7/2}$ (Nd^{3+}) or $^4F_{7/2}$(Er^{3+}). The NIR emission is produced after further relaxation crossing lower 4f level by multi–phonon assisted process. The excitation and emission spectra of YAG activated with Ce^{3+}–Nd^{3+}, and Ce^{3+}–Er^{3+} is shown in **Fig.** 4. A particular feature associated with ET between Ce^{3+} and RE^{3+} is that the NIR emission in these materials can be produced by broadband excitation in the visible, by for instance, Xe–lamp.

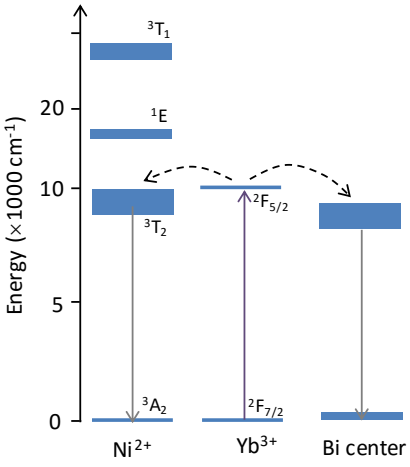

Fig. 5 Energy level diagrams for the illustration of sensitization of the NIR emission from Ni^{2+} and Bi–center by Yb^{3+}, whose $^2F_{5/2}$ level located at around 1000 nm is in resonance (or near resonance) with the $^3T_2$ level of Ni^{2+} and the first excitation state of Bi-center.

In recent years, Yb^{3+} was also used to sensitization the NIR luminescence of ions other than RE ions.83-87 These NIR emitting ions include both TM ions, such as Ni^{2+} and Cu^{2+},83,84,85 and main group emitting centers, such as bismuth,86,87 which has only weak absorption at 980 nm. This type of luminescence material has gained growing interest due to the potential application in photonics. In a recent work demonstrated by Wu et al, 83,84 the emission of Ni^{2+} (pumped at 980 nm) by the transition $^3T_2 \rightarrow {}^3A_2$ centered at 1200 nm was

notably enhanced in the glass–ceramic matrix containing $LiGa_5O_8$ nanocrystals (NCs) after doping of Yb^{3+} (**Fig.** 5). The results of calculation based on ET theory suggests that forwards ET from Yb^{3+} to Ni^{2+} prevails over backward ET from Ni^{2+} to Yb^{3+} and homo–nuclear ET between Yb^{3+} ions, and a critical distance of 1.5 nm is found. In a similar case, Yb^{3+} was used as the sensitizer for the NIR emission of Bi centers in oxide glass, which absorb weakly near 1000 nm.86,87 In a phosphate glass host, the sensitization by Yb^{3+} is again confirmed by emission spectra and the concentration dependence. Under excitation at 980 nm by a diode laser, broadband NIR emission covering 1270–1350 nm is generated, which otherwise is not possible in the absence of Yb^{3+} ions.

3.2 UC and UC enabled by ET between RE ions

UC combines two or more photons of lower energy into a high energy photon, while QC "cuts" a high energy photon into two low energy ones. Both of DC and UC do not violate law of energy conservation and can be produced by making use of ET between RE ions involving transitions between different 4f levels. DC and UC are important optical processes in RE doped materials, and they certainly cannot be simply regarded as the opposite of each other. Reviews on either DC or UC have been published, yet separately.88,89,90 In the following UC and DC are discussed together with the aim to figuring out their similarities as well as difference in both ET mechanisms and related materials.

3.2.1 Ion-ion ET enabled UC

UC here refer to an anti–Stocks emission from activator and this process can have different origins, such as multi–photon absorption, cooperative interaction, ET process and photon avalanche.88,89 ET enables the most efficient UC emission in RE doped materials and that's why these materials are extensively explored for diverse applications.5,88,89 Practically, the most bright UC emission has been observed in Yb^{3+}–RE^{3+} (RE=Er, Tm) activated materials, in which Yb^{3+} again acts as the donor due to its simple energy levels, large absorption cross section and the relatively long lifetime of the only excited state ($^2F_{5/2}$). To be an RE ion that can efficiently accept the energy from Yb^{3+}, first, the activator must has an energy level close to or slightly lower than $^2F_{5/2}$ of Yb^{3+} at around 10000 cm^{-1}. In this regard, RE ions of Pr^{3+} ($^1G_4$), Sm^{3+} ($^6F_{9/2}$), Dy^{3+} ($^6H_{5/2}$), Ho^{3+} ($^5I_6$), Er^{3+} ($^4I_{11/2}$) and Tm^{3+} ($^3H_5$) all can accept the energy from $^2F_{5/2}$ of Yb^{3+} by resonance. Second, the intermediate energy level of the activator should have sufficiently long lifetime to avoid rapid depopulation by radiative or non–radiative decay. This is to ensure high probability of promotion to higher levels by a second ET or excited state absorption. Sm^{3+} and Dy^{3+} are therefore excluded due to the presence of several energy levels below 10000 cm^{-1}. Indeed the UC emission of Yb^{3+}–Nd^{3+}, Sm^{3+}, Dy^{3+} has rarely been reported as they show very low efficiency. **Fig.** 6 presents the energy level alignment for the typical Yb^{3+} sensitized systems, from which the ET process can be understood. For instance, in the Yb^{3+}–Er^{3+} ion pair, after absorption of a 980 nm photon, Yb^{3+} is promoted to the $^2F_{5/2}$ state which transfers the excitation to a nearby Er^{3+} ion, resulting in the population of $^4I_{11/2}$ level. A second step ET or excited state absorption by Er^{3+} promote Er^{3+} to higher levels, from which, after series of phonon assisted relaxation process, red and green UC emission are produced. Moreover, it can be understood easily from the energy level diagram that the red emission from the $^4F_{9/2}$ level and the green emission from $^4S_{3/2}$ (and $^2H_{11/2}$) involve the absorption of two and three photons, respectively (Fig. 6). Besides the first order ET, cooperative ET in which two Yb^{3+} ions transfer energy to one Tb^{3+} cooperatively also results in UC from Tb^{3+},91,92,93,94,95 while the efficiency is orders of magnitude lower than that of the other Yb^{3+}-RE^{3+} ion pairs.88

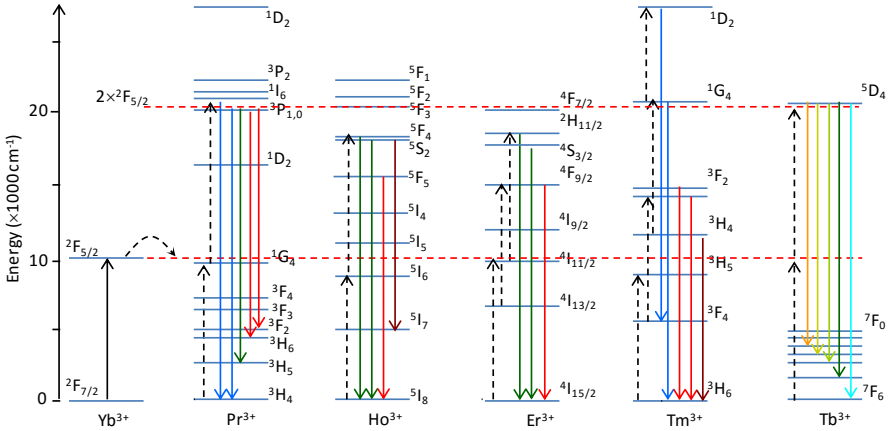

Fig. 6 Energy level diagrams for the illustration of sensitized UC emission in ion pairs of Yb^{3+}–RE^{3+}. The dotted red lines point the energy corresponding to Yb^{3+}: $^2F_{5/2}$ and $2*^2F_{5/2}$. Here, Yb^{3+} with a strong absorption near 1000 nm transfer the excitation energy to Pr^{3+}, Ho^{3+}, Er^{3+} and Tm^{3+}, Er^{3+}, leading to the population of the levels of $^1G_4$ (Pr^{3+}), $^5I_6$ (Ho^{3+}), $^4I_{11/2}$ (Er^{3+}) and $^3H_5$ (Tm^{3+}). The visible emission of these systems are subsequently produced after a further ET process or excited state absorption involving sequential absorption of more than two photons. While for Tb^{3+}, no energy level is in resonance with $^2F_{5/2}$ of Yb^{3+}, the UC emission sensitized by Yb^{3+} is driven by a cooperative mechanism. From this diagram the number of photons involved for different UC emission can be known. Emission and excitation processes in the ions are pointed by solid arrows. Dashed arrows indicate the possible transitions that lead to the UC emission. Non-radiative transitions are not shown here.

In addition to the RE activated materials, UC has also been demonstrated in RE^{3+}–TM^{2+} systems (TM: Ni, Mn, Cr) by Güdel et al. and our group;96,97,98,99,100 while the emission of the TM ions is usually generated in cryostat, implying again the very low UC efficiency. The emissions of TM ions as well as other metal ions normally feature broad band width, which is much larger than that of emission from RE ions.

The UC emission of ion pairs shown in **Fig.** 6 occurs in various inorganic hosts; yet strong emission often favors a host of low phonon energy. This is because the direct decay from the intermediate levels competes with UC process, and this decay is usually accelerated in host with large phonon energy. RE halides are therefore ideal host for UC, such as LaF_3, and $NaYF_4$.101,102,103,104Furthermore, the UC spectra of the same ion pair in different host are also different due to not only the phonon energy but also the crystal structure.

3.2.2 Tuning UC spectra by ET

Management of UC spectra is often desirable to meet special requirement of different applications. Since ET is strongly distance–dependent, the ET enabled UC can be modulated through adjusting the dopant concentration that determines the ion separation. For instance, in a host of $NaYF_4$, Yb^{3+}–RE^{3+} pairs (RE: Er, Tm) produce characteristic emission at green and red region from Er^{3+}, and at blue, red region from Tm^{3+} by 980 nm pumping. It is shown recently that the ratio of green to red emission for Er^{3+} decreases notably with the rise of the concentration of Yb^{3+}.105,106,107 Therefore, almost pure green and red emission by UC is attainable in this system by careful controlling the dopant concentration. This concentration dependence can be rationalized by concentration quenching of green emission due to increased rate of CR via different pathways, which leads to the degradation of excitation energy and the increased population of lower energy levels in samples containing high concentration of dopants.105,106 Similar CR process occurs also in oxide host and pure red UC emission from Er^{3+} is obtained. The spectral tuning of Yb^{3+}–Tm^{3+} pair is based on a similar principle and pure blue and red emission from Tm^{3+} can be generated similarly by controlling the concentration of Yb^{3+} and Tm^{3+}.105,107

3.2.3 Broadband excited UC

For the RE sensitized UC the excitation band widths are inherently narrow and therefore the use of coherent light as excitation is necessary. There have been several attempts to broaden the excitation band width for the UC of RE ions, which may have important practical applications. In the first example, bismuth centers, which has broad absorption at NIR, was employed to sensitize the f–f transition of Ho^{3+} in a glass host. The result shown by Xu et al, 100 clearly indicate the expanding of excitable band widths, compared to that of the Ho^{3+} single doped sample. Broadband excitable UC can be also realized by direct sensitization of the Yb^{3+}–RE^{3+} codoped UC nanoparticles (UCNPs). For instance, an organic dye solution with broad absorption band from red to NIR was employed to sensitize Yb^{3+} doped in the UCNPs of $NaYF_4$:Yb^{3+},Er^{3+} (see **Fig.** 7). Via a two–step ET, i. e., dye→Yb^{3+}→Er^{3+}, the emission of Er^{3+} is successfully produced under excitation from 880 nm to 1000 nm.108 The IR–780 dye does not sensitize the UC emission of NCs because the ET is only observed when the emission spectrum of the dye molecule covers the absorption band of Yb^{3+} (**Fig.** 7). As confirmed by the excitation spectra shown in **Fig.** 7b, the excitation band corresponding to dye molecules centered around 800 nm are much stronger than that of Yb^{3+}, suggesting efficient ET from dye to the NCs.

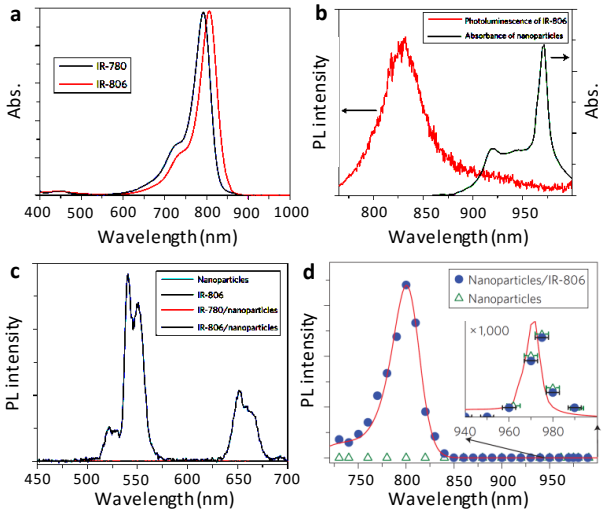

Fig. 7 Dye sensitized broad band UC by $NaYF_4$:Yb^{3+},Er^{3+} NPs. (a) Absorption spectra of the IR–780 and IR–806 dye solutions. (b) PL spectrum of the IR–806 dye solution and the absorption spectrum of the oleylamine–capped UCNPs dispersed in $CHCl_3$. (c) Emission spectra of the NPs solution, IR–806 dye solution, IR–780–NPs solution and the IR–806–NPs solution, under excitation at 980 nm. (d) UC excitation spectra for the NPs and the dye–NPs solution. Reprinted with permission from ref. 108, copyright 2012, Macmillan Publishers Limited.

3.2.4 Ion-ion ET enabled QC

DC, also more widely referred as QC, is often regarded as the opposite of UC process, and DC process is also associated with two different types of ET: the first order ET and the cooperative ET. However, ions pairs that generate efficient UC do not necessarily produce DC emission, and efficient DC materials usually do not guarantee the UC emission as well. In DC process, the first order ET can be in fact considered as a CR process, in which only part of the excitation energy of the donor is used to pump a neighboring ion to its excited state, and the donor ion relaxes to an intermediate excitation state which finally gives the emission of a second photon, or relaxes to the ground state after transferring energy to a second acceptor.

Up to the present, DC based on CR has been observed in a number of ion pairs as long as the energy levels of the donor and acceptor have suitable configurations.90 Among them, the

Gd^{3+}–Eu^{3+} pair is a well–known example which undergoes QC in several hosts.109 Under vacuum UV (VUV) excitation, Gd^{3+} servers as the donor, and it passes part of the excitation energy through the CR process to neighboring Eu^{3+} ions by ^6G_j (Gd^{3+}) + $^7F_0$ (Eu^{3+}) → ^6P_j (Gd^{3+}) + ^5D_j (Eu^{3+}) (step 1, **Fig.** 8a). Afterwards, the Gd^{3+} ion at $^6P_{7/2}$ level can emit itself, or donate the energy to a second Eu^{3+} ion (Step 2, **Fig.** 8a). In a fluoride host $LiGdF_4$:Eu^{3+}, a QE of 170% was reported. Eu^{3+} can be replaced by Tb^{3+} or Er^{3+}, and in the same fluoride host DC emission can be generated.110 Similar as Gd^{3+} ion, Pr^{3+} can also serve as a donor ions in DC process, in which acceptor ion like Cr^{3+} and Mn^{2+} accept energy from Pr^{3+} by a CR process, as shown in **Fig.** 8b,c.111,112,113 It is worth to note that Pr^{3+} itself has been known as an ion capable of QC by means of sequential cascade emissions by $^1S_0$ → $^3P_0$ and $^3P_0$ → $3H_4$.112The only requirement to generate CR in Pr^{3+} ions is that the position of the 4f5d band should be higher than the $^1S_0$ level in the selected host. In the CR of Pr^{3+}–TM (TM: Cr^{3+}, Mn^{2+}) pair, the first ET step populates the $^3P_0$ (Pr^{3+}) level, from which either a second ET to TM ions or the emission by ^3P_j → $^3H_4$ can occur. 111,113 In a similar fashion, DC emission in the NIR by Yb^{3+} can be produced based on CR by selecting RE ion pairs with suitable energy levels. Ion pairs with efficient UC emission given in **Fig.** 8 are natural choice. In fact, the efficient UC pairs shown in **Fig.** 8 all have shown experimentally to be capable of QC by a CR process, regardless of the host. 90,114,115,116,117 However, to minimize the possibility of backward ET from Yb^{3+}, the donor ions should have energy levels located at positions slightly higher than that of $^2F_{5/2}$ (Yb^{3+}). This is why Pr^{3+} and Nd^{3+} can sensitize more efficiently Yb^{3+} in the DC process based on the CR mechanism, similar to the case of Gd^{3+}–Eu^{3+} pair (**Fig.** 8d,e),116,117while Er^{3+} and Tm^{3+} are less efficient as donor for DC due to enhanced rate of backward ET (from Yb^{3+} to Er^{3+} or Tm^{3+} as in the UC process). NIR QC can also be generated based on homo–nuclear CR process. To the present, the only know example is the Tm^{3+} ion, which produced two 1800 nm photons out of each 800 nm photon absorbed by a CR process: $^3H_4$ (Tm^{3+}–1) + $^3H_6$ (Tm^{3+}–2) → $^3F_4$ (Tm^{3+}–1) + $^3F_6$ (Tm^{3+}–2).118,119,120

3.2.5 Cooperative QC and controversies

Similar to the cooperative UC process, the observation of cooperative QC has been claimed by many researchers in different Yb^{3+}–RE^{3+} codoped materials.90 Despite its early theoretical prediction made by Dexter in 1950s,31,32 its experimental observation was made by Meijerink et al until 2005 in Tb^{3+}–Yb^{3+} codoped YPO_4.121 In this report, cooperative ET from Tb^{3+} to Yb^{3+} is confirmed by steady state excitation/emission spectroscopy (**Fig.** 9). Due to the absence of intermediate energy levels matching that of $^2F_{5/2}$ (Yb^{3+}), a cooperative ET process is suggested and this mechanism is supported by numerical modelling. Later, a variety of materials doped with RE^{3+}–Yb^{3+} (RE= Ce, Pr, Er, Tm…) have been reported to show cooperative DC similar as that of the Tb^{3+}–Yb^{3+} case. 90,122,123,124,125,126,127 We list in Table S3 the examples of cooperative DC reported in recent years for the Yb^{3+}–M pairs, where M can be RE, TM ions and other types of optical centers. In these reports, only few authors discuss the unexpectedly low external quantum efficiency (EQE) for the cooperative QC. 128

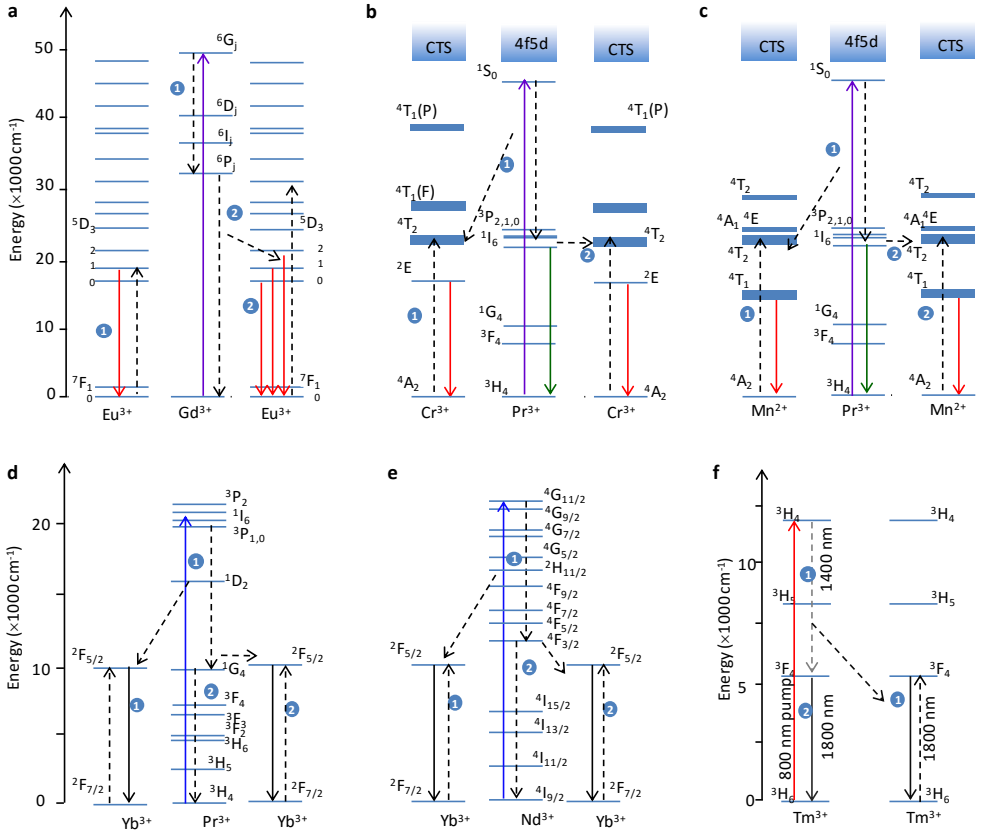

Fig. 8 Energy level diagrams for the illustration of QC by CR in ion pairs of (a) Gd^{3+}–Eu^{3+}, (b) Pr^{3+}–Cr^{3+}, (c) Pr^{3+}–Mn^{2+}, (d) Pr^{3+}–Yb^{3+}, (e) Nd^{3+}–Yb^{3+} and Tm^{3+}–Tm^{3+}. Visible QC is produced in phosphors activated with the first three ion pairs (a–c), whereas NIR QC by the emission of Yb^{3+} and Tm^{3+} is produced by the other three ion pairs (d–f). In Tm^{3+} doped materials, homo–nuclear ET between Tm^{3+} ions occurs, i.e., Tm^{3+} ions act as both donor and acceptor. For the pairs containing only RE ions (a, d–f), QC occurs almost independent of the host. Solid arrows point the transitions in excitation and emission process, and dashed arrows are the transition involved in ET process. Non-radiative processes are not shown.

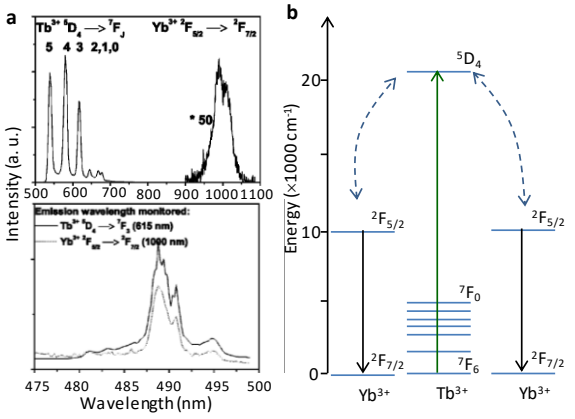

Fig. 9 Cooperative DC emission in YPO_4:Tb^{3+},Yb^{3+}. (a) emission spectra (top) recorded by pumping the $^5D_4$ level Tb3+ at 489 nm, and excitation spectra (bottom) monitoring the emission of Tb^{3+} (515 nm) and Yb^{3+} (1000 nm) (b) Energy level diagram illustrating the cooperative ET from Tb^{3+} to Yb^{3+}. In the cooperative process, two Yb3+ ions are simultaneously sensitized by Tb^{3+}, resulting in the emission of two NIR photons for each absorbed visible photon. Reprinted with permission from ref. 121, copyright 2005, American Physical Society.

Controversies therefore arise regarding the mechanism of cooperative ET from RE^{3+} to Yb^{3+} in the reported DC materials. In addition to the observed low EQE values, there are increased number of evidences against the cooperative ET and the QC process. 128 Unlike the Tb^{3+}–Yb^{3+} pair, RE ions, such as Tm^{3+} and Pr^{3+}, have several energy levels spanning from 0–11000 cm^{-1}, thus a cooperative mechanism might be less favoured. In fact, numerical modelling indicate that, at least for the Pr^{3+}–Yb^{3+} pair, a first order ET by CR is more likely (see Fig. 8). As for the Ce^{3+}–Yb^{3+} and Eu^{2+}–Yb^{3+} where d–f transition of the donor enables a broadband excitation band for NIR emission, the cooperative ET mechanism is also questionable due to the low EQE and presence of different relaxation pathways. In addition, for Ce^{3+}–Yb^{3+} a metal to metal charge transfer could probably occur, by, for instance, Yb^{3+} + Ce^{3+} → Yb^{2+} + Ce^{4+}.61,128,129 This process provides additional quenching pathways for the Ce^{3+}–Yb^{3+} and Eu^{2+}–Yb^{3+} doped materials. On the other hand, excitation of Yb^{3+} at its charge transfer band located in the UV also leads to the NIR emission, which, certainly, is a one–photon process with large Stocks shift, and it cannot be ascribed to the cooperative

mechanism.130,131 Therefore, the sensitization of the NIR emission of Yb^{3+} in the visible remains to be elucidated in a clearer manner from both experiment and theory.

3.3 Managing ion-ion ET in nanostructures

RE doped nanoparticles and nanoarchitectures have gained growing interest in recent years due to their robust emission and diverse applications.5,132-134 When the dimension of the structure is reduced to the size comparable to the critical distance of ET, the modulation of ET can be possible by structural design at nanoscale, as demonstrated in the different types of core–shell structures.

3.3.1 ET in nanoparticles

Similar to their bulk counterparts ET transfer has been intensively examined at nanoscale in various RE and TM activated systems. This is especially benefited by the development of wet–chemistry synthesis in recent years that offers unprecedentedly easy access to different single crystalline nanoparticles as well as nanoscale systems with controlled size and architecture. Since the critical distance for ET is in the order of several nanometers, the size of the nanostructure might be a new parameter for the control of ET in confined space. As inorganic nanocrystals (NCs) doped with RE ions are considered as robust fluorescence labels for bio–imaging, they produced regular down-shifted emission and UC, in which ET dominate the emission properties. A thorough discussion of these systems is not needed here as the synthesis and applications of these nanomaterials have been summarized in several excellent recent reviews.132,133,134

3.3.2 Engineering ET in core–shell architectures

In nanoscale systems with engineered architectures accessed by different synthetic process, ET in a confined manner can be controlled between ions and between heterostructures, which are not amenable to bulk materials. This is often realized by a core–shell design where the core and shell are doped with different ions to spatially confine the ET between target ions.135 For instance, in a LaF_3 based core–shell system, Eu^{3+} and Tb^{3+} ions located respectively in the core and shell are separated by a shell of undoped LaF_3. It is demonstrated that by varying the thickness of the LaF_3 layer, the ET between Eu^{3+} and Tb^{3+} can be controlled to allow partial or complete ET, such that the ratio of Tb^{3+} and Eu^{3+} emission can be finely tuned.135,136,137The core–shell structure therefore can be employed to manipulate spectral features for multi–ion activated materials by modulation the interaction between ions in the nanostructure.

This core-shell design is particularly useful for building three or four–ion activated nanosystems, where ET has to be properly controlled between targeted ions in the structure to avoid undesirable ion-ion coupling. As demonstrated in a recent work by Liu et al, 138 in the matrix of $NaGdF_4$, Yb^{3+}–Tm^{3+} pair is incorporated in the core, and Eu^{3+} is doped at the shell of the same matrix. Under excitation by 980 nm, multi–step ET occurs from core to shell mediated by Gd^{3+} in the direction of Yb^{3+}(core) $\rightarrow$$Tm^{3+}$(core) $\rightarrow$$Gd^{3+}$(core and shell) $\rightarrow$$Eu^{3+}$(shell), resulting in the strong red emission from Eu^{3+}. Eu^{3+} can be replaced by ions of Sm^{3+}, Dy^{3+} or Tb^{3+}, which give visible UC emissions based on a similar core to shell two–step ET process. Without the core–shell design that separate different ions, the UC emission of Eu^{3+} in the four–ion system is definitely impossible because the unavoidable coupling among the four ions could result in the quenching of all the emissions.

The core–shell nano–architectures also facilitate the modulation of UC emission spectra under continuous wave (c.w.) and pulse laser pumping. In a recent report by Liu's group (Fig. 10), 139 the ET between the dopant ions was found to be controllable by adjusting the pulse duration of the excitation laser in a core–shell nanostructure. Using pulse duration from 0.2 ms to 6 ms for the excitation (at 980 nm), the intensity ratio of green to red emission from the shell of $NaYF_4$:Yb^{3+}, Ho^{3+}, Ce^{3+} can be continuously modulated (Fig. 10b). As shown in **Fig.** 10c, after excitation and sensitization by Yb^{3+} the ET from Ho^{3+} to Ce^{3+} (by a CR process: $^5I_6$ (Ho^{3+}) + $^2F_{5/2}$ (Ce^{3+}) $\rightarrow$ $^5I_7$ (Ho^{3+}) + $^2F_{7/2}$ (Ce^{3+})is only allowed under excitation by long pulse. Under short pulse excitation, the transition from $^5I_6$ (Ho^{3+}) to higher levels of $^5F_4$, $^5S_2$ prevails over the above CR process involving Ce^{3+}. Furthermore, in addition to pure red and green emission this judicious design also allows for the generation of pure blue UC emission by pumping at 800 nm. The blue emission is produced as a result of ET from the core to the first shell by $Nd^{3+} \rightarrow Yb^{3+} \rightarrow Tm^{3+}$. Excitation at 980 nm cannot produce blue emission from the core as the excitation light cannot reach the shell doped with Yb^{3+} and Tm^{3+} ions due to adsorption by the Yb^{3+} ions doped in the third shell $NaYF_4$:Yb^{3+}, Ho^{3+}, Ce^{3+}.

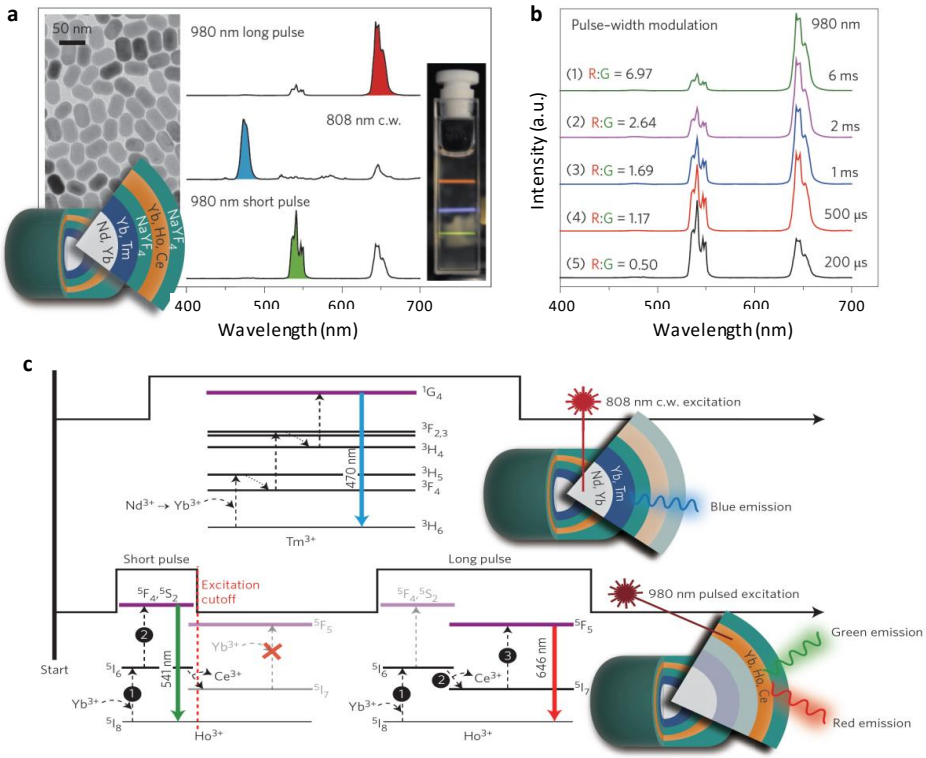

Fig. 10 Controlling ET and UC spectra in core–multishell NPs by pulse laser excitation. (a) UC emission spectra of the NPs under excitation by long and short pulse at 808 nm and 980 nm. The corresponding photograph of the colloidal dispersion of NPs under excitation by different lasers is shown in the right. TEM image and the structure of the core–shell NPs are shown in the left. (b) Emission spectra of the NPs under excitation by pulse 980 nm laser of different pulse duration. (c) Schematic illustration of the excitation and ET mechanisms under C.W. and pulse excitation. The 808 nm c.w. laser only excites Nd^{3+} and triggers ET from Nd^{3+} to Yb^{3+}, resulting in the blue emission from Tm^{3+}. The 980 nm short pulse only produce green UC emission (from $^5F_4$, $^5S_2$) because Ho^{3+} cannot be promoted to the $^5F_5$ level due to short pulse duration. Reprinted with permission from Ref. 139, Copyright 2015, Macmillan Publishers Limited.

3.4 QDs-ion ET

QDs, with the quantized exciton levels, become an important class of luminescent materials due to their intriguing optical properties. They can also serve as efficient donor centers to sensitize the emission of RE and ions as long as resonance condition is fulfilled. In general ET from QD to ions can occur in two different fashions: host sensitized ET and space separated ET.

3.4.1 ET in RE-doped QDs

Semiconductors such as metal sulphides and nitrides have also been employed as luminescent host for the doping of activators including both TM and RE ions in the recent decades. The use of semiconductor host made possible the extension of excitation band of most RE ions and TM ions to the near UV and visible region, offering new possibilities for optoelectronic devices. With the rapid advance in semiconductor QDs, the use of QDs as hosts for TM or RE ions have also been exploited and the ET from QD to TM or RE ions has been gaining interest in recent years.140,141

Compound semiconductors provide tetrahedral cationic site that are suitable for doping with TM ions, such as Mn^{2+} and Cu^{+} (see Table S1). For a long time Mn^{2+} activated materials have been used as green or red phosphors depending on the local coordination environments.62 Mn^{2+} with 3d5 electronic configuration has only weak absorption bands from UV to the visible range, which therefore necessitate the use of a suitable host to sensitize its luminescence. Binary compounds containing TM metal ions with d10 configuration are ideal candidate for isovalent doping with Mn^{2+}. For instance, in the wide band gap semiconductor ZnS (E_g = 3.6 eV), the $^4T_1 \rightarrow {}^6A_1$ transition that gives orange–red emission is efficiently generated under excitation with UV light. By down–size the particle to the nanoscale, it was found by Bhargava et al that the emission rate is enhanced by a factor of 5 for nanosized ZnS:Mn without large loss of quantum efficiency.142,143 This result was interpreted in terms of enhanced interaction of the sp–d orbitals between the host and the dopant in the nanoscale particles as compared to bulk materials. Ions of 3d TM other than Mn^{2+} have also been doped into the lattices of different compound semiconductors. Monovalent Cu^{+} ion is another well–known luminescent ion, which has a closed shell d10 configuration and gives blue–

green emission by transition of $3d^{10} \rightarrow 3d^{9}4s^{1}$ in both oxide and chalcogenides hosts.144,145 In both the bulk and nanocrystalline chalcogenide semiconductors, Cu^{+} taken the divalent cationic site and its blue–green emission can be sensitized by the host excitons under UV excitation.146,147

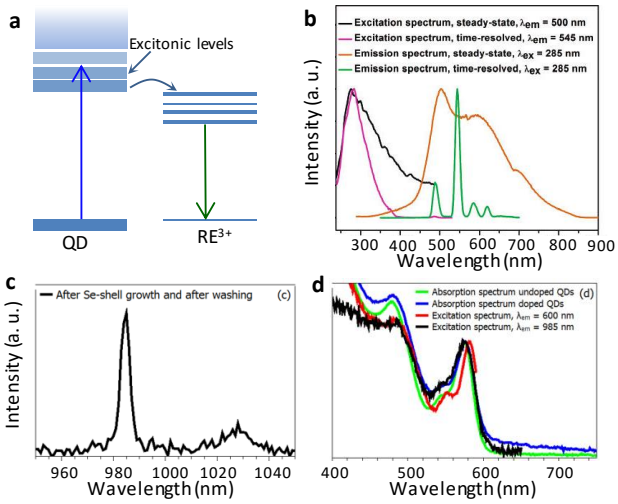

Fig. 11 Host sensitized emission of RE ions in CdSe:RE^{3+}. (a) Schematic diagram for the ET from QD excitonic levels to 4f levels of RE^{3+} ions. (b) Steady state and time resolved spectra for CdSe:Tb^{3+}. Due to the short lifetime, the excitonic emission of the CdSe is not observed in the time–resolved spectrum (recorded after 200 µs interval). (c) NIR emission from Yb^{3+} of CdSe:Yb^{3+} by excitation at 580 nm. (d) Absorption spectra of CdSe QDS and the excitation spectra for the excitonic emission at 600 nm and NIR emission from Yb^{3+}. Reprinted from Refs. 152 and 154, copyright 2005, 2013, American Chemical Society.

Unlike bivalent 3d TM ions, aliovalent doping of RE^{3+} ions into semiconductors at their bivalent (or trivalent) cationic sites of highly covalent nature is difficult at equilibrium state, let along the large difference in electronegativity and ionic size. Successful doping of RE ions like Er^{3+}, however has been claimed in many recent reports for sulphide and nitride semiconductors in both bulk and nanoscale form.148,149,150,151,152,153,154 In many of these reports, discussion of possible ET from the host to the RE based on the spectral overlap is not provided. Until recently, based on a delicate wet-chemistry process, the incorporation of a RE ions into a chalcogenide QDs at the particle surface was realized by Chengelis et al. for a CdSe:Tb^{3+} system with a core–shell design.152The presence of ET from the QDs to Tb^{3+} was confirmed by both steady state and time resolved spectra (**Fig.** 11). Likewise, in a recent report from Meijerink's group, Yb^{3+} ions were incorporated onto surfaces of CdSe QDs using a well–designed wet–chemistry procedure, and the NIR emission of Yb^{3+} near 1000 nm (by $^{2}F_{5/2} \rightarrow {}^{2}F_{7/2}$) is efficiently sensitized by QDs (**Fig.** 11c,d).154 In order to avoid the difficulties faced by incorporation of RE ions, chalcogenide semiconductors containing cationic sites of RE or larger alkali earth ion that can accommodate trivalent RE ions were examined. For instance, by resorting to host of CaS (or SrS) RE ions can be easily incorporated and emission of RE ions can be easily sensitized by the host.155 In spite of the concern on hydroscopicity and stability, these materials still gains much interest due to potential applications in white–light LEDs and other areas.

3.4.2 Space separated ET and QC in QD–RE pairs

Besides the exciton–ion and ion–ion ET in a single host as discussed above, the interactions between ion and QDs or between two QDs also leads to similar optical ET as long as energy resonance condition is fulfilled. QDs, for instance, have been shown to transfer energy to neighboring RE ions or QD. Obviously, this is different from the previous case of host sensitized luminescence by semiconductors where RE ions are believed to occupy the cationic site in QDs. For instance, this QD–ion ET happens in an Er^{3+}–implanted SiO_2 matrix with dispersed Si QDs (**Fig.** 12). At a certain concentration when separation between Er^{3+} ions and Si QDs is comparable to the critical distance ET, the NIR emission from Er^{3+} near 1550 nm is efficiently sensitized by Si QDs, such that the Er^{3+} can be excited at a broad spectral range in the visible.155156,157 The ET from Si QDs to Er^{3+} has been intensively examined by using high–resolution PL, two–color spectroscopy, time–resolved spectroscopy and analysed by simulation.158,159,160 It was found that Er^{3+} emission can be produced by resonant pumping into the bound exciton state of the donor (Si QDs). According to the model proposed by Izeddin et al.,159,160 the minimal energy required to produce the bound excitons (around 1.02 eV) equals the sum of Er^{3+} excitation (0.8 eV) and the ionization energy of the exciton (0.218 eV), which is in agreement with the excitation spectra for the Er^{3+} emission. 159 Due to the presence of both forward and backward ET the emission of Er^{3+} can be notably quenched by Si QDs, which might be explored further for modulation of Er^{3+} emission in the gigahertz region.160

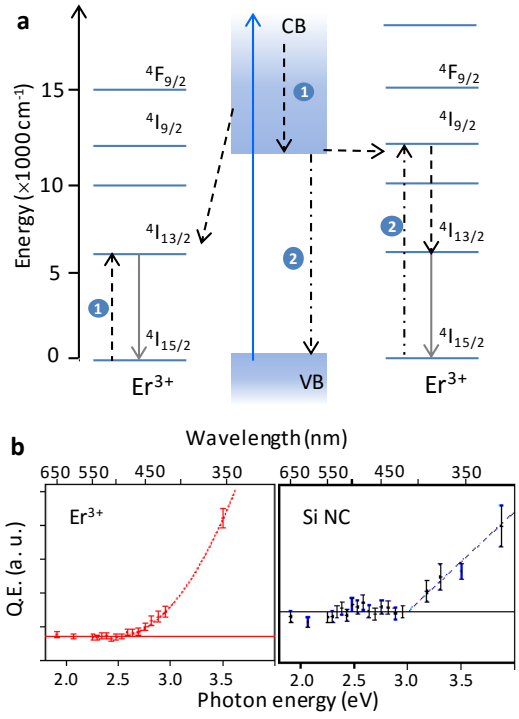

Fig. 12 Space-separated ET from Si QDs to Er^{3+} ions in a SiO_2 matrix. (a) Energy diagram for the illustration of ET from Si QDs to Er^{3+} ions in amorphous SiO_2 matrix. Under

sufficiently high energy excitation, electrons being promoted to CB of Si donate part of its energy to neighboring Er^{3+} ions, by an Auger–like process. The electrons at the bottom of the conduction band can pass the energy to another Er^{3+}, or emit by electron–hole recombination. (b) Quantum efficiency (Q. E.) as a function of excitation energy for (left) Er^{3+} and (right) Si NCs. Reprinted with permission from Ref. 157, copyright 2008, Macmillan Publishers Limited.

Furthermore, it was found that the Er^{3+}–Si QDs system undergoes DC via ET based on a mechanism similar to that of CR in RE ion pairs,157 which is connected with the CM process in QDs, as described below. As shown in **Fig.** 12, electrons being promoted to a high position in conduction band relax first to the bottom of the CB by passing the excessive energy to a nearby Er^{3+}. This can be considered as an Auger–like process by intra–band relaxation in which hot electrons cool down by exciting nearby Er^{3+} ions. Based on a detailed spectroscopic examination, nearly 50% of all Er^{3+} ions are within the effective range of this interaction. A second ET can excite another Er^{3+}, thus producing two NIR photons by Er^{3+} after absorption of one photon by Si QD. When the excitation energy is higher than the threshold (around 2.5 eV, two times of the band gap energy of Si), the QE increases abruptly with the excitation photon energy (Fig. 12b,c). This threshold energy matches the energy of CM in Si QDs, suggesting the possibility of harvesting multiple excitons by RE ions. From a recent report on the measurement of the external QE (EQE), a 15–fold enhancement of EQE was found at high excitation photon energy around 4.2 eV (as compared to excitation energy < 2.0 eV).161 This result again substantiates that efficient extract of hot carriers of Si QDs by nearby Er^{3+} ions in spite of low EQE due to fast Auger recombination. In a similar fashion, the hot carriers can be also harvested by other RE ions emitting in the NIR (such as Nd^{3+}), resulting in the steep growth in QE and broad band excited NIR emission.162

3.5 QC beyond RE ions: ET in CM and SF

As discussed above, ET between RE or TM ions in a CR pathway doubles the photon yield. Analogously, a similar CR process occurs in QDs as well as large number of organic molecules, leading to multiple exciton generation known as CM in QDs, and SF in organic molecules.

3.5.1 CM and SF: from perspective of ET

Similar as the QC process by ion–ion interaction in solids, QDs undergo multiple exciton generation after being excited. A process is known as CM which is mechanistically analogous to CR between ions, as discussed in section 3.2.163 CM in a variety of semiconductor QDs under high energy excitation also features an internal quantum efficiency (IQE) for exciton generation of greater than 1.163-169 The highly efficient generation of photoelectron is associated with the Auger process in semiconductors as shown in **Fig.** 13. When a "hot" electron with high energy produced immediately after excitation relaxes by intra–band transition to the bottom of the conduction band, the energy released by the relaxation meanwhile promotes another electron in the valence band to the conduction band, leading to multiple carrier generation. High order process that result in the generation of more than two excitons by absorption of each UV photon has also been observed by pump–probe experiment and it is considered to be related with a similar mechanism, as illustrated in **Fig.** 13. The threshold excitation energy for CM for different QDs are typically slightly higher than $2E_g$ (E_g: bandgap) and the typical QE for multiple exciton generation can be over 300% for lead chalcogenide. Beside lead based QDs, CM has also been observed a variety of other QDs, including selenide, arsenide, Si, and Ge QDs.164,169

However, CM often does not finally lead to efficient photon emission through recombination of excitons in most QDs. Especially, in the lead based QDs with small band gaps the recombination of excitons are very fast, preventing the observation of PL in most experiment. Method for the harvesting of these multiple exciton are therefore important from viewpoint of practical application, which is to be discussed in section 4.2.4. Direct experimental confirmation of PL QE enhancement due to CM was made by Timmerman et al in Si QDs,170,171 which exhibited a stepwise increase of QE with the rise of excitation photon energy. For the excitation photon energy of 4.5 eV, QE of around 2.5 was observed. This character is especially attractive for the enhancement of power conversion efficiency (PCE) in photovoltaic (PV) devices.

Along with the experimental advances, the multiple exciton generation process has been examined theoretically using ab initio method. Simulations showed that CM favours QDs of smaller size as the CM lifetime is enhanced by size reduction due to enhanced quantum confinement effect. Furthermore, in the presence of neighbouring QDs, CM can involve the simultaneous participation of two QDs due to delocalization of the wavefunctions, resulting in the generation of two excitons localized in two QDs that is similar to the CR process occurring in RE ions. The two–site CM occurs either by a SSQC (space separated QC) or CDCT (Coulomb–driven charge transfer) mechanism. The lifetime of SSQC was found to enhance notably with inter–particle separation, which consists with the experimental observation on Si QDs.172 In a more recent theoretical study, it is revealed that the interaction between the QDs can result in the reduction in the threshold for CM, again due to the delocalization of wavefunctions. In particular, according to the exciton recycling mechanism implemented in their model, Auger recombination is consider to re–excite the carriers to above the CM threshold, which is compatible with experimental results. In this case, the generation of multiple excitons distributed in nearby QDs becomes dominating when the rate of Auger cycling is higher than that of exciton recombination.173

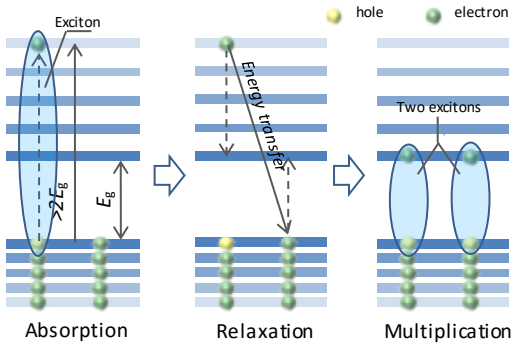

Fig. 13 CM in semiconductor QDs. Under high energy ($h\nu>2E_g$) excitation, an electron being promoted to the higher level in the conduction band pass the "excessive" energy to another electron in the valence band subsequently, meanwhile itself sinks to the bottom of the conduction band. This Auger process finally results in the generation of two electron–hole pairs (exciton) with the absorption of one photon. Multiple carrier generation occurs by a similar mechanism.

As an analogue to the multiple exciton generation in inorganic QDs, SF occurs in certain organic compound which yields two excitons per photon (**Fig.** 14).57,174 Upon UV excitation, the molecule is promoted to the spin singlet excitation state (S=0) from the singlet ground state, generating spin singlet excitons. The recombination of singlet excitons is spin–allowed, resulting in the visible emission. This process is in competition with the fission of the singlet exciton into two triplet excitons, which is also spin allowed and occurs in time scale of 100 pico–seconds, much faster than the emission process. From the view point of ET, the SF process can be understood based on a CR process involving two nearby molecules by M1(S1) + M2(S0) $\rightarrow$ M1(T1) + M2(T1) (Fig. 14).175 For molecules with efficient SF, one generally finds that 2E(T1) $\leqslant$ E(S1). The spin triplet excitons are however not emissive because the transition to spin singlet ground state is spin–forbidden. These triplet excitons therefore have relatively long lifetime and gives only weak phosphorescence or no emission. From the discussions above, the differences and similarities by comparing CM and SF are quite obvious: CM normally occurs within one QD while SF involved two neighbouring interacting molecules.

Polyacenes, such as pentacene, have been known for a long time to undergo SF. However, practical applications of these molecules have been largely hindered due to their poor stability, high cost and low absolute efficiency. There is continuous theoretical and experimental effort devoted to the searching of new SF molecules with better performance and the understanding of the SF mechanisms.176,177 As pointed out in the work of Nozik et al., 178 efficient SF not only relies on the molecular structure but also on the inter–molecular coupling. General theoretical consideration suggests that bi-radical molecules may also serves as the basis for SF molecules in which the low–lying triplet state could satisfy the condition 2E(T1) $\leqslant$ E(S1). Besides having the right molecular structure, to enable SF the two molecules have to be correctly coupled as SF involves two molecules. Cofacial stacking commonly found in molecular crystals is favorable for efficient SF. In addition, the coupling of two molecules can be also mediated through a virtual radical cation/anion state or a charge transfer state.

3.5.2 ET from spin triplet excitons to QDs

Recently, harvesting of these spin triplet dark excitons becomes attractive as this offers a possibility to double the PCE in organic PV devices.179,180 In order to harvest the triplet excitons by ET resonance conditions should be met first. QDs with proper band structure have been shown to be a very effective energy harvester for the spin triplet excitons situated in dark states. As demonstrated in two recent examples, the emission of lead sulphide and selenide QDs were sensitized by the triplet excitons from tetracene and pentacene, respectively. 181,182 Based on both steady state and transient state spectroscopy, the ET from the organic semiconductor to QDs was confirmed and an overall quantum efficiency (QE) greater than unity was found. This triplet to QD ET process therefore offers another pathway to QC (**Fig.** 14), which is totally different from the cooperative mechanism and the CR process described in sections above.

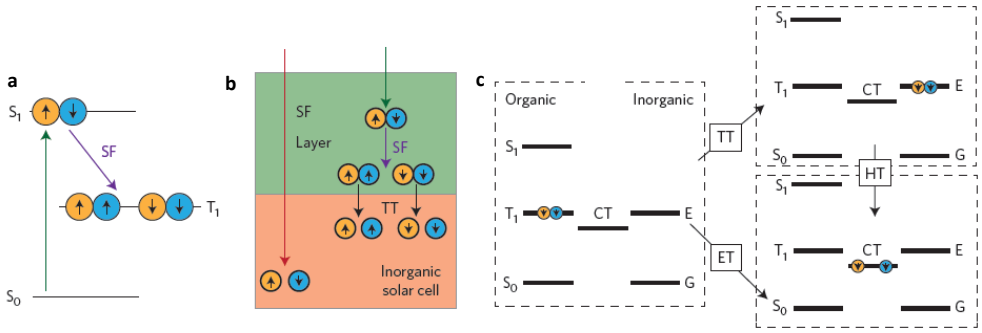

Fig. 14 Schematic representation of singlet exciton fission and triplet ET to QDs. (a) Generation of spin singlet exciton (consisting of electron and hole of opposite spins) by photoexcitation (green arrow), and fission of singlet exciton into two spin triplet excitons (within period of < 100 Ps) with energy located in T1 (triplet energy state). (b) Electronic ET from the organic to the inorganic QD layer mediated by spin triplet excitons. (c) Two possible ET mechanisms from spin triplet excitons to QDs: the direct electron transfer (ET) and the triplet transfer (TT). CT denotes the charge transfer state, and G and E are the ground and excited states of the QD, respectively. Reprinted with permission from **Ref. 181**, copyright 2014, Macmillan Publishers Limited.

3.6 ET involving 2D materials

3.6.1 ET between graphene and QDs

In recent years, there are growing interest in the applications of graphene and other 2D materials in photonics as well as photovoltaics areas due to their intriguing optical and electric properties.183,184,185 Therefore, optical interaction of these 2D materials with fluorescent centers, such as molecules and QDs has been paid special attention. Graphene, the single layer sp2 carbon, absorbs about ~2% of the incoming light, almost independent of the wavelength of light in the entire visible and NIR region.186 Similar to metal surfaces, graphene quenches the fluorescence of molecules placed nearby by resonance ET. However, as we discussed in section 2, ET rate strongly depends on the geometry of the D–A pair, and conventional Förster theory on ET is no longer valid if ET cannot be treated by point dipole approximation.

ET from molecules to graphene was first theoretically examined by Swathi et al employing a tight–binding model for the pi–system and the Dirac cone approximation for graphene.187,188,189,190 They derived an analytic expression for the rate of ET from dye molecule to graphene, which is totally different from the R^{-6} dependence as found for Förster type ET. Their calculation suggests that the ET occurs within far large molecule–graphene separations (up to 30 nm) than that of conventional ET (less than 10 nm). Furthermore, at long separations the ET rate follows R^{-4} dependence on the separation, same as the ET between molecule and metal surface (see section 2.2.5).188

The theories have found good agreement with the experimental observations made in recent years. For dye molecules, the R^{-4} dependence of ET rate is experimentally confirmed by Gaudreau et al using TiO_2 as the separation layer between graphene and Rhodamine.191 At a distance of 5 nm, the decay rate of Rhodamine is enhanced by 90 times due to ET to graphene. Brus's group made the first experimental observation on ET from CdSe/ZnS core/shell QDs to graphene.192 Their results demonstrate that single layer graphene quenches the PL of QDs by a factor of 70 and an ET rate of 4 ns^{-1} is found. With the increase in the number of graphene layer the ET rate increases notably, approaching the bulk limit. For ET between graphene–semiconductor nanostructure, distance dependence of ET rate is correlated with the geometry of the acceptor, because the point dipole approximation valid only for QDs. For instance, Federspiel et al showed that the R^{-4} scaling is only valid in the ET between graphene–QDs.193 The distance dependence of ET from CdSe/CdS/ZnS nanoplatelets (NPLs) to graphene deviates from the R^{-4} especially for short distance d < 5 nm (see Fig. 15b). When the semiconductor nanoplates is replaced with a 2D quantum well, the distance dependence will be changed to a R^{-2} scaling according to theory (see section 2.2.5).194 This relation is indeed experimentally confirmed in the graphene–InGaN using GaN as the separation layer, and this relation prevails at a wide temperature range despite that the ET efficiency changes.194,195

Graphene as a 2D material with zero density of states at Femi level allows the tuning of its band structure around the Dirac point by electric field. By applying an external bias the electron filling can be electrically modulated, offering a new pathway to control ET to graphene. Lee et al are the first to demonstrate this strategy for the control of ET from QDs to graphene using PMMA as the spacing layer.196 At a gate voltage of higher than ~4V, the ET to graphene is suppressed and the PL of QD is restored. It is reasonable that the effective modulation voltage should be higher than the optical band gap of the QDs. Furthermore, due to reduced ET efficiency the modulation magnitude decreases notably with the increasing in the thickness of the PMMA spacing layer.

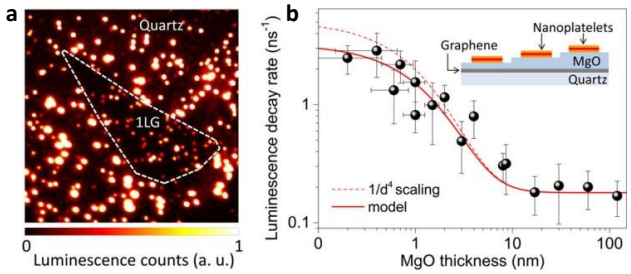

Fig. 15 ET between graphene and semiconductor nanoplates. (a) PL image of CdSe/CdS/ZnS nanoplates covering a single layer graphene, showing that the PL of nanoplates is effectively quenched by the graphene. (b) Dependence of decay rates on the separation (the thickness of MgO layer) between graphene and nanoplates. Deviation from the d^{-4} scaling is found for short graphene-NPL separation. Inset is the structure of the sample. Reprinted with permission from ref. 193, copyright 2015, American Chemical Society.

3.6.2 ET between MoS_2 and QDs

In comparison to graphene which is gapless, TM dichalcogenides, such as MoS_2, have band gaps in the optical frequency and their luminescence is drastically enhanced when thinned down to monolayer, as a result of transition from indirect to direct band gap.197,198,199 The coupling of 2D TM dichalcogenide with luminescent nanomaterials becomes of special interest for the study of ET in nanoscale. Prins et al examined the ET between CdSe QDs and MoS_2 of different thickness.200 In the system examined, colloids QDs were deposited onto a flake of MoS_2 of varying thickness on a silicon substrate (see Fig. 16). The emission peak of QDs centered at 1.95 eV is completely covered by excitonic absorption of MoS_2, thus enabling efficiency ET from QDs to MoS_2. The pictures shown in Fig. 16 suggest that the ET rate is enhanced with the decrease of layer thickness, and the maximal ET efficiency is 95% for single layer MoS_2. This thickness dependence of ET rate is completely counterintuitive as compared to that of the QD–graphene system discussed above, in which ET rate is enhanced with the increase in number of graphene layers. However, as MoS_2 is dielectric rather than conductive, the authors interpreted the enhanced ET in terms of reduced dielectric screen for monolayer MoS_2. A nice agreement is found between the thickness dependence of ET rate and the continuum model developed by Gordon et al. based on anisotropic permittivity.201

Similar to the graphene–QD system, the ET rate from QDs to the 2D semiconductor MoS_2 can be also modulated through the application of external voltage. In the device made by Prasai et al.,202 a thin film of CdSe/CdS core–shell QDs was covered by MoS_2 layer. By applying voltage to MoS_2 layer, the PL of the MoS_2–QDs device can be continuously modulated at the voltage range from –2V to 2V, implying the change in the ET rate at different voltages. At –2V, the PL of MoS_2 reached maximum value, while the PL of QDs is maximal at 2V, where the ET rate is minimal. The change of ET rate is interpreted in terms of the electric field modulation of excitonic absorption of MoS_2. The device gives a PL modulation efficiency of 75% and the authors believe the method can be extendable to other QD/2D semiconductor combinations.

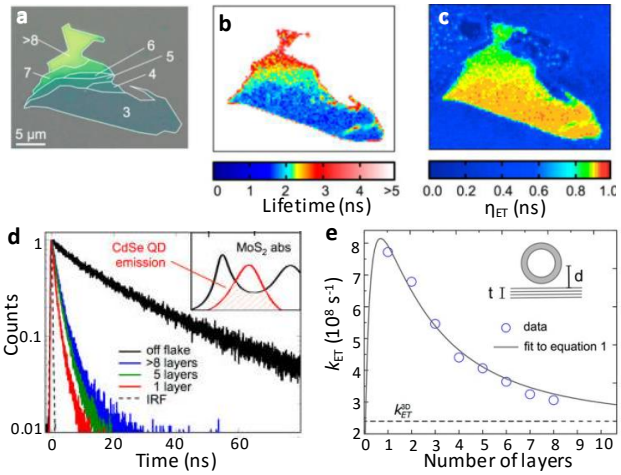

Fig. 16 ET between MoS_2 layers and QDs. (a) Optical image of a MoS_2 plates prepared by mechanical exfoliation. (b) Fluorescence lifetime mapping for CdSe/CdZnS QDs covering the same MoS_2 sample. The change in color indicates the difference in lifetime. (c) ET efficiency calculated from the lifetime shown in b. (d) Fluorescence decay curves for QDs taken on positions with different thickness of MoS_2. (e) ET rate as a function of number of layers. Blue circles are the experimental values and the fitting result is shown as the solid line. The dashed line points the ET rate to bulk MoS_2. Inset shows a schematic representation for the MoS_2–QD and the definition for t and d. Reprinted with permission from ref. 200, copyright 2015, American Chemical Society.

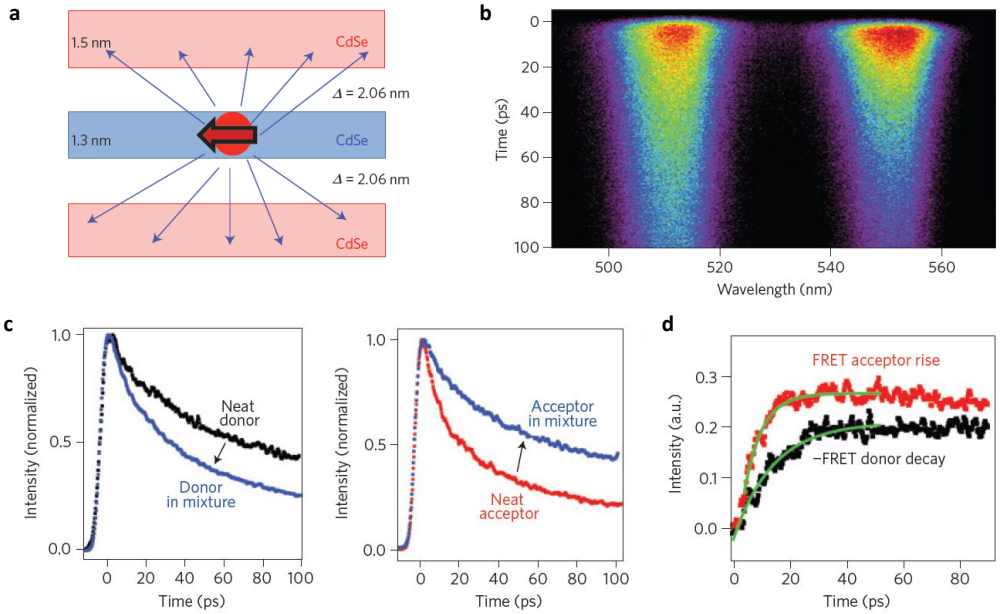

Fig. 17 ET in 2D arrays of CdSe nanoplatelets. (a) CdSe nanoplatelets of different size separated by average distance of 2.06 nm, forming efficient donor–acceptor pairs. (b) Time– and energy–resolved PL intensity map of a 4–ML/5–ML CdSe nanoplatelets. (c) PL decay curves at 512 nm (left) and 550 nm (right), respectively corresponding to 4–ML donor and 5–ML acceptor. The enhanced decay for the donor (4 ML) and the reduced decay (5 ML) both indicated ET from 4ML to 5 ML NPLs. (d) The increase and decrease in intensity for donor and acceptor (from the decay curves in c) as compared to the neat donor and acceptor samples. Reprinted with permission from ref. 205, copyright 2015, Macmillan Publishers Limited.

3.6.3 ET between semiconductor nanoplatelets

As discussed above, ET involving 2D materials leads to the breakdown of the R^{-6} dependence of ET rate, which have been theoretical and experimentally demonstrated in different systems built up from dyes molecules, semiconductor quantum rods and quantum wells.36,203,204 When both the donor and acceptor are structurally 2D, such as quantum well, the ET becomes completely different as compared to that of the systems consisted of 0D QDs or ions. Benefited by the advance in wet chemistry, the investigation of ET in a cofacial stacking of semiconductor nanoplatelet (NPL) of controlled thickness down to few monolayer (ML) has been made possible recently.204 For instance, in the colloidal assembly consisting of random stacking of 4 ML and 5 ML CdSe NPL, the 4ML NPLs with higher exciton energy (due to stronger quantum confinement) act as the donor, and 5ML NPLs is the acceptor in ET. The ET from the 4 ML to 5ML NPL was found to take place with efficiency up to 60%. The ET rate however cannot be further improved due to self–stacking of NPLs with the same thickness, which increase the ET distance. In a more recent report, as revealed by ultrafast spectroscopy, the inter–plate ET rate in this type of NPL assembly was around 6–23 ps^{-1} (**Fig.** 17), which is 15–50 times higher than Auger recombination.205,206 Particularly, under higher excitation densities the fast ET suppress efficiently fluorescence quenching by Auger recombination, thus enabling more efficient collection of multiple excitons by the acceptor layers. The enhanced ET rate can be rationalized by the increased contact area in the face–to–face stacking of NPLs. Precise control of stacking of NPLs are expected to further increase ET efficiency which may promise application in optoelectronic areas.

3.7 ET in Ion–complex, plasma enhanced luminescence and beyond

ET certainly do not limit to inorganic systems like phosphors and QDs; optically active complex as well as metallic plasmonic nanostructures have also served as donor or acceptor centers in ET as long as the spectral resonance condition is met.

3.7.1 ET between ion, QD and organic complex

The original studies on ET are made with organic chromphores; however, with several decades of development this field has expanded rapidly to bio–organic systems as well as inorganic systems with potential application in different areas.3,12 The discussion of ET in pure organic or bio–organic systems is beyond the scope of this review. However, as organics offer rich spectral features, in recently years the sensitization of RE or TM ions by organic chromphores or complex in fact has been widely investigated.207,208,209,210,211 Visible-light-emitting RE ions like Tb^{3+} and Eu^{3+} can be sensitized in the UV region by organic complex for the generation of visible light. Furthermore, NIR emitting ions like Yb^{3+} and Nd^{3+} can be

sensitized by different complex with absorption band located in the visible range. For instance, Yb^{3+} can be sensitized by phenylenevinylenedicarboxylate–3, which forms a metal organic framework with Yb^{3+} and enables visible light excitation of Yb^{3+}.212

Similar to the interactions that occur between QDs described above, the coupling of QDs with an organic semiconductor also occurs and the transfer of excitation energy has been observed in a number of systems.213-215 Again, in a resonant manner organic emitters (such as dye molecules) as well as organic semiconductors (such as aromatic carbon and conjugated polymers) have been employed to sensitize QDs. For instance, the CdSe/ZnS core–shell QD can be sensitized by a blue–emitting polymer semiconductor, leading to much enhanced QE under UV and blue light excitation.213,214 On the contrary, the light emission from organic semiconductor can be also sensitized by inorganic semiconductor quantum wells, which has been observed in a hybrid structure consisting ZnO quantum well and an organic [2,2–p–phenylenebis–(5–phenyloxazol)–sexithiophene] compound.215 Note that the excitons are of the Frenkel type in organic compounds and of the Mott–Wannier type in inorganic semiconductors, the electronic ET in these examples indicates the conversion of exciton type of much different level of quantum confinement.

3.7.2 Plasma enhanced luminescence

In metallic nanostructures, the collective oscillation of conduction electrons is known as localized surface plasmon resonance (SPR), featuring strong absorption peak which depends on the size and shape of the metal structures (Fig. 18).216,217 The interaction of plasmonic nanomaterials with luminescent centers also behaviours quite similarly as resonant ET because in these systems resonance condition still has to be fulfilled for the generation large enhancement in emission. Namely, the SPR band of the plasmonic materials has to be in resonance with the absorption of the luminescent centers. Metallic plasmonic nanostructures based on Au and Ag are of particular interest due to their chemical stability and spectral tunability. The localized SPR of Ag or Au nanostructures which are located in the visible have been used to enhance the PL of diverse materials, from colloidal QDs, to RE doped nanoparticles and organic or bio–organic molecules.218 This enhancement has been observed in solid materials, solutions and nanostructured devices, leading to its wide applications in bio–sensing, optoelectronics, and photonics.219

It has been generally accepted that the interaction of plasmonic nanomaterials with incident light leads to a local enhancement of the electric field, especially around sharp tips where the field enhancement reaches maximum (Fig. 18).220,221,222 This on the other hand implies that the plasmon enhancement of emission is a near field effect and it occurs only in carefully designed nanosystems where the “hot spot” of the electric field and the emitters are positioned in the correct distance and geometry with respect to each other.223 Indeed, the quenching of luminescence is often resulted for emitters in the presence of nearby Ag or Au nanoparticles due to their strong and broad visible absorption (**Fig.** 18).224 As demonstrated in a device made by Teng et al., 223 the largest enhancement of emission is observed for Au–molecule distance of 1 nm (see Fig. 18c, d). The enhancement factor drops rapidly with the increase in distance, and no enhancement or even quenching of the emission is resulted if the fluorophores is positioned at away from the optimal location.

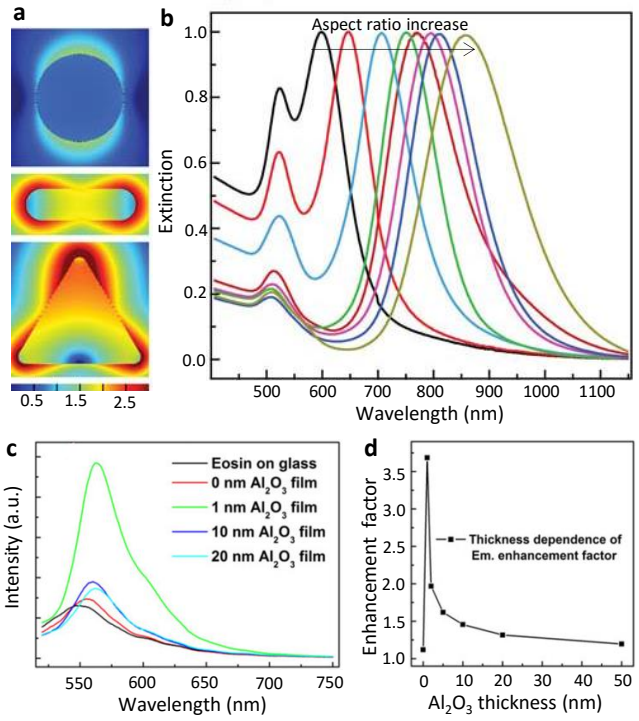

Fig. 18 Optical properties of plasmonic nanostructure and plasma enhanced luminescence. (a) Contour plot for the electric field enhancement around Au NCs of different shapes. Maximal enhancement of emission is usually produced when the particles are placed near the hot spot where the electric field intensity is maximal. (b) Extinction spectra of Au nanorods with different aspect ratios. By increase the aspect ratio the resonance band can be tuned from visible to the infrared spectral region. Reprinted with permission from ref. 224, copyright 2014, Wiley–VCH. (c) Emission spectra of Eosin Y molecules on the surface of plasmon nanostructures (Au) spaced by varying thickness of Al_2O_3. (d) Enhancement factor as a function of Al_2O_3 thickness. Reprinted with permission from ref. 223, copyright 2012, Wiley–VCH.

4. Applications of ET–related materials and processes

Since ET can be used to modulate the optical spectra of D-A pairs, it may have important implications for application in different areas ranging from phosphors to photonics. On the other hand, the high sensitivity of ET to distance and other parameters enables the application of certain materials in sensing and detection making use of optical ET.

4.1 New phosphors making use of ET

4.1.1 ET in White light emitting phosphors

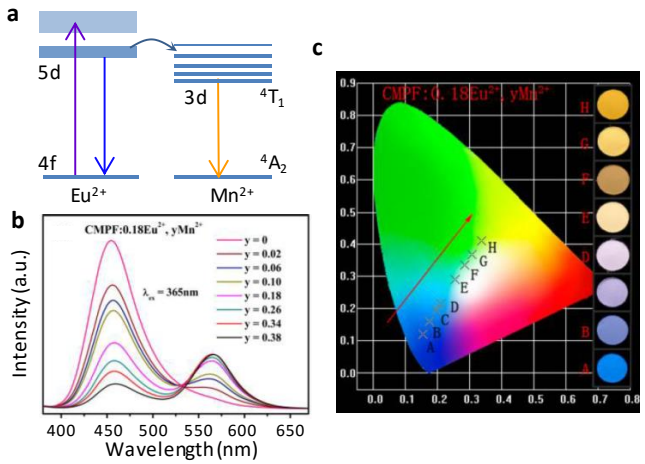

Fig. 19 ET in CMPF:Eu^{2+}, Mn^{2+} white light phosphor used for UV-LED. (a) Schematic diagram for the ET from Eu^{2+} to Mn^{2+} following UV excitation. (b) Emission spectra for the CMPF:Eu, Mn phosphor with different concentrations of Mn^{2+}. (d) Calculated CIE color coordinates for the emission spectra shown in b, and the inset shows the photographs of the corresponding phosphor under UV irradiation. (A–H are samples with y=0–0.38). Reprinted with permission from ref. 226, copyright 2014, American Chemical Society.

With the commercialization of phosphor converted white light LED, there has been growing interest in the searching of efficient yellow phosphors that can be excited by near UV or blue LED chips. Most of the conventional phosphors used in fluorescent lamps are not suitable because of high lying excitation band in the UV region.18,62 By selecting appropriate host and dopants, the ET strategy discussed above can be applied for the development of phosphors for semiconductor lighting.225 For instance, in a Eu^{2+}–Mn^{2+} codoped $Ca_9Mg(PO_4)_6F_2$ (CMPF), the spectra exhibits a clear dependence on the concentration of Mn^{2+} and Eu^{2+}, as seen from **Fig.** 19.226 By careful adjusting the concentration of the dopant ions, white light emission can be obtained after balancing the blue emission from Eu^{2+} and yellow emission from Mn^{2+}. Due to the strong excitation band in the near UV region, this phosphor could be applied in UV–based white light LEDs. A detailed analysis indicates that the ET from Eu^{2+} to Mn^{2+} can be rationalized with d–q interaction and a critical distance around 1.5 nm is found.

On the other hand, RE ions with dense f–f transition lines in the blue or near–UV region, such as Dy^{3+}, and Sm^{3+}, can also act as the sensitizer, and the combination with a red–emitting ion like Eu^{3+} can finally results in white light emission.227 Furthermore, the use of ET strategy can optimize the color temperature as well as color rendering index of commercial phosphor used for LED, such as YAG:Ce^{3+}. By admixing a red emission using ions of Pr^{3+} or Eu^{3+} that can be sensitized by Ce^{3+}, the color temperature for YAG:Ce^{3+}, Pr^{3+} (or Eu^{3+}) is significantly reduced as compared to that of YAG:Ce^{3+} due to the reddish emission from the second dopant, resulting in the desirable warm white emission.228,229

4.1.2 ET in photonic materials

As an efficient strategy to modify spectral feature, ET has played an important role in the performance of materials for photonic applications. Especially in RE activated materials, the use of sensitizer is often preferable in order to improve excitation efficiency. Yb^{3+}, for instance, due to its large absorption cross section near 1000 nm, can serves as the donor ion for NIR emitting ions, such as Tm^{3+} and Er^{3+}. In fact, RE ions with relative large absorption cross section at the working wavelength of commercial laser diode usually serve as donors in the development of laser materials (see Table S2 for examples). Beside the RE doped materials, non–RE ions also need to be sensitized, and Yb^{3+} is again proved to be efficient donor. For instance, in Ni^{2+} doped and Bi–doped glass–ceramic and glass materials, the broadband NIR is notably enhanced in the presence of Yb^{3+} when excited at 980 nm.83,84,86,87 Importantly, the sensitization by Yb^{3+} enables the optical amplification of a Bi–doped phosphate glass in the region from 1270 nm to 1350 nm, which is otherwise not possible without codoping with Yb^{3+}.86

4.2 Spectral UC and DC for enhanced light harvesting

Efficient use of solar energy by spectral conversion has been paid growing attention in recent years, because proper spectral manipulation using the above ET principles can be utilized for better solar light harvesting. Currently, the utilization of solar energy by different types of PV systems as well as artificial photosynthesis still suffer from low energy conversion efficiency due to the limited spectral response of the light harvesters used in this systems. For semiconducting light harvesting materials, photons of sub–bandgap energy, especially the NIR part of solar radiation, cannot be used to generate photocurrent; exceeding the Shockley–Queisser limit of conventional solar cells remains impossible. However, it has been proposed and experimentally demonstrated that the combination of the an UC phosphor layer with a conventional solar cell can harness part of the NIR light and therefore leads to the enhancement in conversion efficiency (**Fig.** 20a).230,231,232,233 On the other hand, photons with energy greater than $2E_g$ (E_g: band gap) only have a maximum PCE (in theory) of less than 50% in normal solar cells, where the excess energy is dissipated as heat. By splitting each of the high energy photons into two or more low energy photons, the efficiency of the solar cell with an attached DC phosphor layer is expected to be doubled in certain spectral region.114,234, It is therefore anticipated that the combination of the above strategies might be used to break the Shockley–Queisser limit in commercial solar cells (**Fig.** 20b).

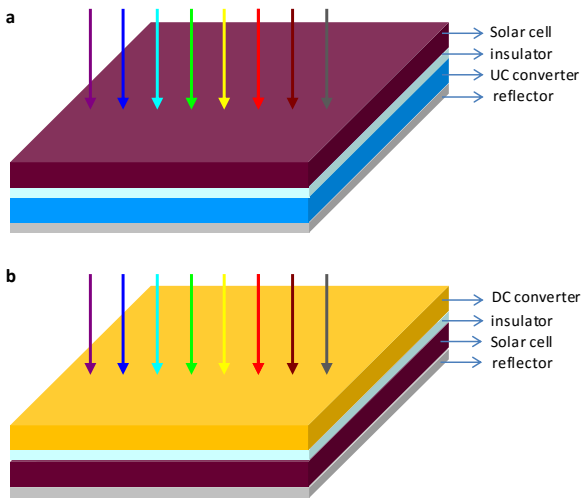

Fig. 20 Configuration of solar cells with added spectral converting layer. (a) A UC layer is attached to the rear part of the solar cells such that the transmitted NIR light is converted to visible emission and reflected back to the solar cell. (b) A DC layer is attached to the front of the solar cell such that high energy photons is cut into lower energy photons and then absorbed by the cell.

4.2.1 Utilization of NIR light in solar cells by UC

In standard solar cells, harness part of the sub–band gap photons can be possible in the presence of a spectral up–converter. Due to absorption of UC emission by the semiconductor, combination of a UC phosphor with a semiconductor of suitable band gap can result in the photon response to sub–band–gap photons in the NIR range.230-233 Up to the present, different semiconductors, such as Si, CdSe, TiO_2 and UC phosphors such as RE–doped fluorides have been used to build this type of NIR responsive heterojunctions, whose operating range depends on the absorption of the donor center in the UC phosphor.235 The first demonstration of such PV systems with incorporated UC materials was made by Güdel et al in 2005 with an amorphous Si solar cell.236 They used the $NaYF_4:Er^{3+}$ UC phosphor as the UC converter which gives visible UC emission by pumping the $^4I_{15/2}\rightarrow{}^4I_{13/2}$ transition of Er^{3+} near 1520 nm. In a proof–of–concept demonstration, a highest EQE of 2.5±0.2d% was obtained under the excitation by a laser diode at 1523 nm. This simple strategy was later extended by using more efficient co–doped UC materials. For instance, a layer of hexagonal $NaYF_4$:Er(18%), Yb(2%) particles was attached to the back of a similar amorphous Si solar cell in front of a white reflector.237 Under 980 nm excitation, the photocurrent increases by 100% as compared to the reference cell without the UC layer. The increment in photocurrent was ascribed to the UC emission from the UC layer as well as the defect absorption by localized states in amorphous silicon. Similar experiments has been demonstrated by Chen et al using 980 nm laser as the excitation light, and the enhancement in NIR response and conversion efficiency have also been observed.238,239

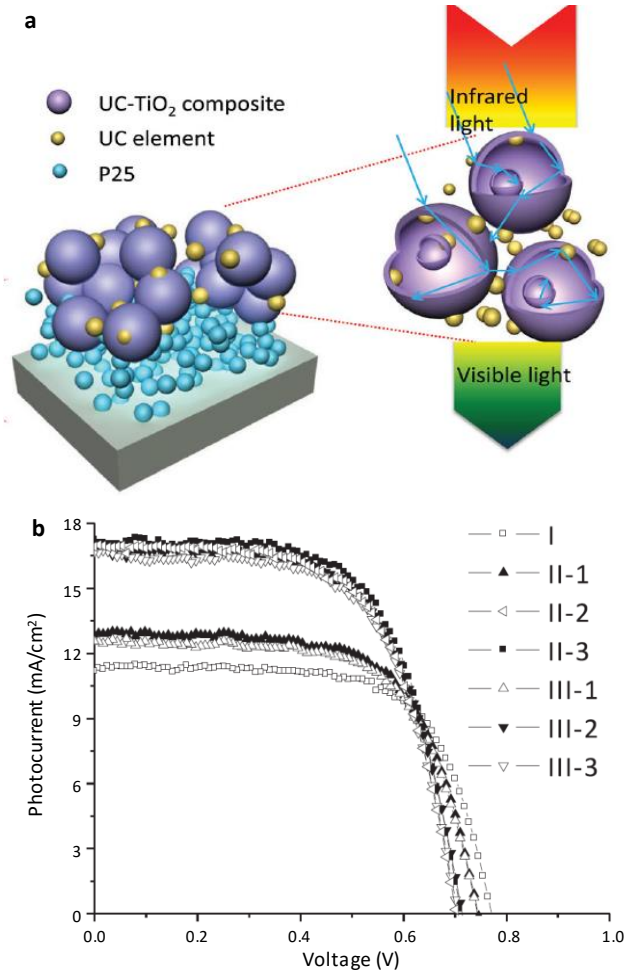

Fig. 21 UCNPs combined with a TiO_2-based dye-sensitized solar cells. (a) Schematic for the microstructure of the thin film, where TiO_2 (P25) particles are deposited in the bottom, covered by a layer of UC-TiO_2 microsphere composite. (b) Performance of the different cells. I: P25, II-1: P25+UC-TiO_2 (thickness 6 μm), II-2 and II-3: P25+UC-TiO_2 (thickness 11 μm), III-1: P25+TiO_2 (thickness 6 μm), III-2 and III-3: P25+TiO_2 (thickness 11 μm), Reprinted with permission from Ref. 240, copyright 2013, Wiley–VCH.

Similar to the Si–based solar cells, the incorporation of UC phosphor into TiO_2–based dye sensitized solar cell (DSSC) as well as polymer based cells also demonstrated enhanced NIR response.240-242 In a DSSC made by Wu et al,240 RE ions of Yb^{3+} and Er^{3+} as UC converter were "doped" into the TiO_2 hollow sphere by a sol–gel process. Under simulated solar light irradiation, the system yields a maximum QE of 9.12%, which manifest a 32.7% enhancement as compared to the bare TiO_2 (P25) anode (Fig. 21). The problem with this system is that the typical red UC emission by the transitions of Er^{3+} ($^4F_{9/2}\rightarrow{}^2I_{15/2}$) at 650 nm cannot be absorbed by the dye in the cell. This problem can be partly avoided through the use of dye molecules with absorption at longer wavelength. As shown in a similar cell,241 the Z–907 dye was adopted which has a broad absorption bands spanning from blue to red spectral region. In this cell, UCNPs of $NaYF_4$:Yb/Er with an average diameter of 7 nm was infiltrated into a porous TiO_2 film which has a pore size of around 10 nm. This design results in a photocurrent of 0.87 mA cm^{-2} under a 980 nm (2 W) laser excitation, and an overall increase in the photocurrent under simulated solar irradiation.

To further enhance the performance of the DSSC systems, the UC phosphor ($NaYF_4$:Er/Yb) was combined with plasmonic silver nanoparticles and used as the light harvesting reflector attached to the rear part of the cell.242 The results shown by Ramasamy et al demonstrated that the PCE was improved from 5.8% for the reference cell to 7.04% for the reflector modified system.

In a quite similar cell, the UC nanoparticles were introduced to different polymer based solar cells. For instance, $NaYF_4$:Yb/Er nanoparticles accessed with the solvothermal approach was again used as the NIR light harvester. The UCNPs were doped into the PCDTBT:PCBM blend layer in the polymer bulk heterojunction solar cell, leading to an 8.68% increase in short circuit current and a 19.1% increase in PCE.243 The same UC phosphor was incorporated into a P3HT/P3HT:PC61BM bilayer cell and the short circuit current and the PCE were again notably improved due to enhanced harvesting of the NIR light by the UCNPs.244

4.2.2 UC enhanced photocatalysis and artificial photosynthesis

In addition to the enhancement of PCE for PV devices as discussed above, harvesting NIR light in photocatalysis and artificial photosynthesis systems have also been helped by UC materials. There have been a number of investigations which examine the combination of UC phosphor with a typical semiconductor photocatalyst, such as TiO_2 and CdS, for the photocatalysis under NIR irradiation.245-249 There are generally two different strategies to incorporate the UC ion pairs into the different types of photocatalyst. Since most of the semiconductors cannot provide suitable lattice site for trivalent RE ions, it is natural to incorporate the RE–doped UC phosphor particle, such as fluoride, into the semiconductor photocatalyst, and the performance of such systems is usually optimized through careful engineering of the nanoscale architecture. For instance, by employing a core–shell structure in a UC–TiO_2 junction,245 Qin et al showed that the UC shell (YF_3:Yb^{3+},Tm^{3+}) converts the NIR light to visible emissions which are then absorbed by the TiO_2 core, where photoelectrons are produced. This nanostructured catalyst exhibits high activity for the degradation of methylene blue and methyl orange under NIR (> 700 nm) irradiation. In comparison, Tang et al. designed a different core–shell particle, in which the $NaYF_4$:Yb^{3+},Tm^{3+} core is coated with a shell of TiO_2 (**Fig.** 22).246 This structure showed moderate activity for photocatalytic dye degradation under NIR irradiation originated from the UC emission in UV produced by Tm^{3+}. Similar NIR active core–shell materials systems, such as ZnO/$NaYF_4$:Yb,Tm, ternary system $NaYF_4$:Yb, Tm/CdS/TiO_2, and $NaYF_4$/TiO_2 nanorod, have also been developed and their NIR activity is similar as that of the systems described above.247,248,249

The combination of a UC phosphor with semiconductors like TiO_2 and CdSe can also be used for water splitting under NIR light irradiation in a photoelectrochemical cell.250 The visible UC emission given by the RE ion pair first produces electron–hole pairs in CdS particle. The electrons at the bottom of the conduction band of CdS then diffuse to TiO_2 which serves as the ultimate water splitting catalyst. Further improvement of the performance of such structures can be achieved through the integration of plasmonic nanomaterials. As shown by Liu et al. 251 in a ZnO nanorod array coated with $NaYF_4$:Yb,Er UC nanoparticles, CdTe and Au NPs, both the photocurrent and the gas evolution rate under NIR irradiation were enhanced by over 100% compared to the samples without attached plasmonic Au NPs.

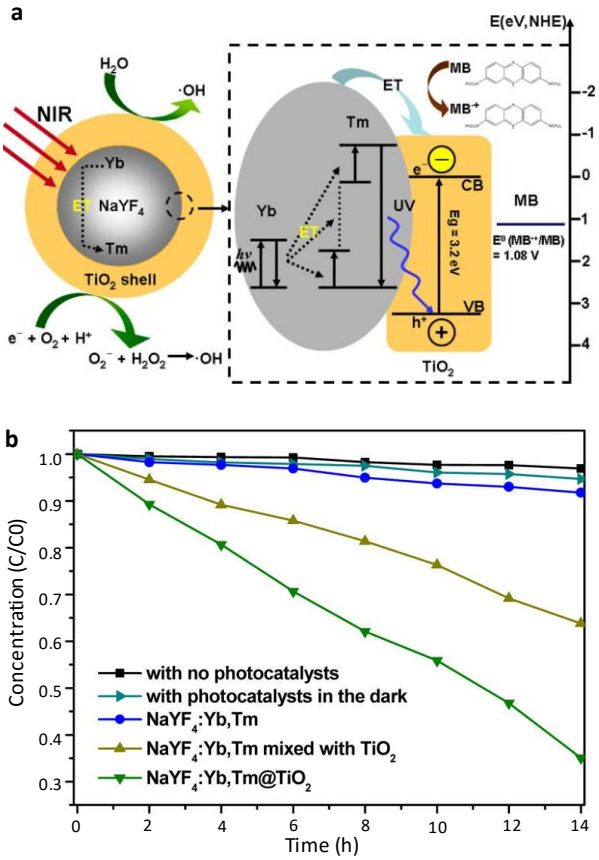

Fig. 22 $NaYF_4$:Yb,Tm/TiO_2 core–shell structure for the harness of NIR light. (a) Left: Core-shell structure for the generation of radicals (such as ·OH, $O_2^{\cdot -}$, and H_2O_2) under NIR irradiation. Right: Energy level alignment and ET mechanism for the $NaYF_4$:Yb,Tm/TiO_2 core–shell structure. (b) Comparison of the degradation rate for methane blue of different materials. Reprinted with permission from Ref. 246, copyright 2013, American Chemical Society.

Without resorting to a nanoscale architecture described above, the RE pair can be directly doped into the lattice of a semiconductor photocatalyst for NIR light harvest. Li et al demonstrated successful doping of Yb^{3+}–Tm^{3+} pair to TiO_2,252 which exhibited high activity for the degradation of Rhodamine B solution under NIR irradiation. As TiO_2 is apparently not a suitable host for RE ions because of large difference in ionic size and electronegativity between Ti^{4+} and RE^{3+}, the doping of RE^{3+} into a trivalent lattice site could be much easier. It is reported recently that Yb^{3+} and Er^{3+} can be doped to the Bi site in $BiVO_4$ using a wet–chemistry process without introducing of secondary phase. Under NIR excitation, the UV and visible emission from the Yb^{3+}–Er^{3+} pair can be partly absorbed by $BiVO_4$ to induce band transition.253 It is shown that the doped samples demonstrate much faster oxygen evolution rate as compared to the undoped ones,

which is correlated with the UC process and structural change as a result of RE doping.

4.2.3 Limitations and debates on the NIR harvesting using UC materials

Concerning the mechanisms of improved PCE and short circuit current in the solar cells, it is quite easy to accept that the upconverted photons from the NIR part of solar radiation contribute dominantly to the enhanced performance. However, it has to be noted here that the UC process is a non–linear process and the UC intensity is typically proportional to the n–th power of the excitation density for an n–photon UC process. This is why monochromatic laser has to be used as the excitation source to generate UC emission for the RE activated systems, rather than non–coherent light sources such as Xe–lamp and natural light. Typically, the EQE of UC emission based on the ET mechanism is far smaller than 10% regardless of the types of ion pair and host. Under simulated sunlight irradiation, the UC emission efficiency could be too low in many of the described system to produce notable enhancement in PV devices. Indeed, the UC emission under solar light pumping has rarely been reported in different UC phosphors. This fact may suggest that the contribution of the upconverted photons to the overall PCE could be negligibly small. On the other hand, the f–f transitions of RE ions by nature are parity forbidden and this fact strongly restricts the absorption band width. This becomes a critical problem for application as the absorption of the RE ions, like Yb^{3+} and Er^{3+}, only covers a very limited region of solar spectrum in the NIR region (centered around 1000 nm for Yb^{3+}). Combined with the low UC emission efficiency in practical conditions, large increase of PCE for these solar cells by the UC process seems to be an unrealistic goal. In fact, more and more evidence point to the fact that it is the scattering effect of the UCNPs that contribute to the enhanced performance and this effect can be dominating as reported recently in a polymer solar cell.254

4.2.4 QC materials for solar cells

In comparison to the UC materials that have been extensively used in PV devices as well as artificial photosynthesis, different RE–doped inorganic DC phosphors are still far from application for enhancing the efficiency of practical PV cells, albeit claimed QE of near 200%.114 This is related with the fact that the EQE for the different types of RE activated QC materials has never exceeds 30%, as we have discussed in section 3. In comparison, QDs and certain organic compounds that experience multiple exciton generation upon excitation have shown great promise as light harvesters in solar cells.255 According to the calculations made by Nozik et al.,256 the maximum PCE increases from 33.7% to 45% for a single band QD-based PV device under AM 1.5G illumination. The efficiency can be increased further when QDs CM absorbers are used in two gap tandem devices.

Experimental demonstrations of PV devices making use of CM or SF for enhanced efficiencies have been reported recently.180, 257-262 Lead based QDs like PbCh (Ch=S, Se) with efficient CM have been used as absorbers in different PV systems.257 By combining PbS with TiO_2, for instance, the IPCE (incident photon–to–current efficiency) and APCE (absorbed PCE) of this QD–sensitized solar cell can reach as high as 0.7% and 190% at photon energy around 3.0 eV, respectively.258 Due to a favorable band alignment between TiO_2 and PbS QDs, the extraction of photoelectrons in QDs by TiO_2 is more efficient as compared to recombination. For photon energy higher than the threshold energy of multiple exciton generation (around 2.5–3.2 E_g), both IPCE and APCE increase notably due to the generation of more than one electron per photon absorbed. The first solar cell with EQE greater than 100% was a QD–based PV device made by Semonin et al.,259 as shown in Fig. 23. For this device the EQE (defined as the ratio of collected charge carriers to incident photons) exceeds 100% at photon energies between 3–3.5E_g and the maximum value reaches 114±1%. After corrected for reflection and absorption loss, the maximum IQE is 130%.

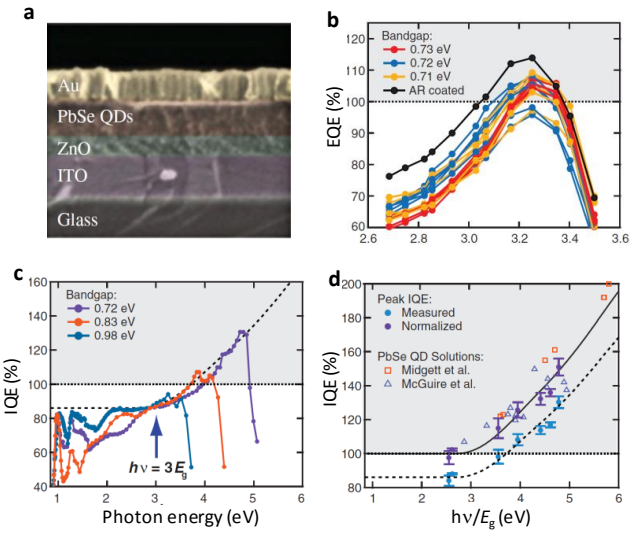

Fig. 23 PbSe QD solar cell with EQE greater than 100%. (a) Cross section (false color) of the device. (b) EQE as a function of photon energy for 18 independent devices made from QDs of different sizes. (c) Calculated IQE (corrected for absorption and reflection loss) as a function of normalized photon energy for QDs with three different E_g values. (d) Measured peak IQE values for QDs with seven different sizes, and the IQEs normalized to 100% QY for incident photons. The QE value of the QDs obtained by transient absorption measurements are shown as triangles and squares. Reprinted with permission from ref. 259, copyright 2011, American Association for the Advancement of Science.

Solar cells based on organic semiconductors that undergo SF have also been exploited intensively for enhancing the conversion efficiency.180,260,261 To build a solar cell utilizing SF, one has to find proper acceptors with right band alignment such that the photon generated triplet excitons can be extracted efficiently. A summary of energy alignment of the acceptors for the extraction of triplet exciton and can be found in ref.180. Small organic molecules as well as colloidal QDs are effective acceptors and a dozen of such devices have been realized.180,261 In a hybrid cell made of fullerene and pentacene (**Fig.** 24),260 the triplet excitons are efficiently extracted by fullerene, leading to a peak EQE of (109±1)% at 670 nm and an IQE of (160±10)%. Similarly, the combination of

pentacene with PbS by a solution process yields an overall PCE of 4.8%, an EQE of 60% and an IQE of 170%.262 Especially, both EQE and IQE reach maximum values at around 600 nm where strongest absorption peak of pentacene is located, suggesting SF indeed facilitates the improvement in PCE. In spite of low PCE values, this type of cells are expected to be improved in the future driven by optimization of the device structure.

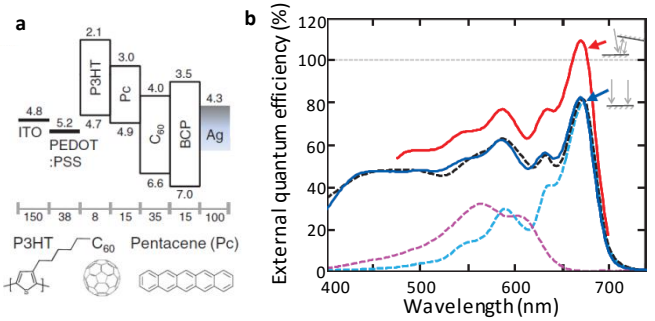

Fig. 24 Device structure and EQE of SF solar cell based on pentacene. (a) Architecture of the cell and the positions of the lowest unoccupied and highest occupied energy levels (in eV) of the molecules. Indium tin oxide (ITO) and poly(3,4–ethylenedioxythiophene) poly(styrenesulfonate) (PEDOT:PSS) serve as the anode, and bathocuproine (BCP) with silver coating is used as the cathode. The chemical structures of the molecules are shown in the bottom. (b) EQE of devices without optical trapping (blue line), and device measured with light incident at 10° from normal with an external mirror reflecting the residual pump light (red line). The dashed lines are fitting results of QE for pentacene (blue), P3HT (purple) and the devices (black). Reprinted with permission from Ref. 260, copyright 2013, American Association for the Advancement of Science.

4.3 Luminescent labels for advanced bio–applications

Due to their rich and robust f–f transitions, RE activated nanophosphors exhibits significant advantages compared to conventional chromphores such as organic dye molecules and colloidal QDs. In addition, through the careful selection of the RE ion pair, the spectra of the materials can be finely engineered to produced down-shifted and UC emissions at desired spectral range. Particularly, these RE–activated nanophosphors open a new gate for bioimaging based on anti–Stocks emission with NIR excitation, which has large penetration depth and can efficiently avoid auto-fluorescence of biological tissues.

4.3.1 Advances in UCNPs for bioimging and sensing

As the accessibility of UCNPs becomes easier in the recent decades due to the rapid advances in wet–chemistry synthesis, bio–labelling using UCNPs emerges as an advanced technique in optical imaging.263-265 After proper surface modification, inorganic UC nanoparticles doped with ion pairs such as Yb^{3+}–RE^{3+} (RE: Er, Tm) have been extensively used for in–vivo detection and visualization of diverse animal cells and bio–tissues. Especially, under the UC mode the background fluorescence, which strongly reduces signal/noise ratio in fluorescence microscopy, can be effectively avoided.263 This field has been expanding rapidly and discussed in a number of excellent reviews published in recent years.264,265

With the application of new ET strategy, materials with anti-Stocks emission operational at new spectral region are continuingly developed, which offer certain advantageous over the well-known UC materials activated with ion pairs of Yb^{3+}-RE^{3+} (RE:Er, Tm). As we know, Yb^{3+} ions has to be pumped near 1000 nm, where biological substance absorbs strongly due to the presence of water, leading to considerable thermal effect.266 Therefore, the use of a new ion pair in which enables excitation at a shorter wavelength is much desirable. Wang et al reported recently that Nd^{3+} ion is able to effectively transfer the excitation energy to Yb^{3+} by pumping its $^4F_{5/2}$ at 808 nm.267 In a $NaGdF_4$:Yb,Er@$NaGdF_4$:Nd,Yb core-shell structure, the Nd^{3+} and Yb^{3+} in the shell ultimately transfer the excitation energy to Er^{3+} ions in the core, giving bright visible emission by the transitions of Er^{3+} (**Fig. 25**). Using the core-shell particles as the probe, the heating effect can be minimized as compared to pumping Yb^{3+} ions at 980 nm. In a similar core-shell particle of $NaGdF_4$:Yb,Tm@$NaGdF_4$:Nd, both anti-Stocks and Stocks emission at the NIR window for biological tissues can be produced by pumping at 980 nm and 785 nm, respectively. This system demonstrated by Zhou et al shows high luminescence efficiency and enables dual-mode visualization of biological tissues in the NIR range by both Stocks and anti-Stocks emission.268

In addition to the UC in RE doped systems, anti–Stocks process based on photon–stimulated emission can also serves as a luminescence probe in biological tissues. Unlike the UC from RE ions, the photon–stimulated process mechanistically is a one–photon process and it can be excited by incoherent NIR light at very low intensities. Therefore, the NIR photons actually servers as a trigger which release the electrons stored in an intermediate levels produced by previous high energy excitation.269,270 The released electrons can then transfer its energy to the activators to give the luminescence. In a Cr^{3+} activated oxide phosphor developed by Qiu et al.,271 after saturated charging with a UV lamp for 5 min, the red emission centered at 710 nm from Cr^{3+} can be triggered by NIR light excitation from 780 nm to near 1000 nm. In addition, the emission of Cr^{3+} showed sufficient lifetime and good reversibility for imaging of biological tissues. This type of NIR luminescent labels might be of special interest as the excitation light is orders of magnitude weaker than normal UC labels.

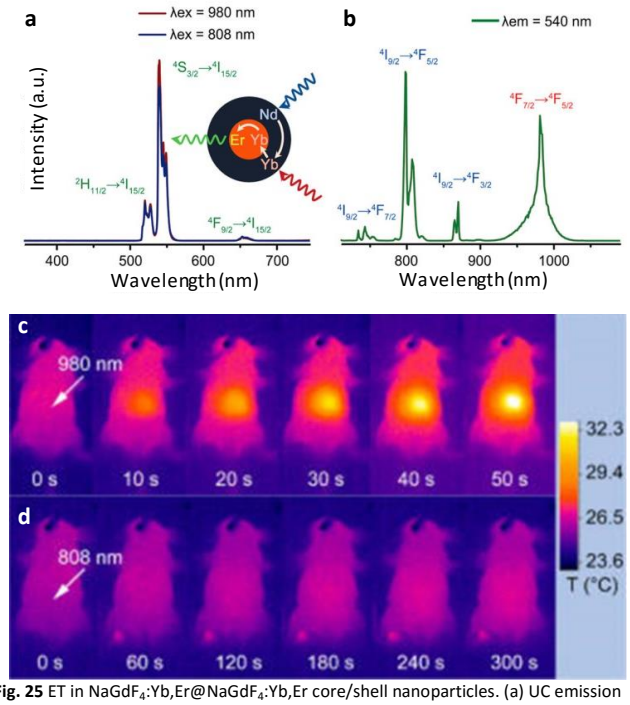

Fig. 25 ET in $NaGdF_4$:Yb,Er@$NaGdF_4$:Yb,Er core/shell nanoparticles. (a) UC emission spectra under excitation at 808 nm and 980 nm. Inset: ET form Nd^{3+} to Yb^{3+} doped in the shell finally leads to the UC emission of Er^{3+} doped in the core. (b) Excitation spectrum monitoring the emission at 540 nm. (c, d) Photographs taken by an infrared camera for a nude mouse under continuous irradiation by NIR lasers of (c) 980 nm, and (d) 808 nm. The increase in temperature in the laser irradiated area is notable in c. Reprinted with permission from ref. 267, copyright 2013, American Chemical Society.

4.3.2 FRET imaging and detection

One of the essential characters of FERT is its rate is depends on the inverse sixth power of the separation between the donor and acceptor center. Therefore, FRET signal is extremely sensitive to the slight change in position when the donor and acceptor are separated by a distance comparable to the Förster distance (usually 3 – 6 nm), which match the size of most biological macromolecules, such as proteins. FRET and the associated imaging technique therefore have been widely applied for the in vivo or in vitro examination of diverse biological processes which produce conformational change.272,273 In the FRET technique, a pair of D–A is employed as emissive probes to label the molecule or biological system. The change in emission intensity of the acceptor can be used as the reference for the change in D–A separation, which can be connected with, for instance, conformational change of the labelled biomolecules and change in biological conditions.273,275,276 This technique offers high spatial and temporal resolution and sensitivity for the investigation of molecular interactions in living cells and a variety of biological process. One of the well–known experiments is the measurement of intercellular Ca^{2+} concentration reported by Tsien et al in the 1990s.277 Cyan and yellow fluorescence proteins were employed as D-A pair respectively to label calmodulin and its binding peptide (M13–YFP). High Ca^{2+} levels lead to binding of donor with acceptor therefore stronger acceptor yellow emission, and at low Ca^{2+} levels lead to cyan emission from the donor.

In recent years, the integration of FRET into laser confocal microscopy and multi–photon imaging techniques has led to enormous technical advance as compared to the conventional wide–field FRET microscopy.278,279 In addition to the intensity based imaging technique which is usually vulnerable to the change in other conditions like concentration, recent technical advance has enabled the imaging using lifetime of the fluorophore which is directly connected with the FRET rate. 280,281 The emission lifetime of the donor would be rapidly reduced as it approaches the acceptor. When combined with FRET, the technique offers remarkable advantage for the visualization of dynamic process in cells and biological substance.

4.3.3 FRET based detection and lifetime-gated techniques using RE–doped nanomaterials

Compared with fluorescent proteins and dye molecules, RE ions offer additional advantages due to its distinct line-shaped emission and long lifetime. Therefore, RE ions doped inorganic NCs appear to be ideal candidate probes due to their chemical robustness and strong and stable emission. Therefore, they can serve as both donor and acceptor in the FRET detection and imaging. For instance, CaF_2:Ce^{3+},Tb^{3+} NCs of 5 nm in size has been used for the FRET detection of Avidin based on the ET from Tb^{3+} to avidin, and a LOD (limit of detection) of 48 PM is reported.282 In recent years, RE activated nanophosphors giving both Stocks and anti–Stocks emissions have been exploited for the detection of trace amount of chemical or biomolecules, like glucose.283Besides these molecules, plasmonic nanomaterials such as Ag, Au NPs have also been used as efficient absorbers for the visible emission from UCNPs in FRET bio–assays.284,285

Due to the presence of ET, the emission intensity from the donor will decay differently in the proximity of an acceptor. The time resolved PL spectroscopy together with time–gated techniques can be powerful tools for the detection of biomolecules. As shown by Chen et al, 286 the use of time–gated PL spectra can completely eliminate the short–lived fluorescence from background (usually in the order of nanoseconds), while the emission of RE ions with lifetime of the order of 0.1–10 ms is preserved, thus giving very high signal to noise ratio.286 In their experiment, the $NaYF_4$:Ce,Tb nanoparticles was used as the probe to detect Avidin grafted with fluorescein isothiocyanate. The ET from the donor ($NaYF_4$:Ce,Tb) to the acceptor leads to the quenching of the green emission from Tb^{3+}. With the use of time–resolved spectra and decay curves, a monotonous decrease of donor lifetime was observed with the increase of avidin concentration. Thus, the lifetime values can be used to quantify the concentration of the detected molecules and the detection limit down to 5 nM was achieved.

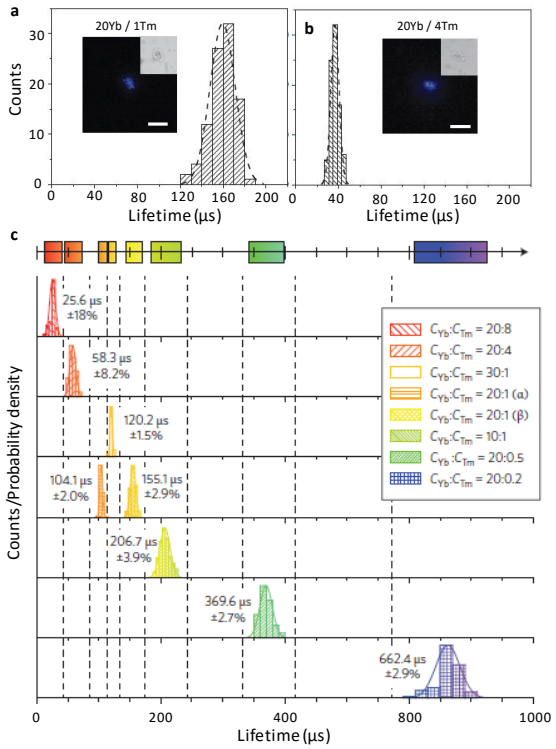

Fig. 26 Lifetime gated image using $NaYF_4$:Yb,Tm nanoparticles as imaging agent. (a) and (b) Lifetime histograms of the $NaYF_4$:Yb,Tm nanoparticle with different doping concentration of Tm^{3+}: (a) Yb:Tm(mol%:mol%) = 20:1, and (b) Yb:Tm(mol%:mol%) = 20:4. The insets in (a) and (b) are the bright–field imaging of the Giardia cysts labeled with the nanoparticles by excitation at 980 nm. (c) Lifetime histograms of $NaYF_4$:Yb,Tm with different doping concentration of Yb^{3+} and Tm^{3+}. Due to the increased ET rate, the lifetime for the blue emission from Tm^{3+} is notably reduced with the increase in the concentration of the dopants. Reprinted with permission from Ref. 287, copyright 2014, Macmillan Publishers.

The lifetime–gated technique can be further extended to distinguish particles and to separate emission bands of with different lifetimes. It is known that the decay rate of emission depends on the separation between donor and acceptor and therefore on the concentration of the activator. The lifetime is shortened at high doping concentration because the ET between nearby centers becomes easier. In $NaYF_4$:Yb,Tm, for instance, the emission lifetime of Tm^{3+} varies between 25 μs to 660 μs depending on the concentration of Tm^{3+} and Yb^{3+} (**Fig.** 26).287 Using time gated spectroscopy, the image of the luminescent nanoprobes with different lifetimes can be recorded separately (**Fig.** 26). Short–lived emission can be screened off depending on the time gap between stoppage of excitation and spectral collection. Therefore, the lifetime of RE ions as modulated by ET can provide another degree of freedom which may have significant implications for optical data storage, coding and bioimaging.

4.4 Optical sensing and detection beyond biology

The emissions of any type of optical centers and ET between different centers couple strongly with the surrounding environment, including both chemical and physical conditions. This is mechanistically related with the fact that the decay of rate of the emission center contains the contribution of intrinsic decay and extrinsic decay. The latter is always affected by the temperature and the presence of different traps that serve as acceptors. Therefore the characteristics of emission center, such as spectral shape, lifetime, and intensity can be used for sensing environmental conditions in a quantitative manner.

4.4.1 Temperature sensor

The emission intensity of a single optical center is known to be affected by the environment temperature as the rate of phonon–assisted processes is enhanced at higher temperatures where phonon population number is much larger. This mechanism can in principle leads to both increase and decrease of emission intensity with the increment of temperature depending on the types of emission process. According to the energy-gap low (see section 2), the rate of phonon–assisted ET bears strong temperature dependence, leading to the high sensitivity of emission intensity to temperatures. Up to the present, different luminescent materials have been employed as temperature sensors, especially nanoscale phosphors.288,289,290

There are basically two different types of optical temperature sensors, which respectively based on temperature dependence of the emission intensity and the ratio of emission intensity from different peaks. The intensity–based sensor (or emission position/energy based) requires the calibration for each system and it is usually vulnerable to the change of solution, concentration and other factors.291,292 These problems are circumvented in the ratio–based sensor based on intensity ratio of two emission peaks, as the intensity ratio is independent of the examined systems and the concentration.293 This is why the ratiometric sensor is always considered as calibration–free sensor. Theoretically, the intensity ratio R of two different transition peaks from the same center has the following temperature dependence.294

$$\mathrm{R} \propto e^{-\frac{\Delta E}{k_B T}} \quad (17)$$

where ΔE is energy difference between the two energy levels, and k_B is the Boltzmann constant. The sensitivity to temperature can be expressed as: 295

$$\mathrm{S} = \frac{dR}{dT} \propto R \cdot \frac{\Delta E}{k_B T^2} \quad (18)$$

In practical system containing multiple dopants the relation is not always obeyed due to the complicated interactions involved. This eq. can nevertheless provide a semi-quantitative description of the temperature-dependant emission for most systems.

The ratiometric sensing strategy has been developed based on different luminescent materials, including organic chromophores, semiconductors and ion–activated systems. For instance, in a Mn–doped $Zn_{1-x}Mn_xSe$/ZnS/CdS/ZnS core–multi–shell nanoparticle system,296 the ratio of excitonic emission intensity to that of total emission intensity was used as the temperature reference (**Fig.** 27). In this system the emission of Mn^{2+} is host–sensitized, or in other words sensitized by excitons. At room temperature the orange emission from $^4T_1$ level of Mn^{2+} is dominating under UV excitation. With the increase of temperature this emission is

gradually quenched, accompanied by the steady growth of excitonic emission peaks from the CdS shell. This process is explained by the thermally activated energy back transfer from Mn^{2+} to CdS, which result in the feeding of the conduction band of CdS, yield excitonic emission (**Fig.** 27). The energy level alignment of this nanostructure is different from that of ZnS:Mn, in which backwards ET is not possible due to large energy gap between Mn^{2+}:$^4T_1$ and bottom of conduction band of ZnS. With sufficient temperature response at temperatures from room temperature to near 300 °C, these dual–emitting nanostructures can be used as highly sensitive optical thermal probes in nanoscale environment for biological systems.

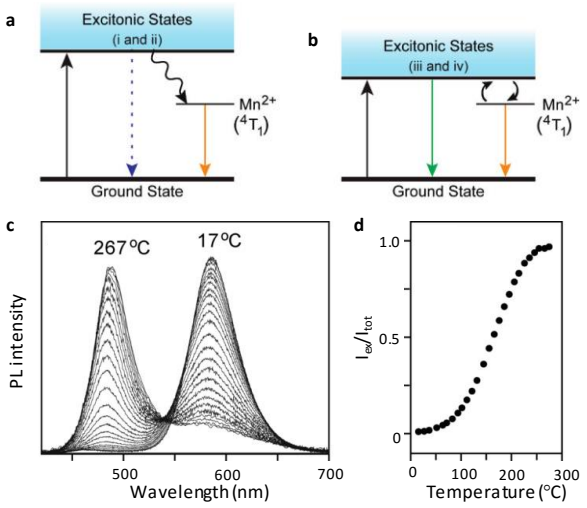

Fig. 27 Ratiometric nano–thermometer based on exciton–Mn^{2+} ET. (A) Energy level diagram and emission process of Mn^{2+} doped in a wide band–gap host, such as ZnS, and ZnSe. (B) Energy level diagram of Mn^{2+} in a semiconductor with a smaller band–gap, in which energy back transfer from Mn^{2+} ($^4T_1$) to CdS occurs by thermal excitation, producing excitonic emission in addition to the orange emission of Mn^{2+}. (c) PL spectra recorded at different temperatures of the core–multi shell Zn_{1-x}MnxSe/ZnS/CdS/ZnS NCs. (d) Temperature dependence of the ratio of excitonic emission to the total emission intensity (I_{ex}/ I_{tot}) for these NCs. Reprinted with permission from Ref. 296, copyright 2014, America Chemical Society.

The ET between RE ions is also sensitive to the thermal environment, leading to the temperature–dependent spectral character. For instance, Qian et al developed a Eu^{3+}–Tb^{3+} codoped metal organic framework (MOF) which can be used as a similar ratiometric temperature sensor based on the emission of Eu^{3+} ($^5D_0 \rightarrow {}^7F_2$) and Tb^{3+} ($^5D_4 \rightarrow {}^7F_2$).297,298 This system shows a similar spectral evolution with temperature as that of Mn–doped core–shell nanoparticle described above. With the rise of temperature, the greenish emission from Tb^{3+} is quenched, while the reddish emission of Eu^{3+} is enhanced gradually as a result of ET between Tb^{3+} and Eu^{3+}. The ratio of emission intensity of Tb^{3+} to that of Eu^{3+} therefore exhibits a clear correlation with temperature. More importantly, in this system the dependence of ratio R on temperature shows good linearity in the temperature range from room temperature to 200 K.

This strategy was later applied to nanoparticles with a core–shell structure. In the nanothermometer reported by Zheng et al., 299 the core is doped with Eu^{3+} and Tb^{3+} and the shell is doped with Yb^{3+} and Tm^{3+} in the host $NaYF_4$(**Fig.** 28). Under 980 nm laser excitation, Tm^{3+} is pumped to a high level $^1I_6$, the Gd^{3+} ions act as the energy relay which afterwards transfer energy to Eu^{3+} and Tb^{3+} in the shell, eventually leading to the visible emission from them. The dependence of I_{Tb}/I_{Eu} (intensity ratio) on the temperature exhibits good linearity in the range of 50 K –300 K. Despite the temperature dependence above room temperature is not measured in this report, this system enables temperature sensing using NIR light at 980 nm as the probe light, which is preferable for bioimaging due to large penetration depth in tissues. Thus, these nanoprobes can be used to monitor the temperature distribution inside biological tissues in a three–dimensional fashion.

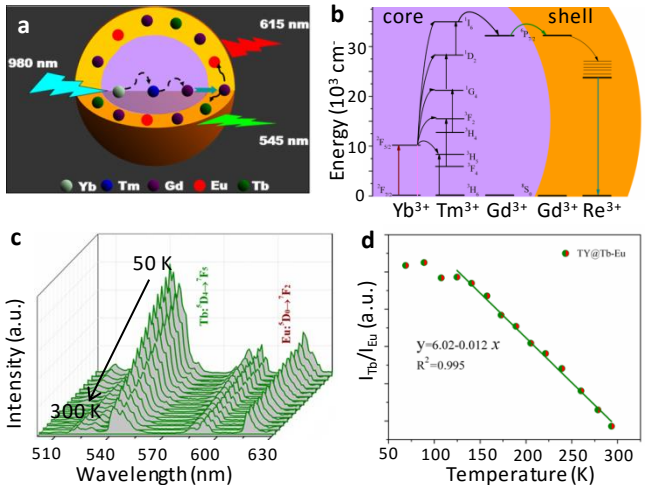

Fig. 28 Temperature sensing using RE–doped core–shell NPs. (a) Structure of the core–shell NPs in which Yb^{3+} and Tm^{3+} are doped in the core, Eu^{3+} and Tb^{3+} is doped in the shell, and the host is $NaGdF_4$ for both core and shell. (b) Energy levels and ET mechanism in the core–shell NPs. (c) Emission spectra recorded at temperatures from 50 K to 300 K under excitation by 980 nm laser. (d) Temperature dependence of intensity ratio of the Tb^{3+} emission to the Eu^{3+} emission (I_{Tb}/I_{Eu}). Reprinted with permission from ref. 299, copyright 2014, Royal Society of Chemistry.

4.4.2 Chemical sensor for gas, pH and heavy metal ion

The PL involving ET from the donor to acceptor is also affected by various external chemical stimuli, in both of the gaseous and liquid phase. Optical chemical sensors, such as pH indicator, have been widely used as the change of visible absorption can be easily observed by naked eyes. Wolfbeis et al demonstrated an ammonia sensor based on the UC emission of $NaYF_4$:Yb,Er, which is immobilized into a thin film of polymer matrix together with phenol red that servers as the pH probe.300 Upon exposure to gaseous ammonia, the emission of Er^{3+} in the green region is quenched by the phenol red triggered by the change in pH. In comparison the red emission is preserved and therefore its intensity can be used as the reference for ammonia concentration. The film meanwhile shows high sensitivity to pH due to the use of the pH probe. pH sensors based on the same mechanism have also been developed by using other pH probe molecules, such as neutral Red.301

Similarly, the combination of probe molecules that respond to a specific type of chemical stimuli can extend

sensing application of UCNPs to different chemical environments. Detection of oxygen in liquid phase is demonstrated using the combination of $NaYF_4$:Yb,Tm with an Ir–complex oxygen probe, $[Ir(CS)_2(acac)]$.302 The UC emission of Tm^{3+} near 470 nm can be used to pump the oxygen probe (Ir–complex) which gives green–yellow emission with a peak near 570 nm. By incorporating them into a thin layer of ethyl cellulose (EC), an oxygen sensor is realized using a 980 nm laser as the excitation. Upon exposure to a mixture of argon/oxygen, the emission of the oxygen probe is quenched notably, whereas the UC emission from Tm^{3+} is not affected (**Fig.** 29b). By using the emission intensity ratio of Ir–complex to Tm^{3+}, the hybrid shows high sensitivity for oxygen with high signal to noise ratio.

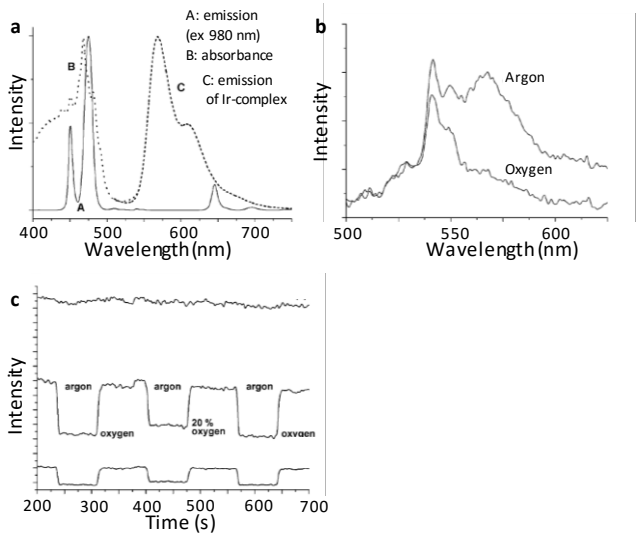

Fig. 29 Optical oxygen sensing by a $NaYF_4$:Yb,Tm–$[Ir(CS)_2(acac)]$ hybrid. (a) Normalized absorption and emission spectra of the $NaYF_4$:Yb,Tm and the oxygen probe $[Ir(CS)_2(acac)]$ (Ir–complex). (b) Emission spectrum of the oxygen sensor in an ethyl cellulose matrix after exposing to argon or oxygen (excitation: 980 nm). The emission from the Ir–complex drops notably in the presence of oxygen. (c) Time evolution of emission intensity recorded by exposing repeatedly to oxygen (O_2/N_2=2/8) and argon. Top: Ir–complex by excitation at 475 nm (collected at 696 nm); Middle: $NaYF_4$:Yb,Tm–$[Ir(CS)_2(acac)]$ hybrid by excitation at 980 nm (collected at 568 nm); Bottom: Time evolution of the ratio of the two signals (I_{568}/I_{696}) for the oxygen sensor, indicating high signal/noise ratio. Reprinted with permission from Ref. 302, copyright 2011, Wiley–VCH.

The detection and sensing of heavy metal ions in liquid phase have recently been paid with much attention partly due to increased concern about the spread of heavy metal pollution in water resources. Optical sensing of heavy metal ions have been realized in different systems contained UCNPs and organic complex. For instance, a ruthenium complex–assembled UCNPs was employed as a ratiometric luminescent sensor for Hg^{2+} in living cells, yielding a Hg^{2+} detection limit down to 1.95 ppb.303 These nanoscale luminescent probes also allows for the visualization of the intracellular distribution of Hg^{2+} ions. The detection of Hg^{2+} can be also achieved by the use of organic complex that selectively bond to Hg^{2+} and meanwhile interacts with UCNPs. As shown by Zhang et al.,304 the green UC emission of $NaYF_4$:Yb, Er can be efficiently absorbed by the Rhodamine B hydrazide complexed with Hg^{2+} that covalently bonded to the surface of $NaYF_4$/silica particle, resulting in high sensitivity and selectivity for Hg^{2+} ions.

4.4.3 Stress sensor

Emissions from solid phosphors are also sensitive to the applied stress which causes distortion of the local coordination; therefore this mechanism allows for the optical sensing of pressure applied to the materials. Optical pressure sensing has been used for decades. A well-known example is the use of ruby crystals for monitoring the pressure inside diamond anvil cells based on the emission of Cr^{3+}.305 The mechano–optical effect can be more remarkable for piezoelectric materials due to the induced electric field. In a host sensitized system of Mn^{2+} doped CaZnSO, the reddish emission of Mn^{2+} by the transition of $^4T_1(4G) \rightarrow {}^6A_1(6S)$ can sense different types of mechanical stress at a wide range of frequencies and energies.306 This is explained by the trapped carrier excitation induced by the piezoelectric effect that interferes with the exciton–Mn^{2+} ET.

The detection of pressure can be achieved in a quite different method. It is know that a group of emitters when stay within a critical distance are prone to concentration quenching that is analogous to aggregate induced quenching for organic molecules. By applying a stress the separations between emitters are reduced, leading to the enhanced interaction among nearby emitters and the reduction in the emission intensity. This type of sensor is realized in a porous composite made from nanofiber with incorporated CdSe–CdS tetrapod QDs prepared by electrospinning.307 The emission of QDs is gradually quenched as a result of increased applied stress. Furthermore, the sensing ability is enhanced with QD concentration in the composite and it can be fully recovered after repeated loading and unloading.

5. Summary and outlook

We have discussed the transfer of energy in solid state materials as well as their nanoscale counterparts mediated by photons, with focus on the optical energy transfer by means of resonance between optical centers. This type of resonant energy transfer has been named after Förster–Dexter, who, using quantum chemical method, laid the theoretical basis that is still widely applied today. In practical systems, energy transfer typically involves two optical centers acting as donor and acceptor, which can be metal ions centers, host lattice, quantum dots and organic chromophores. These systems produce downconversion and upconversion besides the normal emission in which energy transfer plays a pivotal role. In the context of energy transfer, we have discussed the similarities as well as differences of downconversion, upconversion involving metal ion dopants and multiple exciton generation in quantum dots and molecules.

For luminescent materials, careful engineering of photoluminescence spectra with energy transfer between optical centers enables the applications of these optical materials in diverse fields. Of particular interest are the large number of upconversion and downconversion materials,

especially their nanoscale counterparts, which have been intensively exploited for the development of novel luminescent materials and energy conversion devices for efficiency solar light harvesting. In the medical field, optical techniques based on energy transfer are extensively used for imaging, diagnosis, detection of biomolecules and medical treatment. Beside biomedical application, energy transfer has also played an important role in the fluorescence sensing and detection of various physical and chemical environmental conditions by optical spectra, such as temperature, stress and pollutant species.

In spite of enormous progress regarding the basic physics of energy transfer in the past century, the rapid advance of nanoscience as well as biotechnology in the 21st century has evoked increasing number of investigations into the applications of new optical materials as well as the new physics of energy transfer down to the nanoscale. Especially, the combination of optical energy transfer with the forefront of solar energy, and biological sciences remains at its infantry. On the other hand, the investigation of energy transfer between ions and other centers in a single particle level, rather than ensemble level, are still expected to delineate new physics of energy transfer in solid materials. Moreover, the development of single photon detection and the related devices made it possible to examine single ion spectroscopy.308,309 Application of these cutting–edge techniques is expected to provide deeper physical insight into optical energy transfer down to the ion–ion level.

Acknowledgements

One of the authors (X. L.) is grateful to the financial support from the Fundamental Research Funds for the Central Universities (No. 2014QNA4006) and the Natural science foundation of Zhejiang Province (No. LQ14E020003).

Notes and references

1 J. Marshall, *Nature*, 2014, **510**, 22–24.
2 G. D. Scholes, G. R. Fleming, A. Olaya–Castro and R. van Grondelle, *Nature Chem.*, 2011, **3**, 763–774.
3 G. S. Engel, T. R. Calhoun, E. L. Read, T. K. Ahn, T. Mancal, Y. C. Cheng, R. E. Blankenship and G. R. Fleming, *Nature*, 2007, **466**, 782–786.
4 C. Ronda. Luminescence: From theory to applications, Wiley-VCH, Weinheim, 2008.
5 H. Dong, L. D. Sun and C. H. Yan, *Chem. Soc. Rev.*, 2015, **44**, 1608-1634.
6 G. K. Liu, *Chem. Soc. Rev.*, 2015, **44**, 1635-1652.
7 L. P. Tu, X. M. Liu, F. Wu and H. Zhang, *Chem. Soc. Rev.*, 2015, **44**, 1331-1345.
8 P. R. Shelvin, *Nat. Struct. Biol.*, 2000, **7**, 730-734.
9 G. D. Scholes, T. Mirkovic, D. B. Turner, F. Fassiolia and A. Buchleitner, *Energy Environ Sci.*, 2012, **5**, 9374–9393.
10 R. Vangrondelle, J. P. Dekker, T. Gillbro and V. Sundstrom, Biochimica Et Biophysica Acta–Bioenergetics, 1994, **1187**, 1–65.
11 B. Gobets, and R. van Grondelle, *Biochimica Et Biophysica Acta–Bioenergetics*, 2001, **1507**, 80–99.
12 A. Olaya–Castro and G. D. Scholes, *Int. Rev. Phys. Chem.*, 2011, **30**, 49–77.
13 V. M. Agranovich and M. D. Galanin, Electronic Excitation energy transfer in Condensed Matter, North–Holland Publishing Company, 1982.
14 G. D. Scholes and G. Rumbles, *Nat. Mater.*, 2006, **5**, 683–696.
15 B. D. Bartolo and X. S. Chen, Advances in Energy Transfer Processes, World Scientific, Singapore, 1999.
16 K. T. Wong and D. M Bassani, *NPG Asia Mater*, 2014, **6**, e116/1–10.
17 D. L. Andrew and Andrey A. Demidov, Resonance Energy Transfer, Wiley, 1999.
18 W. M. Yen, S. Shionoya, H. Yamamoto, Phosphor Handbook, CRC press, Boca Raton, 2007.
19 T. Miyakawa and D. L. Dexter, *Phys. Rev. B*, 1970, **1**, 2961–2969.
20 D. L. Andrews and R. D. Jenkins, *J. Chem. Phys.*, 2001, **114**, 1089–1110.
21 T. Förster, *Ann. Phys.*, 1948, **2**, 55–75.
22 D. L. Dexter, *J. Chem. Phys.*, 1953, **21**, 836–850.
23 E. Fermi, Nuclear Physics. University of Chicago Press, Chicago, 1950.
24 P. A. M. Dirac, *Proc. Royal Soc. A*, 1927, **114**,243–265.
25 E. Nakazawa and S. Shionoya, *J. Chem. Phys.*, 1967, **47**, 3211–3219.
26 T. Kushida, *J. Phys. Soc. Japan*, 1983, **34**, 1313–1337.
27 M. Inokuti and F. Hirayama, *J. Chem. Phys.*, 1965, **43**, 1978–1989.
28 F. Varsanyi and G. H. Dieke, *Phys. Rev. Lett.*, 1961, **7**, 442–444.
29 S. C. Rand, L. S. Lee and A. L. Schawlow, *Opt. Commun.*, 1982, **42**, 179–184,
30 E. Dorman, *J. Chem. Phys.*,1966, **44**, 2910–2916.
31 D. L. Dexter, *Phys. Rev.*, 1957, **108**, 630–633.
32 D. L. Dexter, Phys. Rev., 1962, 126, 1962–1967.
33 A. L. Rogach, T. A. Klar, J. M. Lupton, A. Meijerink and J. Feldmann, *J. Mater. Chem. C*, 2009, **19**, 1208–1221.
34 G. Gómez-Santos and T. Stauber, *Phys. Rev. B*, 2011, **84**, 165438.
35 S. Jang, M. D. Newton and R. J. Silbey, *Phys. Rev. Lett.*, 2004, **92**, 218301/1–218301–4.
36 A. L. Rogach, *Nano Today*, 2011, **6**, 355–365.
37 P. L. Hernández–Martínez, A. O. Govorov and H. Volkan Demir, *J. Phys. Chem. C*, 2013, **117**, 10203−10212.
38 H. Lee, Y. C. Cheng and G. R. Fleming, *Science*, 2007, **316**, 1462–1465.
39 E. Collini and G. D. Scholes, *Science*, 2009, **323**, 369–373.
40 G. D. Scholes, *Annu. Rev. Phys. Chem.,* 2003, **54**, 57–87.
41 D. Beljonne, C. Curutchet, G. D. Scholes and R. J. Silbey, J. Phys. Chem. B, 2009, 113, 6583–6599.
42 H. DeVoe, *J. Chem. Phys.*, 1965, **43**, 3199-3208.
43 S. Valleau, S. K. Saikin, D. Ansari-Oghol-Beig, M. Rostami, H. Mossallaei, and A. Aspuru-Guzik, *ACS Nano*, 2014, **8**, 3884-3894.
44 J. S. Avery, *Proc. Phys. Soc.*, 1966, **88**, 1–8.
45 L. Gomberoff and E. A. Power, *Proc. Phys. Soc.*, 1966, **88**, 281–284.
46 D. L. Andrews, *J. Chem. Phys.*, 1989, **135**, 195–201.
47 G. J. Daniels, R. D. Jenkins, D. S. Bradshaw and D. L. Andrews, *J. Chem. Phys.*, 2003, **119**, 2264–2274.
48 D. L. Andrews and G. Juzeliūnas, *J. Chem. Phys.*, 1992, **96**, 6606–6612.
49 D. L. Andrews, *J. Phys. Chem. Lett.*, 2013, **4**, 3878–3884.
50 See, e.g., D. L. Andrew, Can. J. Chem., 2008, 86, 855-870.
51 J. R. Lakowicz, Principles of Fluorescence Spectroscopy, 3rd Ed., Springer 2006.
52 B. K. K. Fung and L. Stryer, *Biochemistry*, 1978, **17**, 5241–5248.
53 Yekta, J. Duhamel and M. A. Winnik, *Chem. Phys. Lett.*, 1995, **235**,119–125.
54 J. Rolinski and D. J. S. Birch, *J. Chem. Phys.*, 2000, **112**, 8923–8933.

55 T. Elsaesser, S. Mukamel, M.M. Murnane and N.F. Scherer, Ultrafast Phenomena XII, Springer, Berlin, 2000.
56 A. J. Nozik, *Ann. Rev. Phys. Chem.*, 2001, **52**, 193–231.
57 M. B. Smith and J. Michl, *Ann. Rev. Phys. Chem.*, 2013, **64**, 361 – 386.
58 G. S. Schlau–Cohen, A. Ishizaki and G. R. Fleming, *Chem. Phys.*, 2011, **386**, 1–22.
59 N. S. Ginsberg, Y. C. Cheng and G. R. Fleming, *Acc. Chem. Res.*, 2009, **42**, 1352–1363.
60 T. Brixner, J. Stenger, H. M. Vaswani, M. Cho, R. E. Blankenship and G. R. Fleming, *Nature*, 2005, **434**, 625–628.
61 G. Blasse and B. C. Grabmaier, Luminescent Materials, Springer–Verlag, Berlin 1994.
62 W. M. Yen, M. J. Weber, Inorganic phosphors: compositions, preparation, and optical properties, CRC Press, Boca Raton, Florida, 2000.
63 A. K. Levine and F. C. Palilla, *Appl. Phys. Lett.*, 1964, **5**, 118–120.
64 F. C. Palilla and A. K. Levine, *Appl. Opt.*, 1966, **5**, 1467–1468.
65 Y. G. Su, L. P. Li and G. S. Li, *Chem. Mater.*, 2008, **20**, 6060–6067.
66 A. K. Parchur, R. S. Ningthoujam, S. B. Rai, G. S. Okram, R. A. Singh, M. Tyagi, S. C. Gadkari, R. Tewari and R. K. Vatsa, *Dalton Trans*, 2011, **40**, 7595–7601.
67 R. J. Ginther, *J. Electrochem. Soc.*, 1954, **101**, 248–257.
68 J. S. Kim, P. E. Jeon, J. C. Choi, H. L. Park, S. I. Mho and G. C. Kim, *Appl. Phys. Lett.*, 2004, **84**, 2931–2933.
69 W. J. Yang, L. Y. Luo, T. M. Chen and N. S. Wang, *Chem. Mater.*, 2005, **17**, 3883–3888.
70 W. J. Yang and T. M. Chen, *Appl. Phys. Lett.*, 2006, **88**, 101903/1–3.
71 X. Orignac, D. Barbier, X. M. Du, R. M. Almeida, O. McCarthy and E. Yeatman, *Opt. Mater.*, 1999, **12**, 1–18.
72 S. Tanabe, T. Kouda and T. Hanada, *Opt. Mater.*, 1999, **12**, 35–40.
73 M. J. F. Digonnet, Rare–Earth–Doped Fiber Lasers and Amplifiers, Revised and Expanded, Marcel Dekker Inc., New York, 2001.
74 D. C. Yeh, R. R. Petrin, W. A. Sibley, V. Madigou, J. L. Adam and M. J. Suscavage, *Phys. Rev. B*, 1989, **39**, 80–90.
75 M. J. Weber, *Phys. Rev. B*, 1971, **4**, 3153–3159.
76 H. Y. Zhong, B. J. Chen, G. Z. Ren, L. H. Cheng, L. Yao and J. S. Sun, *J. Appl. Phys.*, 2009, **106**, 083114.
77 H. T. Guo, L. Liu, Y. Q. Wang, C. Q. Hou, W. N. Li, M. Lu, K. S. Zou and B. Peng, *Opt. Express*, 2009, **17**, 15350–15358.
78 J. C. Bourcet and F. K. Fong, *J. Chem. Phys.,* 1974, 60, 34–39.
79 J. X. Meng, J. Q. Li, Z. P. Shi, K. W. Cheah, *Appl. Phys. Lett.*, 2008, **93**, 221908/1–3.
80 J. J. Zhou, Y. Teng, X. F. Liu, S. Ye, Z. J. Ma and J. R. Qiu, *Phys. Chem. Chem. Phys.*, 2010, **12**, 13759–13762.
81 P. Chen, J. J. Zhou, Z. J. Fang, J. C. Wang, B. B. Xu, D. Z. Tan, S. N. Khisro and J. R. Qiu, *J. Noncryst. Solid*, 2014, **391**, 49–53.
82 J. X. Meng, K. W. Cheah, Z. P. Shi and J. Q. Li, *Appl. Phys. Lett.*, 2007, **91**, 151107/1–3.
83 B. T. Wu, J. Ruan, J. J. Ren, D. P. Chen, C. S. Zhu, S. F. Zhou and J. R. Qiu, *Appl. Phys. Lett.*, 2008, **92**, 041110/1–3.
84 B. T. Wu, S. F. Zhou, J. Ruan, Y. B. Qiao, D. P. Chen, C. S. Zhu and J. R. Qiu, *Opt. Express*, 2009, **16**, 1879–1984.
85 Y. X. Zhuang and S. Tanabe, *J. Appl. Phys.*, 2012, **112**, 093521/1–6.
86 J. Ruan, E. Wu, H. P. Zeng, S. F. Zhou, G. Lakshminarayana and J. R. Qiu, *Appl. Phys. Lett.*, 2008, **92**, 101121/1–3.
87 J. Ruan, Y. Z. Chi, X. F. Liu, G. P. Dong, G. Lin, D. P. Chen, E. Wu and J. R. Qiu, *J. Phys D–Appl. Phys.*, 2009, **42**, 155102/1–6.
88 F. Auzel, *Chem. Rev.*, 2004, **104**, 139–173.
89 F. Auzel, *Proc. IEEE.*, 1973, **61**, 758–787.
90 Q. Y. Zhang and X. Y. Huang, *Prog. Mater. Sci.*, 2010, **55**, 353–427.
91 E. Nakazawa and S. Shionoya, *Phys. Rev. Lett.*, 1970, **25**, 1710–1712.
92 F. W. Ostermay and L. G. Vanuiter, *Phys. Rev. B*, 1970, **1**, 4208–4212.
93 I. R. Martin, A. C. Yanes, J. Mendez–Ramos, M. E. Torres and V. D. Rodriguez, *J. Appl. Phys.*, 2001, **89**, 2520–2524.
94 M. A. Noginov, P. Venkateswarlu and M. Mahdi, *J. Opt. Soc. Am. A*, 1996, **13**, 735–741.
95 Y. Dwivedi and S. C. Zilio, *Opt. Express*, 2013, **21**, 4717–4727.
96 S. Heer, M. Wermuth, K. Krämer and H. U. Güdel, *Phys. Rev. B*, 2002, **65**, 125112/1–10.
97 C. Reinhard, R. Valiente, and H. U. Güdel, *J. Phys. Chem. B* 2002, **106**, 10051–10057.
98 S. García–Revilla, P. Gerner, O. S. Wenger, H. U. Güdel and R. Valiente, *Chem. Phys. Lett.*, 2005, **401**, 492–496.
99 P. Gerner, K. Krämer and H. U. Güdel, *J. Lumin.*, 2003, **102–103**, 112–118.
100 B. B. Xu, G. X. Bai, J. C. Wang, Q. B. Guo, D. Z. Tan, W. B. Chen, X. F. Liu, S. F. Zhou, J. H. Hao, J. R. Qiu, *Opt. Lett.*, 2014, **39**, 3022–3025.
101 S. Heer, K. Kompe, H. U. Güdel and M. Haase, *Adv. Mater.*, 2004, **16**, 2102–2105.
102 F. Wang and X. G. Liu, *Chem. Soc. Rev.*, 2009, **38**, 976–989.
103 M. Haase and H. Schäfer, *Angew. Chem. Int. Ed.*, 2011, **50**, 2–24.
104 G. Y. Chen, H. L. Qiu, P. N. Prasad, and X. Y. Chen, *Chem. Rev.*, 2014, **114**, 5161–5214.
105 X. F. Liu, G. P. Dong, Y. B. Qiao and J. R. Qiu, *Appl. Opt.*, 2008, **47**, 6416–6421.
106 D. Matsuura, *Appl. Phys. Lett.*, 2002, 81, 4526–4528.
107 F. Wang and X. G. Liu, *J. Am. Chem. Soc.*, 2008, **130**, 5642–5643.
108 W. Q. Zou, C. Visser, J.A. Maduro, M. S. Pshenichnikov and J. C. Hummelen, *Nat. Photonics*, 2012, **6**, 560–564.
109 R. T. Wegh, H. Donker, K. D. Oskam, and A. Meijerink, *Science*, 1999, **283**, 663–666.
110 R. T. Wegh, E.V.D. van Loef, A. Meijerink, *J. Lumin.*, 2000, **90**, 111–122.
111 Z. G. Nie, J. H. Zhang, X. Zhang, X. G. Ren, X. J. Wang and G. B. Zhang, *Opt. Lett.*, 2007, **32**, 991–993.
112 A. M. Srivastava and W. W. Beers, *J. Lumin.*, 1997, **71**, 285–290.
113 Y. Chen, C. Shi, W. Yan, Z. Qi and Y. Fu, *Appl. Phys. Lett.*, 2006, **88**, 061906/1–3.
114 B. M. van der Ende, L. Aarts and A. Meijerink, *Phys. Chem. Chem. Phys.*, 2009, **11**, 11081–11095.
115 J. M. Meijer, L. Aarts, B. M. van der Ende, T. J. H. Vlugt and A. Meijerink, Phys. Rev. B, 2010, **81**, 035107/1–9.
116 X. J. Zhou, Y. J. Wang, X. Q. Zhao, L. Li, Z. Q. Wang and Q. X. Li, *J. Am. Ceram. Soc.,* 2014, **97**, 179–184.
117 B. Fan, C. Chlique, O. Merdrignac–Conanec, X. H. Zhang and X. P. Fan, *J. Phys. Chem. C*, 2012, **116**, 11652−11657.
118 J. F. Wu, Thulium Doped Microsphere Laser and Fiber Laser, PhD Thesis, The University of Arizona, Tucson, 2005.
119 D. F. de Sousa, R. Lebullenger, A. C. Hernandes and L. A. O. Nunes, *Phys. Rev. B*, 2002, **65**, 094204/1–6.
120 J. F. Wu, S. B. Jiang, T. Q. Qiu, M. Morrell, A. Schulzgen and N. Peyghambarian, *SPIE*, 2005, **5723**, 152–161.
121 P. Vergeer, T. J. H. Vlugt, M. H. F. Kox, M. I. den Hertog, J. P. J. M. van der Eerden and A. Meijerink, *Phys. Rev. B*, 2005, **71**, 014119/1–6.
122 Q. Y. Zhang, G. F. Yang and Z. H. Jiang, *Appl. Phys. Lett.*, 2007, **91**, 051903/1–3.
123 X. F. Liu, Y. B. Qiao, G. P. Dong, S. Ye, B. Zhu, G. Lakshminarayana, D. P. Chen and J. R. Qiu, *Opt. Lett.*, 2008, **33**, 2858–2860.
124 B. M. van der Ende, L. Aarts and A. Meijerink, *Adv. Mater.*, 2009, **21**, 3073–3077.

125 X. F. Liu, S. Ye, Y. B. Qiao, G. P. Dong, B. Zhu, D. P. Chen, G. Lakshminarayana and J. Qiu, *Appl. Phys. B*, 2009, **96**, 51–55.
126 S. Ye, B. Zhu, J. X. Chen, J. Luo and J. R. Qiu, *Appl. Phys. Lett.*, 2008, **92**, 141112/1–3.
127 Q. Luo, X. S. Qiao, X. P. Fan, H. Y. Fu, J. L. Huang, Y. J. Zhang, B. Fan and X. H. Zhang, *J. Am. Ceram. Soc.*, 2012, **95**, 1042–1047.
128 J. Ueda and S. Tanabe, *J. Appl. Phys.*, 2009, **106**, 043101/1–5.
129 D. C. Yu, F. T. Rabouw, W. Q. Boon, T. Kieboom, S. Ye, Q. Y. Zhang, and A. Meijerink, *Phys. Rev. B*, 2014, **90**, 165126/1 – 7.
130 X. F. Liu, Y. Teng, Y. X. Zhuang, J. H. Xie, Y. B. Qiao, G. P. Dong, D. P. Chen and J. R. Qiu, *Opt. Lett.*, 2009, **34**, 3565–3567.
131 P. Dorenbos, J. Phys. Cond. Matt., 2003, 15, 8417–8434.
132 G. Y. Chen, C. H. Yang and P. N. Prasad, *Acc. Chem. Res.*, 2013, **46**, 1474–1486.
133 S. L. Gai, C. X. Li, P. P. Yang and J. Lin, *Chem. Rev.*, 2014, **114**, 2343−2389.
134 L. D. Sun, Y. F. Wang, and C. H. Yan, *Acc. Chem. Res.*, 2014, **47**, 1001–1009.
135 G. Y. Chen, H. Ågren, T. Y. Ohulchanskyy and P. N. Prasad, *Chem. Soc. Rev.*, 2015, **44**, 1680–1713.
136 J. R. DiMaio, C. Sabatier, B. Kokuoz and J. Ballato, *Proc. Natl. Acad. Sci. USA.*, 2008, **105**, 1809–1813.
137 J. R. DiMaio, B. Kokuoz, T. L. James and J. Ballato, *Adv. Mater.*, 2007, **19**, 3266–3270.
138 F. Wang, R. R. Deng, J. Wang, Q. X. Wang, Y. Han, H. M. Zhu, X. Y. Chen and X. G. Liu, *Nat. Mater.*, 2011, **10**, 968–973.
139 R. R. Deng, F. Qin, R. F. Chen, W. Huang, M. H. Hong and X. G. Liu, *Nat. Nanotechnol.*, 2015, **10**, 237–242.
140 D. J. Norris, A. L. Alfros and S. C. Erwin, *Science*, 2008, **319**, 1776–1780.
141 J. D. Bryan and D. R. Gamelin, *Prog. Inorg. Chem.*, 2005, **54**, 47–126.
142 R. N. Bhargava, D. Gallagher, X. Hong and A. Nurmikko, *Phys. Rev. Lett.*, 1994, **72**, 416–419.
143 Y. L. Soo, Z. H. Ming, S. W. Huang, and Y. H. Kao, R. N. Bhargava and D. Gallagher, *Phys. Rev. B*, 1994, **50**, 7602–7607.
144 B. B. Srivastava, S. Jana and N. Pradhan, *J. Am. Chem. Soc.*, 2011, **133**, 1107–1115.
145 A. A. Khosravi, M. Kundu, L. Jatwa, S. K. Deshpande, U. A. Bhagwat, M. Sastry and S. K. Kulkarni, *Appl. Phys. Lett.*, 1995, **67**, 2702–2704.
146 A. A. Bol, J. Ferwerda, J. A. Bergwerff and A. Meijerink, *J. Lumin.*, 2002, **99**, 325–334.
147 R. G. Xie and X. G. Peng, *J. Am. Chem. Soc.*, 2009, **131**, 10645–10651.
148 A. J. Steckl, J. C. Heikenfeld, D. S. Lee, M. J. Garter, C. C. Baker, Y. Q. Wang and R. Jones, *IEEE J. Sel. Top. Quant.*, 2002, **8**, 749–766.
149 J. C. Heikenfeld, M. Garter, D. S. Lee, R. Birkhahn and A. J. Steckl, *Electron Lett.*, 1989, **25**, 718–719.
150 J. Heikenfeld, M. Garter, D. S. Lee, R. Birkhahn and A. J. Steckl, *Appl. Phys. Lett.*, 1999, **75**, 1189–1191.
151 R. Birkhahn, M. Garter and A. J. Steckl, *Appl. Phys. Lett.*, 1999, **74**, 2161 – 2163.
152 D. A. Chengelis, A. M. Yingling, P. D. Badger, C. M. Shade and S. Petoud, *J. Am. Chem. Soc.*, 2005, **127**, 16752−16753.
153 O. E. Raola and G. F. Strouse, *Nano Lett.*, 2002, **2**, 1443−1447.
154 R. Martín–Rodríguez, R. Geitenbeek and A. Meijerink, *J. Am. Chem. Soc.*, 2013, **135**, 13668−13671.
155 Y. M. Zhao, F. T. Rabouw, T. van Puffelen, C. A. van Walree, D. R. Gamelin, C. D. Donega and A. Meijerink, *J. Am. Chem. Soc.*, 2014, **136**, 16533–16543.
156 M. Fujii, M. Yoshida, Y. Kanzawa, S. Hayashi and K. Yamamoto, *Appl. Phys. Lett.*, 1997, **71**, 1198–1200.
157 D. Timmerman, I. Izeddin, P. Stallinga, I. N. Yassievich And T. Gregorkiewicz, *Nat. Photonics*, 2008, **2**, 105–109.
158 N. N. Ha, S. Cueff, K. Dohnalová, M. T. Trinh, C. Labbé, R. Rizk, I. N. Yassievich, and T. Gregorkiewicz, *Phys. Rev. B*, 2011, **84**, 241308/1–5.
159 I. Izeddin, M. A. J. Klik, N. Q. Vinh, M. S. Bresler and T. Gregorkiewicz, *Phys. Rev. Lett.*, 2007, **99**, 077401/1–4.
160 I. Izeddin, D. Timmerman, T. Gregorkiewicz, A. S. Moskalenko, A. A. Prokofiev, I. N. Yassievich and M. Fujii, *Phys. Rev. B*, 2008, **18**, 035327/1–14.
161 S. Saeed, E.M.L.D. de Jong, K. Dohnalova and T. Gregorkiewicz, *Nat. Commun.*, 2014, **5**, 4665/1–5.
162 S. Y. Seo, M. J. Kim and J. H. Shin, *Appl. Phys. Lett.*, 2003, **83**, 2778–2780.
163 R. D. Schaller and V. I. Klimov, *Phys. Rev. Lett.*, 2004, **92**, 186601/1–4.
164 M. C. Beard, K. P. Knutsen, P. R. Yu, J. M. Luther, Q. Song, W. K. Metzger, R. J. Ellingson and A. J. Nozik, *Nano Lett.*, 2007, **7**, 2506–2512.
165 V. I. Klimov, *Ann. Rev. Phys. Chem.*, 2007, **58**, 635–673.
166 R. J. Ellingson, Ma. C. Beard, J. C. Johnson, P. R. Yu, O. I. Mićić, A. J. Nozik, A. Shabaev and A. L. Efros, *Nano Lett.*, 2005, **5**, 865–871.
167 J. E. Murphy, M. C. Beard, A. G. Norman, S. P. Ahrenkiel, J. C. Johnson, Pin. R. Yu, O. I. Mićić, R. J. Ellingson and A. J. Nozik, *J. Am. Chem. Soc.*, 2006, **128**, 3241–3247.
168 L. A. Padilha, J. T. Stewart, R. L. Sandberg, W. K. Bae, W. K. Koh, J. M. Pietryga and V. I. Klimov, *Acc. Chem. Res.*, 2013, **46**, 1261–1269.
169 A. J. Nozik, M. C. Beard, J. M. Luther, M. Law, R. J. Ellingson and J. C. Johnson, *Chem. Rev.*, 2010, **110**, 6873–6890.
170 D. Timmerman, J. Valenta, K. Dohnalová, W. D. A. M. de Boer and T. Gregorkiewicz, *Nat. Nanotechnol.*, 2011, **6**, 710–714.
171 W. D. A. M. de Boer, D. Timmerman, K. Dohnalova, I. N. Yassievich, H. Zhang, W. J. Buma and T. Gregorkiewicz, *Nat. Nanotechnol.*, 2010, **5**, 878–884.
172 M. Govoni, I. Marri and S. Ossicini, *Nat. Photonics*, 2012, 6, 672–679.
173 I. Marri, M. Govoni and S. Ossicini, *J. Am. Chem. Soc.*, 2014, 136, 13257−13266.
174 M. B. Smith and J. Michl, Chem. Rev., 2010, 110, 6891–6936.
175 A. Köhler, H. Bässler, *Mat. Sci. Eng. R*, 2009, 66, 71–109.
176 T. Zeng, N. Ananth and R. Hoffmann, *J. Am. Chem. Soc.*, 2014, 136, 12638−12647.
177 E. C. Greyson, B. R. Stepp, X. D. Chen, A. F. Schwerin, I. Paci, M. B. Smith, A. Akdag, J. C. Johnson, A. J. Nozik, J. Michl and M. A. Ratner, *J. Phys. Chem. B*, 2010, 114, 14223–14232.
178 J. C. Johnson, A, J. Nozik and J. Michl, *Acc. Chem. Res.*, 2013, 46, 1290–1299.
179 V. Agranovich, Y. Gartstein and M. Litinskaya, *Chem. Rev.*, 2011, **111**, 5179–5214.
180 J. Lee, P. Jadhav, P. D. Reusswig, S. R. Yost, N. J. Thompson, D. N. Congreve, E. Hontz, T. Van Voorhis and M. A. Baldo, *Acc. Chem. Res.*, 2013, **46**, 1300–1311.
181 M. Tabachnyk, B. Ehrler, S. Gélinas, M. L. Böhm, B. J.Walker, K. P. Musselman, N. C. Greenham, R. H. Friend and A. Rao, *Nat. Mater.*, 2014, **13**, 1033–1038.
182 N. J. Thompson, M. W. B. Wilson, D. N. Congreve, P. R. Brown, J. M. Scherer, T. S. Bischof, M. F. Wu, N. Geva, M. Welborn, T. V. Voorhis, V. Bulovic, M. G. Bawendi and M. A. Baldo, *Nat. Mater.*, 2014, **13**, 1039–1043.
183 Q. H. Wang, K. Kalantar-Zadeh, A. Kis, J. N. Coleman and M. S. Strano, *Nat. Nanotechnol.*, 2012, **7**, 699–712.
184 P. Miró, M. Audiffred and T. Heine, *Chem. Soc. Rev.*, 2014, **43**, 6537–6554.
185 A. K. Geim and K. S. Novoselov, *Nat. Mater.*, 2007, **6**, 183–191.
186 R. R. Nair, P. Blake, A. N. Grigorenko, K. S. Novoselov, T. J. Booth, T. Stauber, N. M. R. Peres and A. K. Geim, *Science*, 2008, **320**, 1308.

187 R. S. Swathi and K. L. Sebastian, *J. Chem. Phys.*, 2008, **129**, 054703/1–9.
188 R. S. Swathi and K. L. Sebastian, *J. Chem. Phys.*, 2009, **130**, 086101/1–3.
189 R. S. Swathi and K. L. Sebastian, *J. Chem. Sci*., 2012, **124**, 233–240.
190 R. S. Swathi and K. L. Sebastian, *J. Chem. Sci*., 2009, **121**, 777–787.
191 L. Gaudreau, K. J. Tielrooij, G. E. D. K. Prawiroatmodjo, J. Osmond, F. J. G. de Abajo and F. H. L. Koppens, *Nano Lett.*, 2013, **13**, 2030−2035.
192 Z. Y. Chen, S. Berciaud, C. Nuckolls, T. F. Heinz and L. E. Brus, *ACS Nano*, 2010, **4**, 2964–2968.
193 F. Federspiel, G. Froehlicher, M. Nasilowski, S. Pedetti, A. Mahmood, B. Doudin, S. Park, J.–O Lee, D. Halley, B. Dubertret, P. Gilliot and S. Berciaud *Nano Lett.*, 2015, **15**, 1252−1258.
194 T. N. Lin, L. T. Huang, G. W. Shu, C. T. Yuan, J. L. Shen, C. A. J. Lin, W. H. Chang, C. H. Chiu, D. W. Lin, C. C. Lin and H. C. Kuo, *Opt. Lett.*, 2013, **38**, 12897–2899.
195 Y. J. Yu, K. S. Kim, J. Nam, S. R. Kwon, H. Byun, K. Lee, J. H. Ryou, R. D. Dupuis, J. Kim, G. Ahn, S. Ryu, M. Y. Ryu and J. S. Kim, *Nano Lett.*, 2015, **15**, 896–902.
196 J. Y. Lee, W. Bao, L. Ju, P. J. Schuck, F. Wang, and A. Weber–Bargioni, *Nano Lett.*, 2014, **14**, 7115−7119.
197 K. F. Mak, C. Lee, J. Hone, J. Shan, and T. F. Heinz, *Phys. Rev. Lett.*, 2010, **105**, 136805/1–4.
198 L. J. Zhang and A. Zunger, *Nano Lett.*, 2015, **15**, 949−957.
199 G. Eda, H. Yamaguchi, D. Voiry, T. Fujita, M. W. Chen and M. Chhowalla, *Nano Lett.*, 2011, 1, 5111–5116.
200 F. Prins, A. J. Goodman and W. A. Tisdale, *Nano Lett.*, 2014, **14**, 6087−6091.
201 J. M. Gordon and Y. N. Gartstein, *J. Phys.: Condens. Matter*, 2013, **25**, 425302/1–10.
202 D. Prasai, A.R. Klots, AKM Newaz, J. S. Niezgoda, N. J. Orfield, C. A. Escobar, A. Wynn, A.Efimov, G. K. Jennings, S. J. Rosenthal and K. I. Bolotin, *Nano Lett.*, 2015, DOI: 10.1021/acs.nanolett.5b00514.
203 L. T. Kunneman, M. D. Tessier, H. Heuclin, B. Dubertret, Y. V. Aulin, F. C. Grozema, J. M. Schins and L.D. A. Siebbeles, *J. Phys. Chem. Lett.*, 2013, **4**, 3574−3578.
204 B. Guzelturk, M. Olutas, S. Delikanli Y. Kelestemur, O. Erdema and H. Volkan Demir, *Nanoscale*, 2015, **7**, 2545–2551.
205 C. E. Rowland, I. Fedin, H. Zhang, S. K. Gray, A. O. Govorov, D.V. Talapin and R. D. Schaller, *Nat. Mater.*, 2015, **14**, 484 – 489.
206 I. Moreels, *Nat. Mater.*, 2015, 14, 464–465.
207 M. C. Heffern, L. M. Matosziuk and T. J. Meade, *Chem. Rev.*, **114**, 4496−4539.
208 A. D'Aléo, F. Pointillart, L. Ouahabb, C. Andraudc and O. Maury, Cood. *Chem. Rev.*, 2012, **256**, 1604–1620.
209 S. Faulkner, L. S. Natrajan, W. S. Perry and D. Sykes, *Dalton Trans.*, 2009, **20**, 3890–3899.
210 J. Lehr, P. D. Beer, S. Faulkner and J. J. Davis, *Chem. Commun.*, 2014, **50**, 5678–5687.
211 M. D. Ward, Coord. *Chem. Rev.,* 2007, **251**, 1663–1677.
212 A. Foucault–Colleta, K. A. Gogick, K. A. White, S. Villette, A. Pallier, G. Collet, C. Kieda, T. Li, S. J. Geib, N. L. Rosi and S. Petoud, *Proc. Natl. Acad. Sci. U. S. A.*, 2013, **110**, 17199–17204.
213 M. Anni, L. Manna, R. Cingolani, D. Valerini, A. Creti and M. Lomascolo, *Appl. Phys. Lett.*, 2004, **85**, 4169–4171.
214 P. O. Anikeeva, C. F. Madigan, S. A. Coe–Sullivan, J. S. Steckel, M. G. Bawendi, and V. Bulovic, *Chem. Phys. Lett.*, 2006, **424**, 120–125.
215 S. Blumstengel, S. Sadofev, C. Xu, J. Puls and F. Henneberger, *Phys. Rev. Lett.*, 2006, **97**, 237401/1–4.
216 P. Mulvaney, *Langmuir*, 1996, **12**, 788–800.
217 E. Fort and S. Grésillon, *J. Phys. D: Appl. Phys.*, 2008, **41** 013001/1–31.
218 T. Ming, H. J. Chen, R. B. Jiang, Q. Li and J. F. Wang, *J. Phys. Chem. Lett.*, 2012, **3**, 191−202.
219 H. F. Yuan, S. Khatua, P. Zijlstra, M. Yorulmaz and M. Orrit, *Angew. Chem. Int. Ed.*, 2012, **51**, 1217–1221.
220 O. Debieu, D. Breard, A. Podhorodecki, G. Zatryb, J. Misiewicz, C. Labbe, J. Cardin and F. Gourbilleau, *J. Appl. Phys.*, 2010, **108**, 113114/1–6.
221 K. Watanabe, H. Tamaoka, M. Fujii, K. Moriwaki and S. Hayashi, *Physica E*, 2002, **13**, 1038–1042
222 T. Hayakawa, S. T. Selvan and M. Nogami, *Appl. Phys. Lett.*, 1999, **74**, 1513–1515.
223 Y. Teng, K. Ueno, X. Shi, D. Aoyo, J. R. Qiu and H. Misawa, *Ann. Phys.*, 2012, **524**, 733–740.
224 R. B. Jiang, B. X. Li, C. H. Fang and J. F. Wang, *Adv. Mater.*, 2014, **26**, 5274–5309.
225 M. M. Shang, C. X. Li and J. Lin, *Chem. Soc. Rev.*, 2014, **43**, 1372–1386.
226 C. H. Huang, W. R. Liu and T. M. Chen, *J. Phys. Chem. C*, 2014, **118**, 11026−11034.
227 Z. L. Wang, H. B. Liang, M. L. Gong and Q. Su, *Electrochem. Solid State Lett.*, 2005, **8**, H33–H35.
228 H. K. Yang, H. M. Noh and J. H. Jeong, *Solid State Sci.*, 2014, **27**, 43–46.
229 S. Unithrattil, K. H. Lee, W. J. Chung and W. Bin Im, *J. Lumin.*, 2014, **152**, 176–181.
230 A. Shalav, B.S. Richards and M. A. Green, *Solar Energy Mat. Solar Cell*, 2007, **91**, 829–842.
231 T. Trupke, A. Shalav, B.S. Richards, P. Würfel and M.A. Green, *Solar Energy Mat. Solar Cell*, 2006, 90, 3327–3338.
232 T. Trupke, M. A. Green and P. Würfel, *J. Appl. Phys.*, 2002, **92**, 4117–4123.
233 J. de Wild, A. Meijerink, J. K. Rath, W. G. J. H. M. van Sark and R. E. I. Schropp, *Energy Environ. Sci.*, 2011, **4**, 4835–4848.
234 B. S. Richards, *Solar Energy Mat. Solar Cell*, 2006, **90**, 1189–1207.
235 X. Huang, S. Han, W. Huang and X. Liu, *Chem. Soc. Rev.*, 2013, **42**, 173–201.
236 A. Shalav, B. S. Richards, and T. Trupke, K. W. Krämer and H. U. Güdel, *Appl. Phys. Lett.*, 2005, **86**, 013505/1–3.
237 J. de Wild, A. Meijerink, J. K. Rath, W. G. J. H. M. van Sark and R. E. I. Schropp, *Solar Energy Mat. Solar Cell*, 2010, **94**, 1919–1922.
238 Y. Chen, W. He, Y. Jiao, H. Wang, X. Hao, J. Lu and S. E. Yang, *J. Lumin.*, 2012, **132,** 2247–2250.
239 A. Boccolini, R. Faoro, E. Favilla, S. Veronesi and M. Tonelli, *J. Appl. Phys.*, 2013, **114**, 064904/1–7.
240 X. Wu, G. Q. Lu and L. Wang, *Adv. Energy Mater.*, 2013, **3**, 704–707.
241 C. Yuan, G. Chen, P. N. Prasad, T. Y. Ohulchanskyy, Z. Ning, H. Tian, L. Sun and H. Ågren, *J. Mater. Chem.*, 2012, **22**, 16709–16713.
242 P. Ramasamy and J. Kim, *Chem. Comm.*, 2014, **50**, 879–881.
243 W. Guo, K. Zheng, W. Xie, L. Sun, L. Shen, C. Liu, Y. He and Z. Zhang, *Solar Energy Mat. Solar Cell*, 2014, **124**, 126–132.
244 M. Kong, W. Hu, F. Cheng, Z. Huang, J. Zhang, Z. Han, N. Shi, Q. Fan, S. Chen and W. Huang, *J. Mater. Chem. C*, 2013, **1**, 5872–5878.
245 W. Qin, D. Zhang, D. Zhao, L. Wang and K. Zheng, *Chem. Commun.,* 2010, **46**, 2304–2306.
246 Y. Tang, W. Di, X. Zhai, R. Yang, and W. Qin, *ACS Catal.*, 2013, **3**, 405−412.
247 X. Guo, W. Song, C. Chen, W. Di and W. Qin, *Phys. Chem. Chem. Phys.*, 2013, **15**, 14681–14688.
248 X. Guo, W. Di, C. Chen, C. Liu, X. Wang and W. Qin, *Dalton Trans.*, 2014, **43**, 1048–1054.
249 Y. Zhang and Z. Hong, *Nanoscale*, 2013, **5**, 8930–8933.

250 F. Gonell, M. Haro, R. S. Sánchez, P. Negro, I. Mora–Seró, J. Bisquert, B. Julián–López and S. Gimenez, *J. Phys. Chem. C*, 2014, **118**, 11279−11284.
251 C. K. Chen, H. M. Chen, C. J. Chen and R. S. Liu, *Chem. Commun.*, 2013, **49**, 7917–7919.
252 Z. X. Li, F. B. Shi, T. Zhang, H. S. Wu, L. D. Sun and C. H. Yan, *Chem. Commun.*, 2011, **47**, 8109–8111.
253 S. Obregón and G. Colón, *Appl. Catal. B–Environ.*, 2014, **152–153**, 328–334.
254 S. Chen, B. Peng, F. Lu, Y. Mei, F. Cheng, L. Deng, Q. Xiong, L. Wang, X. Sun and W. Huang, *Adv. Optical Mater.*, 2014, **2**, 442–449.
255 M. C. Beard, J. C. Johnson, J. M. Luther and A. J. Nozik, *Phil. Trans. R. Soc. A*, 2014, **373**, 20140412/1–11.
256 M. C. Hanna and A. J. Nozik, *J. Appl. Phys.*, 2006, **100**, 074510/1–8.
257 S. Ten Cate, C. S. S. Sandeep, Y. Liu, M. Law, S. Kinge, A. J. Houtepen, J. M. Schins, L. D. A. Siebbeles, *Acc. Chem Res.*, 2015, **48**, 174–181.
258 J. B. Sambur, T. Novet, B. A. Parkinson, *Science*, 2010, **330**, 63–66.
259 O. E. Semonin, J. M. Luther, S. Choi, H.–Y. Chen, J. B. Gao, A.J. Nozik and M. C. Beard, *Science*, 2011, **334**, 1530–1533.
260 D. N. Congreve, J. Lee, N. J. Thompson, E. Hontz, S. R. Yost, P. D. Reusswig, M. E. Bahlke, S. Reineke, T. Van Voorhis, M. A. Baldo, *Science*, 2013, **340**, 334–337.
261 M. W. B. Wilson, A. Rao, B. Ehrler and R. H. Friend, *Acc. Chem. Res.*, 2013, **46**, 1330–1338.
262 L. Yang, M. Tabachnyk, S. L. Bayliss, M. L. Böhm, K. Broch, N. C. Greenham, R. H. Friend and B. Ehrler, *Nano Lett.*, 2015, **15**, 354–358.
263 D. K. Chatteriee, A. J. Rufalhah, Y. Zhang, *Biomaterials*, 2008, **29**, 937–943.
264 Y. I. Park, K. T. Lee, Y. D. Suh and T. Hyeon, *Chem. Soc. Rev.*, 2015, **44**, 1302–1317.
265 A. Sedlmeier and H. H. Gorris, *Chem. Soc. Rev.*, 2015, **44**, 1526–1560.
266 M. K. G. Jayakumar, *Proc. Natl. Acad. Sci. U.S.A.*, 2012, **109**, 8483–8488.
267 Y. F. Wang, G. Y. Liu, L. D. Sun, J. W. Xiao, J. C. Zhou and C. H. Yan, *ACS Nano*, 2013, **7**, 7200–7206.
268 J. J. Zhou, N. Shirahata, H. T. Sun, B. Ghosh, M. Ogawara, Y. Teng, S. F. Zhou, R. G. Chu, M. Fujii and J. R. Qiu, *J. Phys. Chem. Lett.*, 2013, **4**, 402−408.
269 E. G. Yukihara and W. S. McKeever, Optically Stimulated Luminescence: Fundamental and Applications (John Wiley & Sons Ltd., 2011).
270 S. Schweizer, *Phys. Stat. Sol. A*, 2001, **187**, 335–393.
271 Y. Li, S.F. Zhou, G. P. Dong, M. Y. Peng, L. Wondraczek and J. R. Qiu, *Sci. Report*, 2014, **4**, 4059/1–6.
272 A. Periasamy, *J. Biomed. Opt.*, 2001, **6**, 287–291.
273 A. P. Demchenko, Introduction to Fluorescence Sensing, Springer, 2009.
274 E. A Jares–Erijman and T. M. Jovin, *Nat. Biotechnolog*y, 2003, **21**, 1387–1385.
275 R. M. Clegg, R.M. Fluorescence resonance energy transfer (FRET) in Fluorescence Imaging Spectroscopy and Microscopy, (eds. Wang, X.F. and Herman, B.) 179–252, John Wiley & Sons, New York, 1996.
276 R. B. Sekar and A. Periasamy, *J. Cell Biol.*, 2003, **160**, 629–633.
277 R. Y. Tsien and A. Miyawaki, *Science*, 1998, **280**, 1954–1955.
278 see, e.g., M. A. D. Pozo, , W.B. Kiosses, N.B. Alderson, N. Meller, K.M. Hahn and M.A. Schwartz. *Nat. Cell Biol.*, 2002, **4**, 232–239.
279 M. Elangovan, H. Wallrabe, Y. Chen, R.N. Day, M. Barroso and A. Periasamy, *Methods*, 2003, **29**, 58–73.
280 M. Elangovan, R.N. Day and A. Periasamy, *J. Microsc.*, 2002, **205**, 3–14.
281 P. I. H. Bastiaens and A. Squire, *Trend Cell Biology*, 1999, **9**, 48 – 52.
282 W. Zheng, S. Zhou, Z. Chen, P. Hu, Y. Liu, D. Tu, H. Zhu, R. Li, M. Huang and X. Y. Chen, *Angew. Chem. Int. Ed.*, 2013, **52**, 6671 –6676.
283 Y. S. Liu, D. T. Tu, H. M. Zhu and X. Y. Chen, *Chem. Soc. Rev.*, 2013, **42**, 6924–6958.
284 M. Wang, W. Hou, C. C. Mi, W. X. Wang, Z. R. Xu, H. H. Teng, C. B. Mao and S. K. Xu, *Anal. Chem.*, 2009, **81**, 8783–8789.
285 X L. Y. Wang, R. X. Yan, Z. Y. Hao, L. Wang, J. H. Zeng, H. Bao, X. Wang, Q. Peng and Y. D. Li, *Angew. Chem., Int. Ed.*, 2005, **44**, 6054–6057.
286 D. Tu, L. Liu, Q. Ju, Y. Liu, H. Zhu, R. Li and X. Y. Chen, *Angew. Chem. Int. Ed.,* 2011, **50**, 6306 –6310.
287 Y. Lu, J. Zhao, R. Zhang, Y. Liu, D. Liu, E. M. Goldys, X. Yang, P. Xi, A. Sunna, J. Lu, Y. Shi, R. C. Leif, Y. Huo, J. Shen, J. A. Piper, J. P. Robinson and D. Jin, *Nat. Photonics*, 2014, **8**, 32–36.
288 X. D. Wang, O. S. Wolfbeis and R. J. Meier, *Chem. Soc. Rev.*, 2013, **42**, 7834.
289 G. Kucsko, P. C. Maurer, N. Y. Yao, M. Kubo, H. J. Noh, P. K. Lo, H. Park and M. D. Lukin, *Nature*, 3013, **500**, 54–58.
290 D. Jaque, B. del Rosal, E. M. Rodríguez, L. Martínez Maestro, P. Haro-González and J. G. Solé, *Nanomedicine*, 2014, **9**, 1047–1062.
291 D. Ross, Mi. Gaitan and L. E. Locascio, *Anal. Chem.,* 2001, **73**, 4117–4123.
292 J. Feng, K. J. Tian, D.H. Hu, S. Q. Wang, S. Y. Li, Y. Zeng, Y. Li and G. Q. Yang, *Angew. Chem. Int. Ed.*, 2011, **50**, 8072–8076.
293 See, for example, J. F. Lou, T. A. Hatton and P. E. Laibinis, *Anal. Chem.*, 1997, **69**, 1262–1264.
294 X S. F. León–Luis, U. R. Rodríguez–Mendoza, I. R. Martín, E. Lalla and V. Lavín, *Sensor Actuat. B: Chem.*, 2013, **176**, 1167–1175.
295 S. A. Wade, S. F. Collins and G. W. Baxter, *J. Appl. Phys.*, 2003, **94**, 4743–4756.
296 E. J. McLaurin, V. A. Vlaskin and D. R. Gamelin, *J. Am. Chem. Soc.*, 2011, **133**, 14978–14980.
297 X. Rao, T. Song, J. Gao, Y. Cui, Y. Yang, C. Wu, B. Chen and G. Qian, *J. Am. Chem. Soc.*, 2013, **135**, 15559−15564.
298 Y. Cui, H. Xu, Y. Yue, Z. Guo, J. Yu, Z. Chen, J. Gao, Y. Yang, G. Qian and B. Chen, *J. Am. Chem. Soc.*, 2012, **134**, 3979−3982.
299 S. H. Zheng, W. B. Chen, D. Z. Tan, J. J. Zhou, Q. B. Guo, W. Jiang, C. Xu, X. F. Liu and J. R. Qiu, *Nanoscale*, 2014, **6**, 5675–5679.
300 H. S. Mader and O. S. Wolfbeis, *Anal. Chem.*, 2010, **82**, 5002–5004.
301 R. J. Meier, J. M. B. Simburger, T. Soukka and M. Schaferling, *Anal. Chem.*, 2014, **84**, 5535–5540.
302 D. E. Achatz, R. J. Meier, L. H. Fischer and O. S. Wolfbeis, *Angew. Chem. Int. Ed.*, 2011, **50**, 260 –263.
303 Q. Liu, J. J. Peng, L. N. Sun and F. Y. Li, *ACS Nano*, 2011, **5**, 8040–8048.
304 J. Zhang, B. Li, L. M. Zhang and L. G. Zhang, *Chemphyschem*, 2013, **14**, 2897–2901.
305 R. A. Forman, S. Block, J. D. Barnett and G. J. Piermari, *Science*, 1972, **176**, 284–285.
306 J. C. Zhang, C. N. Xu, S. Kamimura, Y. Terasawa, H. Yamada and X. Wang, *Opt. Expres*s, 2013, **21**, 12976–12986
307 S. N. Raja, A. C. K. Olson, K. Thorkelsson, A. J. Luong, L. Hsueh, G. Chang, B. Gludovatz, L. Lin, T. Xu, R. O. Ritchie and A. P. Alivisatos, *Nano Lett.*, 2013, **13**, 3915−3922.
308 R. Kolesov, K. Xia, R. Reuter, R. Stöhr, A. Zappe, J. Meijer, P. R. Hemmer and J. Wrachtrup, *Nat. Commun.*, 2012, **3**, 1029/1–7.
309 T. Utikal, E. Eichhammer, L. Petersen, A. Renn, S. Götzinger and V. Sandoghdar, *Nat. Commun.*, 2014, **5**, 3627/1–8.